

INVESTIGATION OF CONJUGATED POLYELECTROLYTES AND THEIR PROTEIN
SENSING BY FLUORESCENCE CORRELATION SPECTROSCOPY

By

DANLU WU

A DISSERTATION PRESENTED TO THE GRADUATE SCHOOL
OF THE UNIVERSITY OF FLORIDA IN PARTIAL FULFILLMENT
OF THE REQUIREMENTS FOR THE DEGREE OF
DOCTOR OF PHILOSOPHY

UNIVERSITY OF FLORIDA

2012

© 2012 Danlu Wu

To my parents

ACKNOWLEDGMENTS

I would avail myself of this opportunity to express my heartfelt thanks to those people who have ever helped, supported and accompanied with me during my journey toward this important milestone in my life. First of all, I would like to express the sincere appreciation to my advisor, Dr. Kirk Schanze, for his expert, valuable guidance and encouragement. His knowledgeability and enthusiasm to science stimulate my creativity and independence, making me enjoy wandering in the science wonderland.

I also would like to take this opportunity to record my sincere thanks to all the former and current members of the Schanze group. When I first started experiments, Dr. Eunkyung Ji and Dr. Katsu Ogawa kindly taught me how to use instruments and how to design an analytical experiment. Dr. Chen Liao helped me to get used to work in the Schanze group. Dr. Fude Feng and Dr. Zhen Fang always shared their knowledge and experience of scientific research with me and helped me to overcome difficulties. Dr. Yan Chen from Dr. Weihong Tan's group kindly trained me on the fluorescence correlation spectroscopy and also shared her experience in instrument construction. Dr. Dongping Xie, Zhuo Chen and Zhenxing Pan helped me with sample characterization and instruments using. I am also very grateful to Sile Hu from Department of Computer and Information Science and Engineering for being so supportive in LDA programming. It is also dedicated to Patrick Wieruszewski, Randi Price, and Russell Winkel for helping with my English writing. In addition, thanks to Dr. Anand Parthasarathy, Dr. Galyna Dubinina, Subhadip Goswami, Jie Yang and Shanshan Wang who have provided helps and suggestions for my Ph.D. study and research.

I would like to express my sense of gratitude to all my committee members: Dr. Ronald Castellano, Dr. Christopher Batich, Dr. Charles Cao, and Dr. David Powell for

their time and helpful suggestions. Thanks to Dr. Weihong Tan, Dr. Ronald K. Castellano, and Dr. Christopher Batich for their kindness in writing strong recommendation letters for me. In addition, Dr. Christopher Batich, who taught me much knowledge in polymer characterization when I spent my one year master study in Department of Materials Science and Engineering, still gave me many helps after I transferred to Department of Chemistry.

Finally, my family, especially my parents, to whom I am extremely grateful and indebted, always provides me the best for my life. Without their unceasing supports and loves, I would not stand here and be who I am today. Again, I place on record, my deepest gratitude to my parents for making my dreams come true.

TABLE OF CONTENTS

	<u>page</u>
ACKNOWLEDGMENTS	4
LIST OF FIGURES.....	10
LIST OF ABBREVIATIONS.....	16
ABSTRACT	22
 CHAPTER	
1 INTRODUCTION	24
Conjugated Polymers.....	24
Conjugated Polyelectrolytes (CPE).....	25
Fluorescence Quenching and Stern-Volmer Plot.....	27
Fluorescence Resonance Energy Transfer.....	31
Amplified Quenching and Molecular Wire Effect.....	32
Aggregation of Conjugated Polyelectrolytes	35
Environmental Effect on the Conformation of CPE	39
Sensing Assay Development of CPEs.....	43
Small Ions/Molecules Sensing.....	43
Metal ion sensing.....	44
Small molecule sensing	46
DNA Sensing.....	48
Protein/Enzyme Activity Sensing.....	51
Protein sensing by CPE based sensor.....	52
Enzyme activity sensing.....	55
Non-specific Interaction of CPEs	60
Sensor Array	61
Linear Discriminant Analysis.....	64
Fluorescence Correlation Spectroscopy (FCS).....	68
Basic Principle of FCS.....	68
Application of FCS.....	69
Overview of This Dissertation	70
2 CONSTRUCTION OF A FLUORESCENCE CORRELATION SPECTROSCOPY..	72
Theory of FCS	72
Construction of FCS System.....	77
Laser Optimization and Alignment.....	77
Blue (405 nm) diode Laser.....	77
Fiber coupling spatial filter and fiberport	79
Dichroic Mirror Cube and Laser Alignment.....	80
Objective Lens and Focusing	82

Signal Collection and Detection.....	84
Potential Interference	85
Calibration	86
Examination of FCS System	88
Summary	92
Materials and Methods.....	93
Materials.....	93
FCS Component and Measurement.....	93
3 THE APPLICATION OF DYE-LIGAND INTERCALATED HELICAL CONJUGATED POLYELECTROLYTE ON PROTEIN SENSING	95
Background.....	95
Results and Discussion.....	96
FRET Study of Helical CPE/dye-ligand with Protein.....	96
Photophysical properties of Poly-1 and biotin-TMR	96
FRET from Poly-1 to TMR.....	98
Addition of avidin to Poly-1/biotin-TMR	100
Titration of preformed avidin/biotin-TMR to Poly-1	101
FCS Study on the Poly-1/biotin-TMR/avidin System	103
Diffusion behavior of four types of molecules/complex	105
Mechanism for formation of supramolecular aggregation	108
Control experiment.....	109
Avidin sensing strategy	113
Conclusion	115
Experiments and Materials	116
Materials.....	116
Preparation of Poly-1/biotin-TMR complex.....	117
Negative Control Experiment by Using BSA.....	117
Instrumentation.....	118
FCS measurement.....	118
Fluorescence spectroscopy.	118
UV-Vis measurement.....	118
4 STUDY OF CONFORMATION CHANGE OF CPES INDUCED BY PROTEINS AND DEVELOPMENT OF SENSOR ARRAY FOR PROTEINS BY FCS	119
Background.....	119
Results and Discussion.....	121
Properties of Six CPEs and Seven Proteins.....	121
FCS Results and Discussion	124
Protein Sensing.....	130
Linear discriminant analysis of FCS diffusion times for protein/CPE mixtures	130
Unknown sample test.....	134
Summary	137
Material and Experiment.....	138

Materials.....	138
Bradford Protein Assay Procedure	139
Instrumentation.....	140
FCS measurement.....	140
UV-Vis measurement.....	140
5 STUDY OF INTERACTION OF META-LINKED POLY(PHENYLENE ETHYNYLENE) SULFONATE CONTAINING PYRIDINE WITH METAL IONS	141
Background.....	141
Results and Discussion.....	143
Photophysical Properties of mPPESO ₃ py	143
Solvent-induced photophysics change.....	143
Palladium ion-induced photophysics change	146
Photophysics change of mPPESO ₃ py with various metal ions	148
FCS Study on the mPPESO ₃ py with Various Metal Ions.....	150
Summary	153
Experimental.....	154
Materials.....	154
Instrumentation.....	154
Absorption and Emission measurement	154
FCS measurements	155
6 CONCLUSION.....	156
The Application of Dye-Ligand Intercalated Helical Conjugated Polyelectrolyte to Protein Sensing	156
New Fluorescence Correlation Spectroscopy and Application on Protein Sensor Array Development.....	157
Study of <i>meta</i> -Linked Poly(Phenylene Ethynylene) Sulfonate Containing Pyridine Quenched by Metal Ions.....	158
Outlook for Application of FCS in CPE.....	158
APPENDIX	
A TABLES OF TRAINING DATA	160
B TABLE OF TEST DATA.....	164
LIST OF REFERENCES	166
BIOGRAPHICAL SKETCH.....	180

LIST OF TABLES

<u>Table</u>	<u>page</u>
3-1 Photophysical properties of TMR, Poly-1, and biotin-TMR in 10 mM phosphate buffer solution (pH 7.4).	98
3-2 Diffusion data for four species in phosphate buffer (10 mM, pH 7.4).....	106
4-1 Basic information of CPEs.....	122
4-2 Basic information of proteins.	124
4-3 Eigenvalues with their percentage of each LDA operation training matrix.....	133
A-1 Training matrix of $\text{Log}(\tau_d/\tau_0)$ of six CPE sensor array (P1 – P6) against seven proteins.	160
B-1 Unknown sample test matrix of $\text{Log}(\tau_d/\tau_0)$ of 6 CPE sensor array (P1 – P6) against various proteins.....	164

LIST OF FIGURES

<u>Figure</u>	<u>page</u>
1-1 Structures of commonly used conjugated polymers.	25
1-2 Normalized absorption and emission spectra of perylene in benzene with corresponding electronic energy diagram.....	27
1-3 The pH-dependent absorption and emission spectra of fluorescein.....	28
1-4 Mechanism and Stern-Volmer plot of A) collisional quenching and B) static quenching (right).....	30
1-5 Schematic representation of the FRET spectral overlap integral and energy diagram.	31
1-6 Schematic illustration of amplified fluorescence quenching of a conjugated polymer by MV^{2+}	32
1-7 Illustration of the molecular wire.	33
1-8 Absorption and fluorescence spectra of MPS-PPV in water in the presence and absence of MV^{2+}	34
1-9 Structure of some polymers that used in the text.....	34
1-10 Stern-Volmer plots of a series of PPE-CO ₂ with $[MV^+]$	35
1-11 A) Absorption and fluorescence spectra of PPE-NH ₃ with increasing $[PPI]$. B) Structure of PPE- ^d NH ₃ and PPI.	36
1-12 Illustration of amplified quenching by oppositely charged quencher in A) non-aggregated CPE B) aggregated CPE.	37
1-13 Structure of MV^{2+} and MBL-PPV and Stern-Volmer plot for MBL-PPV quenched by MV^{2+}	38
1-14 Quenching of 10 μ M PPE-CO ₂ ⁻ emission by MV^{2+} in water (■) and in methanol with 0 μ M (□), 2.5 μ M (○), 5.0 μ M (◇), 7.5 μ M (Δ), or 10.0 μ M (∇) CaCl ₂	38
1-15 Absorption (left) and fluorescence (right) spectra of PPE-SO ₃ in MeOH (—), (1:1) H ₂ O-MeOH (--), and H ₂ O (-••-).	40
1-16 Solvent effect on the aggregation state of CPE.	40

1-17	Structures of OPEs studied by Moore's group and a space-filling model showing the conformational equilibrium for OPE of length $n = 18$	42
1-18	A) Normalized emission spectra of OPE in various solvents. Insert: absorption spectra. B) Structure of OPE and cartoon for coil-helix transition process.	42
1-19	Schematic illustration of Hg^{2+} -induced agglutination of the h-PPE- CO_2 /papain complex.	44
1-20	A) Sensing strategy for aptamer mediated CPE based K^+ sensor. B) Absorption spectra and visible colors of polythiophene mixed with different ions.	46
1-21	A) Interaction between p-BV $^{2+}$ and sugar. B) Fluorescence recovery titration curves against three sugars.	47
1-22	Photographs, possible structure and UV-Vis absorption spectra changes for the PT based DNA sensor	48
1-23	Schematic illustration of DNA detection by CPE labeled molecular beacon.	50
1-24	Chemical structures of quenchers or ligands.	53
1-25	Whitten's quencher-tether-ligand based "turn-on" strategy for avidin sensing.	53
1-26	Schematic description of the specific detection of human α -thrombin by use of ssDNA thrombin aptamer and cationic polymer.	54
1-27	Mechanism of the "turn-on" and "turn-off" CPE-based sensors.	55
1-28	A) Structures of polymer, BpPPESO $_3$ and substrate, 10CPC, and reaction scheme for hydrolysis of 10CPC by PLC. B) Mechanism of PLC turn-off assay.	59
1-29	Mechanism of ALP turn-off assay and photographs of solutions illuminated with near-UV light illustrating the polymer fluorescence under the different conditions of the assay.	60
1-30	Schematic presentation of the cell detection assay by CPEs including signal response pattern and canonic score plot.	63
2-1	Working principle for FCS.	73
2-2	The excitation volume in A) Z direction and B) X-Y planar as generated by a diffraction-limited objective lens.	74
2-3	development of an autocorrelation curve.	74

2-4	Ellipsoid-like excitation volume formed by the objective lens.	75
2-5	Schematic diagram of the FCS setup described in the text.	78
2-6	Photographs for A) excitation part of FCS setup and B) fiber coupling spatial filter.....	79
2-7	Cross-sections for laser beam in each optimization step.....	80
2-8	A) Inner structure of fluorescence microscope and B) photograph for a part of the setup.....	81
2-9	Diagram of the dichroic mirror cube.....	81
2-10	Effect of objective media A) oil immersion objective B) water immersion objective.	83
2-11	Photographs for signal detection and correlation components of FCS setup.	84
2-12	Confocal volume and optics.....	85
2-13	Black cover and breadboard for FCS setup.....	86
2-14	Structure of molecules that used in calibration and their acronyms.....	88
2-15	Correlation curves for TMR in water.	89
2-16	Effect of molecular weight (MW) on the correlation curves of molecules A) using 590 nm emission filter, B) using 500 nm emission filter.	91
2-17	Plot of diffusion coefficient of four standard samples as a function of their molecular weight.....	92
3-1	Structure of polymers and dye-ligand compound.	97
3-2	Absorption (Abs) and emission (Em) spectra of Poly-1 and biotin-TMR.....	97
3-3	Normalized emission spectra for titration of 0-0.3 μ M biotin-TMR into 15 μ M Poly-1 in 1 mM phosphate buffer solution, pH = 7.4.	98
3-4	Normalized fluorescence spectra ($\lambda_{\text{ex}} = 320$ nm) of biotin-TMR (225 nM) in the absence (—) and presence (---) of Poly-1 (15 μ M) in aqueous phosphate buffer.	99
3-5	Fluorescence anisotropy spectra for biotin-TMR with and without Poly-1.	99
3-6	Fluorescence spectra of Poly-1 solution (—) upon addition of biotin-TMR (•••) and avidin (---).	100

3-7	Normalized emission spectra for Poly-1 mixed with preformed avidin/biotin-TMR at various [avidin]/[biotin-TMR].	101
3-8	Ratio of intensities at 590 nm and 450 nm after addition of pre-mixed biotin-avidin complex at various avidin concentrations in phosphate buffer	102
3-9	Binding of preformed avidin/biotin-TMR complex to Poly-1 as a function of added avidin concentration.....	103
3-10	Basic setup for FCS with 543 nm Laser.	104
3-11	Background detection for A) phosphate buffer (10 mM, pH 7.4) B) Poly-1 (1 μ M) in phosphate buffer (10 mM, pH 7.4).....	104
3-12	Normalized correlation functions of biotin-TMR, Poly-1/biotin-TMR, biotin-TMR/avidin, and Poly-1/biotin-TMR/avidin	105
3-13	Normalized correlation functions of biotin-TMR, Poly-2/biotin-TMR, Poly-2/biotin-TMR/avidin and biotin-TMR/avidin	106
3-14	Photon counting rate (fluorescence fluctuation) during the detection time (1200 s) for Poly-1/biotin-TMR and Poly-1/biotin-TMR/avidin.....	107
3-15	Proposed mechanism of protein-induced aggregation.	108
3-16	AFM images for A) pure Poly-1 B) Poly-1/biotin-TMR C) Poly-1/biotin-TMR/avidin Line scans for D) pure Poly-1 E) Poly-1/biotin-TMR F) Poly-1/biotin-TMR/avidin.....	109
3-17	Normalized correlation functions of biotin-TMR, Poly-1/biotin-TMR, and Poly-1/biotin-TMR/avidin.....	110
3-18	Normalized correlation functions for ligand-free TMR with and without avidin..	111
3-19	Normalized correlation curves for Poly-1/TMR and Poly-1/TMR/avidin in 10mM phosphate buffer A) pH 7.4 B) pH 10.5.....	112
3-20	AFM images for A) Poly-1/avidin and B) Poly-1/TMR/avidin Line scans for C) Poly-1/avidin and D) Poly-1/TMR/avidin.	112
3-21	Normalized correlation functions for biotin-TMR, Poly-1/biotin-TMR and Poly-1/biotin-TMR/BSA.....	113
3-22	Normalized correlation functions for biotin-TMR, Poly-1/biotin-TMR, and Poly-1/biotin-TMR/avidin	114
3-23	Autocorrelation FCS curves for Poly-1/biotin-TMR, Poly-1/TMR/avidin and Poly-1/biotin-TMR/avidin	115

4-1	Chemical structures of six CPEs.	122
4-2	Normalized absorption and emission spectra for six CPEs.	123
4-3	FCS curves for P4 without protein (■) and with avidin (●) LYZ (▲)HRP (▼) HK3 (►) BSA (◆) PLD2 (◄) GOx (★) in 5 mM HEPES buffer pH 7.2..	125
4-4	Fluctuation profiles for A) P4 without and with seven proteins and B) their enlargement	126
4-5	Log (τ_d/τ_0) response 2D bar pattern of six CPEs mixing with seven proteins.. .	127
4-6	Log (τ_d/τ_0) response 3D column pattern of six CPEs mixing with seven proteins.....	128
4-7	Flowchart for protein sensor array development.....	130
4-8	Flowchart of multiple LDA operation for training known samples.	132
4-9	LDA discriminant spaces/plots for the diffusion time response patterns.....	133
4-10	Training results for multiple LDA operation of diffusion time response for six CPE probes against seven proteins	134
4-11	Flowchart for multiple LDA operation for testing unknown samples.	135
4-12	Test results for multiple LDA operation of diffusion time response for six CPE probes against forty-two unknown protein samples.....	136
5-1	Structure of mPPESO ₃ py.....	142
5-2	A) Absorption spectra for mPPESO ₃ py in solvent mixture with different component volume ratio. B) Ratiometric plot of A_L/A_S versus the percentage of water in methanol..	144
5-3	A) Mechanism of solvent- and metal ion-induced formation of helical structures. B) Mechanism of multi-valence metal ion-induced crosslinking of CPE.	145
5-4	A) Emission spectra for mPPESO ₃ py in solvent mixture with different component volume ratio. B) Absorbance ratio of two bands versus the percentage of water in MeOH.....	146
5-5	A) Absorption spectra of 15 μ M mPPESO ₃ py titrated with Pd ²⁺ . B) The absorbance ratio of two bands versus the concentration of Pd ²⁺ in aqueous solution.	147

5-6	Emission spectra for 15 μM mPPESO ₃ py with various [Pd ²⁺] in aqueous solution.....	148
5-7	Stern-Volmer plots for mPPESO ₃ py with various metal ions in water.....	149
5-8	Stern-Volmer constant for various metal ions in water.	149
5-9	Bar graph for fluorescence quenching ratios I_0/I at 680 nm of mPPESO ₃ py with different metal ions at various concentrations in aqueous solution..	150
5-10	A) FCS correlation curves and B) fluctuation profiles for 15 μM mPPESO ₃ py without (red) and with 40 μM Pd ²⁺ (green) or Cr ³⁺ (blue).....	151
5-11	Diffusion time ratio for mPPESO ₃ py with different amount of Pd ²⁺ measured for 30 min in aqueous solution.....	152
5-12	Diffusion time ratio of mPPESO ₃ py before and after the addition of metal ions.....	153

LIST OF ABBREVIATIONS

\bar{v}	Specific gravity
η	Viscosity of the solvent
$\langle F \rangle$	Average fluorescence intensity
10CPC	Phosphatidylcholine
2D	Two dimension
3D	Three dimension
A	Absorbance
Abs	Absorption
ADP	Adenosine diphosphate
AFM	Atomic force microscopy
A_L	Absorbance at the longer wavelength band
ALP	Alkaline phosphatase
AMP	Adenosine monophosphate
APD	Single-photon counting avalanche photodiode
A_S	Absorbance at the shorter wavelength band
ATP	Adenosine triphosphate
Biotin-TMR	Biotinylated rhodamine, 5-(and-6)-tetramethylrhodamine biocytin
BpPPESO ₃	Biphenyl sulfonated poly(para-phenylene ethynylene)
BSA	Bovine serum albumin
Bz-FVR-pNA	N-benzoyl-Phe-Val-Arg- <i>p</i> -nitroanilide hydrochloride hydrate
C	Concentration
CaM	Calmodulin
CNC	Charge-neutral complex
CO ₂ ⁻	Carboxylate

CP	Conjugated polymer
CPE	Conjugated polyelectrolyte
Cyt <i>c</i>	Cytochrome <i>c</i>
<i>D</i>	Diffusion coefficient
Dabcyl	4-(4-(Dimethylamino) phenylazo) benzoic acid
DAG	Degraded product of 10CPC
d_{laser}	Diameter of laser beam
DLS	Dynamic light scattering
DMSO	Dimethylsulfoxide
DNA	Deoxyribonucleic acid
$d_{pupille}$	Diameter of lens pupil
dsDNA	Double stranded DNA
EB	Ethidium bromide
ELISA	Enzyme linked immunosorbent assay
Em	Emission
ET	Energy transfer
$F(t)$	Fluorescence intensity at time
FCS	Fluorescence correlation spectroscopy
FRET	Fluorescence resonance energy transfer
FWHM	Full width half maximum
$G(\tau)$	Autocorrelation function
GFP	Green fluorescence protein
GOx	Glucose oxidase from <i>Aspergillus niger</i>
HEPES	4-(2-Hydroxyethyl)-1-piperazineethanesulfonic acid

HK3	Hexokinase from <i>saccharomyces cerevisiae</i> , type III
h-PPE-CO ₂	<i>homo</i> -Carboxylate-substituted poly(phenylene ethynylene)
HRP	Peroxidase from horseradish, type I
<i>I</i>	Fluorescence intensity with quencher
<i>I</i> ₀	Fluorescence intensity without quencher
ICP-MS	Inductively coupled plasma mass spectrometry
<i>k</i>	Boltzmann's constant
<i>K</i> _{assoc}	Association constant for formation of the fluorophore-quencher complex
<i>K</i> _b	Binding constant
<i>K</i> _D	Dynamic constant
K-pNA	L-Lys- <i>p</i> -nitroanilide dihydrobromide
<i>k</i> _q	Bimolecular quenching rate constant
<i>K</i> _{SV}	Stern-Volmer constant
LDA	Linear discrimination analysis
LED	Light-emitting diode
LYZ	Lysozyme
MB	Molecular beacon
MeOH	Methanol
mPPESO ₃ py	Sulfonated PPE containing meta-linked pyridine rings in the backbone
MPS-PPV	Sulfonated poly(phenylene vinylene)
MV ⁺	Monovalence methyl viologen
MV ²⁺	Methyl viologen
MW	Molecular weight
MWCO	Molecular weight cutoff

N	Number of fluorophore in confocal volume
NA	Numerical aperture of objective lens
NR ₃ ⁺	Quarternary ammonium
OPE	Oligo(phenylene ethynylene)
P1	Poly(para-phenylene ethynylene) with polyethynylene glycol and polydendric ammonia side chains
P2	Sulfonated <i>meta</i> -linked poly(phenylene ethynylene)
P3	Sulfonated <i>para</i> -linked poly(poly(phenylene ethynylene)
P4	Cationic poly(thiophene phenylene) with bis-alkylammonium side groups
P5	Cationic poly(thiophene phenylene) with quaternary ammonia side chains
P6	Cationic Poly(para-phenylene ethynylene) with bis-alkylammonium side groups
PA	Polyacetylene
PANI	Polyaniline
<i>p</i> -BV ²⁺	Boronic acid functionalized benzyl viologen
PE-CO ₂	Oligomer carboxylated para-phenylene ethynylene
PEG	Polyethynylene glycol
PET	Photoinduced electron transfer
PF	Polyfluorene
PFP-CO ₂	Carboxylated poly(fluorene-co-phenylene)
<i>p</i> I	Isoelectrical point
PLC	Phospholipase C
PLD2	Phospholipase D from arachis hypogaea (peanut), type II
<i>p</i> -NA	<i>p</i> -nitroanilide

PO_3^{2-}	Phosphonate
Poly-1	Sulfonated <i>meta</i> -linked poly(phenylene ethynylene)
Poly-2	Sulfonated <i>para</i> -linked poly(poly(phenylene ethynylene))
PPE	Poly(para-phenylene ethynylene)
PPE-CO ₂	Carboxylated poly(para-phenylene ethynylene)
PPE- ^d NH ₃	Cationic poly(para-phenylene ethynylene) with dendric ammonia side chains
PPE-PEG- ^d CO ₂	Poly(para-phenylene ethynylene) with polyethynylene glycol and polydendric ammonia side chains
PPE-PEG- ^d CO-DNA	DNA conjugated PPE-PEG- ^d CO ₂
PPE-PO ₃	Phosphonate-substituted poly(para-phenylene ethynylene)
PPE-SO ₃	Sulfonated poly(para-phenylene ethynylene)
PPi	Pyrophosphate
PPP	Poly(para-phenylene)
PPV	Poly(para-phenylene vinylene)
PPy	Polypyrrole
PRU	Repeat unit concentration
PT	Polythiophene
Q	Quencher
QTL	Quencher-tether-ligand
R	Radius of a sphere
R _H	Hydrodynamic radius
Rho-Arg	Emissive peptide-derivative rhodamine
Rho-Arg ₂	Non-emissive peptide-derivative rhodamine
Ru(bpy) ₂ (dppz) ²⁺	Ruthenium complex (bpy = 2,2'-bipyridine and dppz = dipyrdo[3,2-a:2',3'-c] phenazine)

Ru(phen)_3^{4-}	Ruthenium complex ((phen)=4,7-bis(4-sulfophenyl)-1,10-phenanthroline)
SM	Single mode
SNP	Single nucleotide polymorphism
SO_3^-	Sulfonate
ssDNA	Single strand DNA
SV	Stern-Volmer
T	Temperature
TCSPC	Time Correlated Single Photon Counting
TMR	Tetramethylrhodamine
UV-Vis	Ultra violet and visible
V	Volume of molecule
V_{eff}	Effective detection volume
λ_{ex}	Excitation wavelength
$\delta F(t)$	Deviation of the fluorescence intensity from $\langle F \rangle$ at time t
ε	Molar absorptivity or extinction coefficient
ϕ_{fl}	Quantum yield
λ_{max}	Wavelength of maximum emission peak
τ	Decay lifetime of fluorophore
τ_0	Initial diffusion time
τ_{D}	Diffusion time of a fluorophore
τ_{d0}	Diffusion time of pure CPE
ω	Structure parameter
ω_{r}	Transversal or waist radius of confocal volume
ω_{z}	Longitudinal radius of confocal volume

Abstract of Dissertation Presented to the Graduate School
of the University of Florida in Partial Fulfillment of the
Requirements for the Degree of Doctor of Philosophy

INVESTIGATION OF CONJUGATED POLYELECTROLYTES AND THEIR PROTEIN
SENSING BY FLUORESCENCE CORRELATION SPECTROSCOPY

By

Danlu Wu

December 2012

Chair: Kirk S. Schanze
Major: Chemistry

Conjugated polyelectrolytes (CPEs) are water-soluble polymers characterized by π -conjugated backbones with ionic side groups. By possessing favorable optical properties, charge interaction ability and solvent-dependent self-assembly, this class of polymers has been studied for chemical and biological sensor applications.

A DNA intercalator biotin-tetramethylrhodamine (biotin-TMR) is found to be capable of intercalating into a helical conjugated polyelectrolyte. Efficient fluorescence resonance energy transfer (FRET) from the polymer to the TMR chromophore is observed. It can be disrupted by mixing of biotin-TMR with avidin prior to the addition of the polymer. A discontinuous sensing strategy is developed for avidin with sensitivity as low as 100 pM. This project is further studied by a 543 nm laser coupled fluorescence correlation spectroscopy (FCS), which can provide insight regarding diffusion behavior and size change of molecules. A remarkable increase in the diffusion time of the poly-1/biotin-TMR complex in the presence of avidin is observed. This change is attributed to the formation of large supramolecular polymer aggregates, giving rise to a sensitive detection method for avidin with detection limit < 100 pM.

An FCS system coupled with 405 nm blue laser, which can directly track the diffusion of CPE, is successfully built up in house. A detailed construction of such type of FCS along with troubleshooting, optimizing and calibrating are fully described. This FCS setup is employed in the investigation on an array-based protein sensing project. A series of CPEs is developed as a probe array and exposed to seven proteins. The diversity in the final molecular sizes and diffusion times of the CPE probes is revealed through FCS. The chemometric linear discriminant analysis (LDA) is employed to differentiate different protein groups and identify unknown protein samples. The high discriminant/recognition accuracy (~93%) verified the feasibility of this new sensor array.

In the last project, a CPE (mPPESO₃py) containing meta-linked pyridine rings in the backbone is developed as a Pd²⁺ sensor. The polymer shows a great affinity and selectivity for the Pd²⁺ ion for that the quenching efficient of Pd²⁺ on polymer emission greatly surpasses that of the other metal ions. The FCS study discovers that aggregation of mPPESO₃py is induced when several multivalent metal ions, except Pd²⁺, are added into the system. While shorter diffusion time is observed for CPE/Pd²⁺. The quenching mechanism of Pd²⁺ on mPPESO₃py is dominated by charge transfer instead of aggregation.

CHAPTER 1 INTRODUCTION

Conjugated Polymers

In chemistry, the conjugation means an overlap of one π -orbital with another across an intervening sigma bond (in larger atoms d-orbitals can be involved).¹ A conjugated system is a system comprising a region of overlapping π -orbital bridged with interjacent single bonds. The involved molecules generally have lower overall energy and higher stability. Those molecules may be cyclic, acyclic, linear or mixed, allowing their π electrons delocalize across all the adjacent aligned π -orbitals.²

Among the large number of conjugated systems, conjugated polymers (CPs) with alternating single and multiple bonds have attracted an overwhelming interest in laboratories around the world. In 1967, the first conjugated polymer polyacetylene (PA, Figure 1-1) was born in Hideki Shirakawa's lab of the University of Tsukuba in Japan,³ launching the investigation on this novel conductive material. Various conjugated polymers have been generated, such as poly(para-phenylene) (PPP),⁴ poly(para-phenylene vinylene) (PPV),⁵ poly(para-phenylene ethynylene) (PPE),⁶ polythiophene (PT),⁷ polypyrrole (PPy),⁸ polyaniline (PANI)⁹ and polyfluorene (PF)¹⁰ (Figure 1-1). One of the milestones is that in 2000, Hideki Shirakawa, Alan MacDiarmid (University of Pennsylvania) and Alan Heeger (University of California at Santa Barbara) were awarded the Nobel Prize for the discovery of conducting polyacetylene.¹¹ By possessing various well-designed functional groups, the CPs have favorable electrical, optical or magnetic properties, which offer them great potential in applications including light-emitting diodes (LED),^{5, 12} field-effect transistors,^{13, 14} solar cells¹⁵ and chemosensors.¹⁶ Among those applications, chemosensing is experiencing a rapid growth in the past few

years. A large part of this is driven by the need in the fields of medical diagnostics, environmental monitoring and toxicological analysis.

Generally speaking, a sensor in analytical chemistry is commonly defined to be a chemical indicator that produces a signal indicative of the presence of a target analyte.¹⁷ Consequently, CP has been demonstrated to be a versatile chemosensor, since their color (colorimetric),¹⁸ emission (fluorometric),¹⁶ conductivity (conductometric)¹⁹ or redox potential (potentiometric)²⁰ changes upon analyte binding. The diversity or variety in the CP sensor type is a result of amplified signal response due to the efficient coupling between optoelectronic segments^{21, 22} and the rapid transport of electronic excitations governed by the nature of conjugation.¹⁶

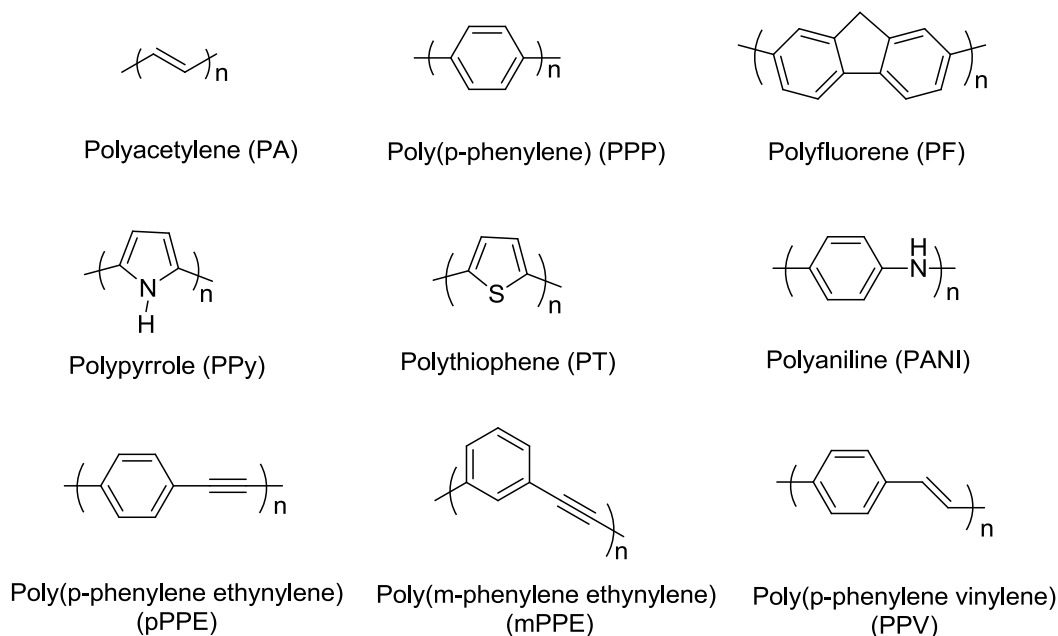


Figure 1-1. Structures of commonly used conjugated polymers.

Conjugated Polyelectrolytes (CPE)

Conjugated polyelectrolytes (CPEs) are water-soluble conjugated polymers characterized by π -conjugated backbones with various ionic side groups, such as

sulfonate (SO_3^-),^{23, 24} carboxylate (CO_2^-),²⁵ phosphonate (PO_3^{2-})²⁶ and quarternary ammonium (NR_3^+),^{27, 28} either branched^{25, 28} or linear.^{23, 24, 27, 29} CPEs possess not only attractive electrical or optical properties, but also charge interaction ability and solvent-dependent self-assembly. These features satisfy the requirement of sensor applied in the biological system or aqueous solutions.

The intrinsic amphiphilic nature of CPEs offers them various conformations in aqueous solution. For example, the *meta*-linked PPE with more than 4 repeat units tends to form helical structure in aqueous solution.^{23, 30} *para*-Linked PPEs with linear ionic groups undergo spontaneous aggregation in water,^{24, 29, 31} while some CPEs with high charge density, e.g., with branched ionic side chains, remain single polymer chain in water. The charge and structure nature of CPE facilitates the ability to control the distance and the strength of interaction between CPE and other ionic species. For instance, a rhodamine labeled ligand compound with net positive charge was found to intercalate into the helix of an anionic *meta*-linked PPE, forming a ligand functionalized complex.³⁰ Pyrophosphate (PPi) was demonstrated to induce aggregation of a monodisperse cationic poly(phenylene-ethynylene) with dendritic polyamine side chains through binding between the PPi and amine ligands in water.²⁸ CPEs are able to form complexes with oppositely charged surfactants via Coulombic attraction, which results in dramatic and tunable changes in both geometric conformation and optical properties of CPEs.³² It was also found from the optical aspect that proteins can modify the geometric conformation of CPEs via “non-specific” interactions.^{33, 34} The change in the chemical or physical properties of CPEs induced by other species provides a platform for sensor applications of these materials.

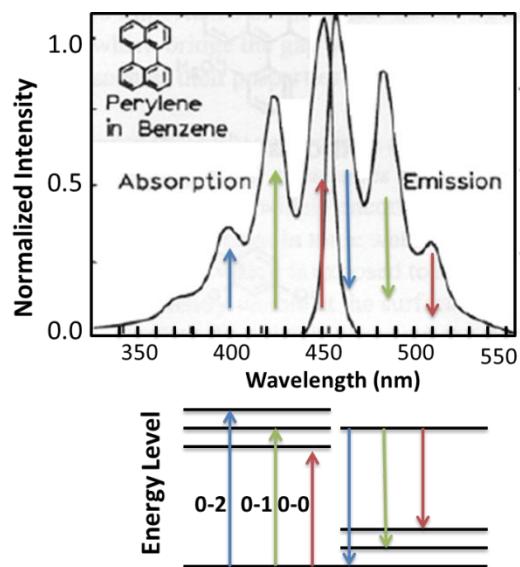


Figure 1-2. Normalized absorption and emission spectra of perylene in benzene with corresponding electronic energy diagram. Adapted with permission from Lakowicz, J. R.³⁵

Fluorescence Quenching and Stern-Volmer Plot

Fluorescence is the light emitted by a fluorophore after absorbing energy from excitation electromagnetic radiation, e.g., light. It occurs as the molecules relax from higher electronic singlet states. At each of the electronic energy levels there are several vibrational energy levels. The fluorophores can stay in a lower vibrational energy level through vibrational relaxation.³⁵ A typical absorption and emission spectra of an organic fluorophore with corresponding energy level diagram, is shown in Figure 1-2. The excited molecules usually relax to a lower vibrational state, so their fluorescence bands are shifted to wavelengths that are longer than the original band. This shift is termed the Stokes shift. A large Stokes shift can help to separate the excitation light and emission light. Usually, the average time a molecule spends in the excited state prior to return to the ground state is called lifetime (τ). The lifetime can be detected through a time correlated single photon counting (TCSPC) coupled fluorescence lifetime spectrometry and it has been used to analyze the physical state of the fluorophore as well as related

chemical reaction.³⁵ The way to characterize the emission efficiency of a fluorophore is to measure its quantum yield (ϕ_f), which is the number of emitted photons relative to the number of absorbed photons.³⁵

The absorption and emission spectra of some species change upon the change of surrounding chemical environments. For instance, the spectra of fluorescein, which is a synthetic organic compound available as a dark orange/red powder soluble in water, is pH-sensitive over the range of 5 to 9 as shown in Figure 1-3.³⁶ By making use of this property, its absorption and emission efficiency at a certain wavelength can be carefully tuned to achieve some particular purpose, which is applied in Chapter 2.

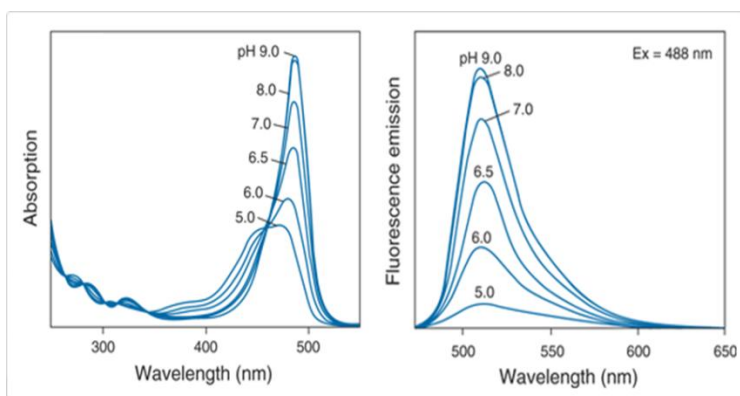


Figure 1-3. The pH-dependent absorption and emission spectra of fluorescein. Reprinted with permission from Invitrogen.³⁶

Fluorescence quenching, which refers to any process (fluorescence resonance energy transfer, electron transfer, intersystem crossing due to heavy atom effect, etc.) that reduces the fluorescence intensity of a fluorophore, is an important process that has been well utilized in many applications, especially in biosensors. Quenching can occur from many different mechanisms, among which, two mechanisms—dynamic and static quenching—are quite important and commonly seen. Dynamic quenching, also termed collisional quenching, occurs when the excited-state fluorophore is deactivated upon colliding with some other molecule, i.e., quencher, in solution. It is a diffusion-

limited process since the quencher must come into contact with the fluorophore, obtaining the energy of emitting photon within the lifetime of fluorophore at excited state. This results in the fluorophore returning to the ground state without emission of a photon. Static quenching occurs due to formation of a non-fluorescent ground-state complex by the fluorophore and the quencher. Quenching occurs in the ground state (Figure 1-4).³⁵

To qualify or quantify a quenching process, a Stern-Volmer (SV) plot and its slope, named Stern-Volmer constant K_{SV} , is normally employed. The SV equation is expressed as follows,

$$\frac{I_0}{I} = 1 + K_{SV}[Q] \quad (1-1)$$

where I_0 and I are the fluorescence intensity without and with quencher at a specific wavelength, usually the emission maximum of the fluorophore. $[Q]$ is the quencher concentration. In the simplest case, the plot is a straight line that has an intercept at

$\frac{I_0}{I} = 1$ with $K_{SV} > 0$, i.e., $I_0 > I$. In the situation of dynamic quenching mechanism,

$K_{SV} = k_q \tau = K_D$, where k_q is the bimolecular quenching rate constant (unit $M^{-1}s^{-1}$) and τ is the decay lifetime of the fluorophore (unit s). K_D is so called dynamic constant (unit M^{-1}). In the other case of static quenching mechanism, $K_{SV} = K_{assoc}$, where the latter term is the association constant for formation of the fluorophore-quencher complex.

There is a simple way to distinguish dynamic and static quenching process by observing the slope change of SV plot upon increasing experimental temperature. Due to the diffusion-dependent property of dynamic quenching, an increase in temperature will enhance quenching-the higher temperature, the more collision occurs-the K_{SV} thus increases. While in the other side, higher temperature will cause dissociation of

fluorophore-quencher complex, resulting in fluorescence recovery. A decrease in the slope of SV plot is observed (Figure 1-4).

Sometimes, an upward-curved SV plot appears, especially, when a large amount of quencher is added into the system. This non-linear plot is the results of combination of static and dynamic quenching effect. It can be described as follows:

$$\frac{I_0}{I} = (1 + K_D[Q])(1 + K_{assoc}[Q]) \quad (1-2)$$

This phenomenon is frequently observed for CPE quenching study, where the effect is named “superlinear quenching”.^{37, 38} K_{SV} is obtained by applying Equation 1-1 in fitting of the SV plot at low $[Q]$, where the plot is still linear.

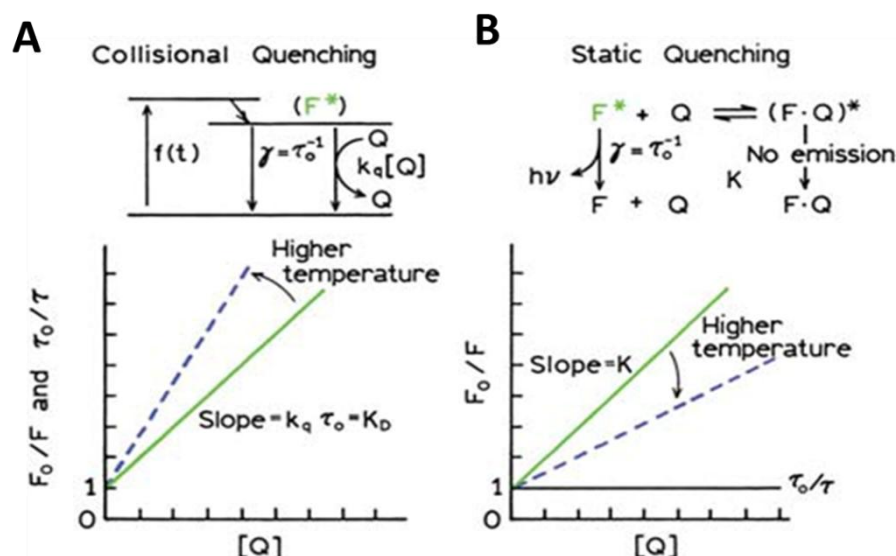


Figure 1-4. Mechanism and Stern-Volmer plot of A) collisional quenching and B) static quenching (right). F_0 and F are the same as I_0 and I described in the text. Reprinted with permission from Lakowicz, J. R.³⁵

Generally, K_{SV} reflects the quenching ability of the quencher on fluorophore, or, from a sensing aspect, it represents the sensitivity of a sensor/probe (fluorophore) against the analyte (quencher). A larger K_{SV} indicates that the sensor exhibits greater response when exposed to the analyte. Another way to think of the Stern-Volmer

constant is that its inverse ($1/K_{SV}$) is the concentration of analyte (quencher) producing 50% quenching on sensor molecule.

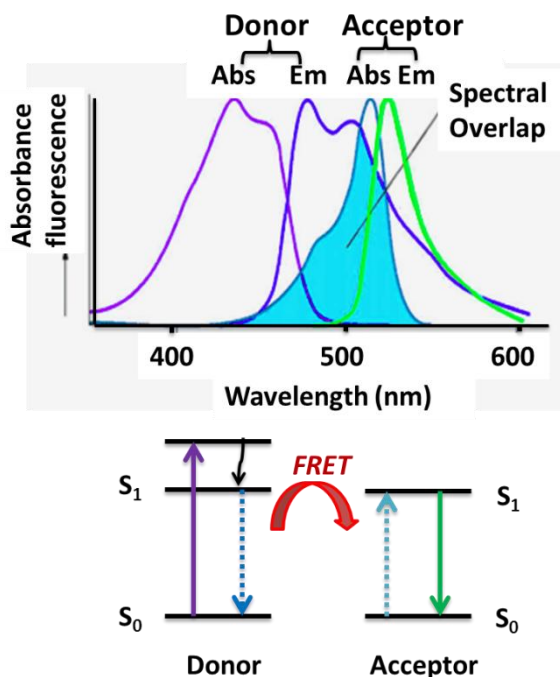


Figure 1-5. Schematic representation of the FRET spectral overlap integral and energy diagram. Adapted with permission from Lakowicz, J. R.³⁵

Fluorescence Resonance Energy Transfer

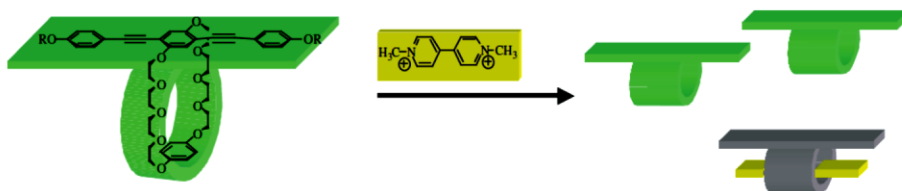
One of the important quenching processes is fluorescence resonance energy transfer (FRET), also named Förster resonance energy transfer. This process occurs whenever the emission spectrum of a fluorophore, called the donor, overlaps with the absorption spectrum of another molecule, called the acceptor (Figure 1-5). A donor chromophore, initially in its electronic excited state, transfers energy to an acceptor chromophore at ground state through nonradiative dipole–dipole coupling with little emission from the donor. If the acceptor is fluorescent, the emission belonging to the acceptor is observed. The efficiency of FRET is dependent on the inverse sixth power of the intermolecular distance, making it sensitive to detect the molecular proximity and

interaction between donor and acceptor.³⁹ This strategy has been fully utilized in the biological sensor development,⁴⁰ such as molecular beacon DNA probe.⁴¹

Amplified Quenching and Molecular Wire Effect

The term “amplified quenching” in fluorescent conjugated polymers was first proposed by Zhou and Swager.⁴² Their classic paper published in 1995 shows that a PPE featuring a number of crown-ether type functional groups, is quenched by the methyl viologen (MV^{2+} , Figure 1-6) 50 - 100 fold more efficiently compared to a small molecule featuring only one repeat unit with one crown-ether of PPE (Figure 1-6). The K_{SV} value for the polymer was $\sim 10^5 \text{ M}^{-1}$ whereas that for the small molecule counterpart was $\sim 10^3 \text{ M}^{-1}$. The authors explained that the conjugated polymer resembles a molecular wire, along which the exciton, a quasiparticle that delocalizes at the excited state, is smoothly diffusing until it encounters the first electron-accepter MV^{2+} that binds efficiently to the crown-ether portion. So that one single MV^{2+} can adequately quench a large number of exciton producers, creating the amplified quenching event. This also gave rise to the concept “molecular wire” effect as shown in Figure 1-7.

Monomeric chemosensor: sensitivity determined by the equilibrium constant



Receptor wired in series: amplification due to a collective system response

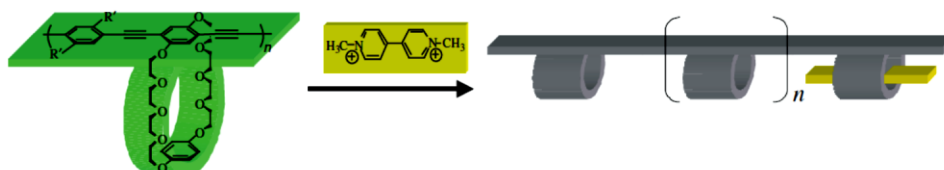


Figure 1-6. Schematic illustration of amplified fluorescence quenching of a conjugated polymer by MV^{2+} . Reprinted with permission from Zhou, Q., *et al.*⁴²

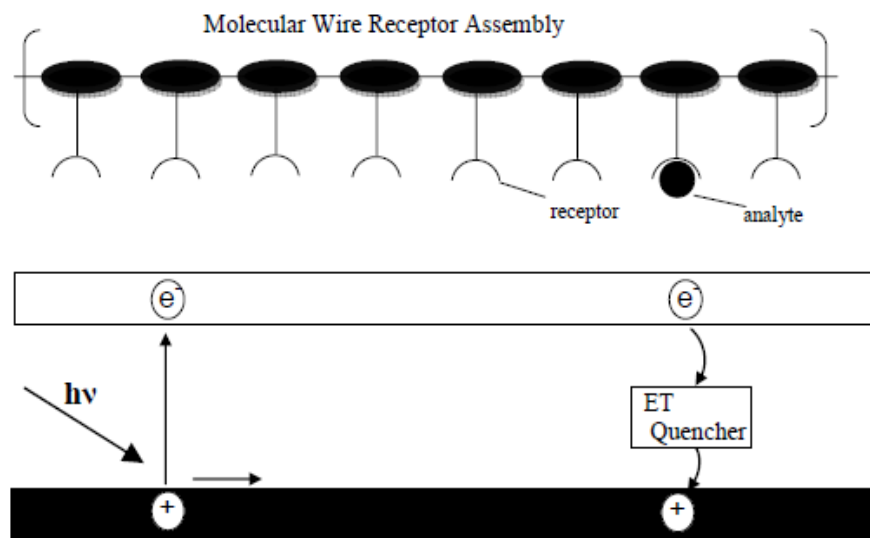


Figure 1-7. Illustration of the molecular wire. Adapted with permission from Zhou, Q. *et al.*⁴²

A few years later, Whitten and co-workers discovered that very efficient amplified quenching occurred to an anionic poly(phenylene vinylene) CPE (MPS-PPV, Figure 1-8) when mixed with the oppositely charged MV^{2+} electron acceptor.⁴³ The ion-pairing between the CPE and quencher ion mediates the photoinduced electron transfer, so that the exciton transporting within the CPE single chain, or clusters due to aggregation, can be efficiently and immediately trapped by the electron-deficient MV^{2+} , resulting in quenching amplification. The reported K_{SV} is $1.7 \times 10^7 \text{ M}^{-1}$, which is nearly six orders of magnitude greater than that for stilbene, which has the similar structure with that of PPV monomer. Subsequent to the Whitten paper, a number of groups quickly showed that the amplified quenching effect is general when fluorescent CPEs are quenched by oppositely charged ions.^{24, 37, 44} In 2008, Schanze and coworkers³¹ conducted an investigation on the effect of length of CPE (PPE- CO_2 , Figure 1-9) on the quenching efficiency of a monovalent quencher methyl viologen (MV^+) in methanol. They synthesized a series of PPE- CO_2 with various repeat unit number ($n = 7, 13, 35, 49,$

108) and these polymers are believed to be molecularly dissolved in the methanol. The quenching study shows that for low and moderate CPE polymerization degree, the K_{SV} systematically increases as polymers chain extend, saturating at a value of ~ 40 polymer repeat units (Figure 1-9), which suggests that a singlet exciton is able to effectively migrate a PPE chain with length of ~ 80 phenylene ethynylene units during its lifetime.

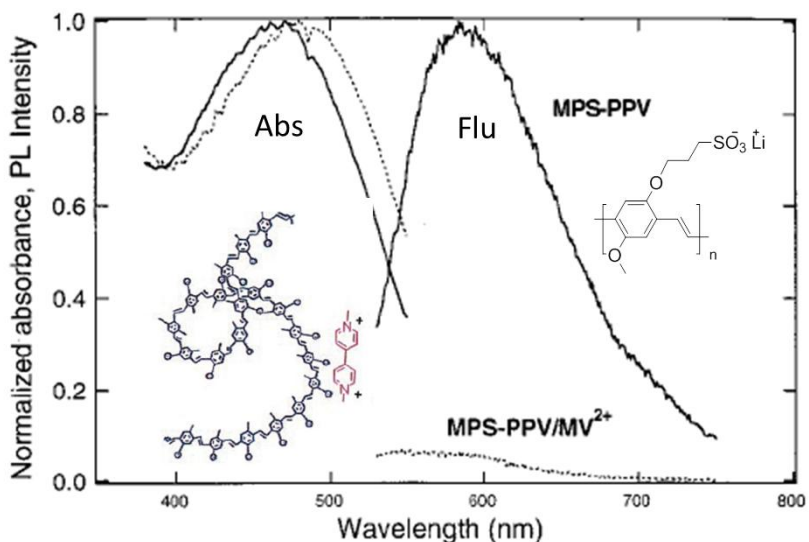


Figure 1-8. Absorption and fluorescence spectra (excited at 500 nm) of MPS-PPV (1.7×10^{-5} M in monomer repeat units) in water in the presence (dotted line) and absence (solid line) of MV^{2+} (1×10^{-7} M). Reprinted with permission from Chen, L. H., *et al.*⁴³

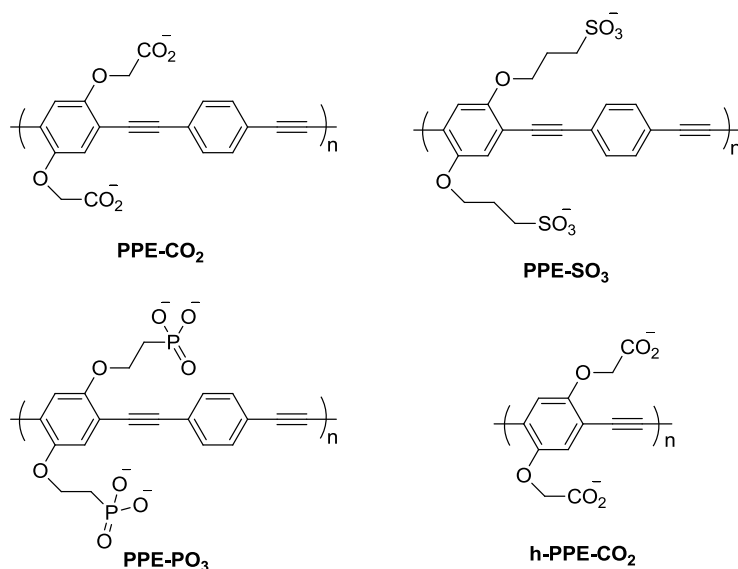


Figure 1-9. Structure of some polymers that used in the text.

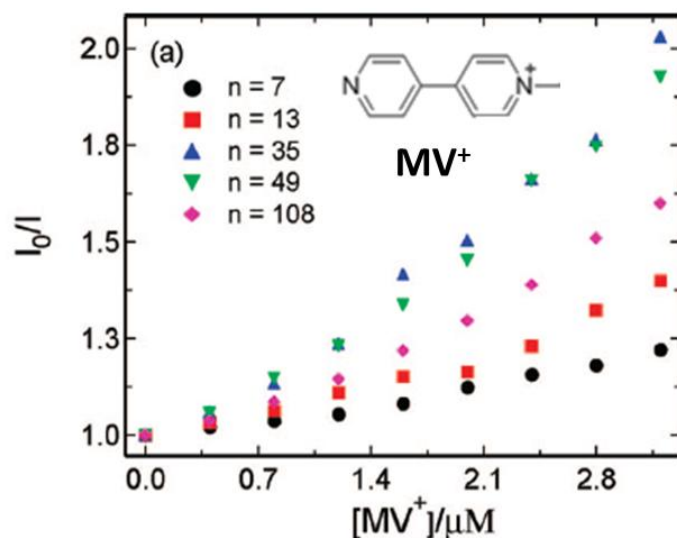


Figure 1-10. Stern-Volmer plots of a series of PPE-CO₂ with [MV⁺]. Reprinted with permission from Zhao, X. Y., *et al.*³¹

Aggregation of Conjugated Polyelectrolytes

One important property of CPEs is their self-assembly in various environments. Due to its highly hydrophobic rigid backbone and hydrophilic ionic side chains, CPEs tend to aggregate in polar solvents via π - π stacking interaction between the phenyl groups while remaining soluble. Once aggregated, the absorption and emission spectra are changed because the inter-chain conjugation has much lower energy state than that of the intra-chain conjugation. A red-shift in both absorption and emission bands is observed. In 2010, Zhao and Schanze²⁸ reported that PPI, a anionic biomolecule, can greatly induce aggregation of a cationic PPE with dendritic ammonia side chains (PPE-^dNH₃, Figure 1-11B). The absorption of PPE was dominated by a 430 nm instead of 400 nm (Figure 1-11A left). Attenuation in the emission intensity and a change from a sharp fluorescence peak at 430 nm to a broad band around 520 nm indicate that the polymer is undergoing a transform from “free polymer chain” to “aggregated polymer” (Figure 1-11A right). A blue-to-green color transition, which corresponds to the switch from non-

aggregation to aggregation state, can be directly observed by eye under the UV illumination (insert in Figure 1-11A).

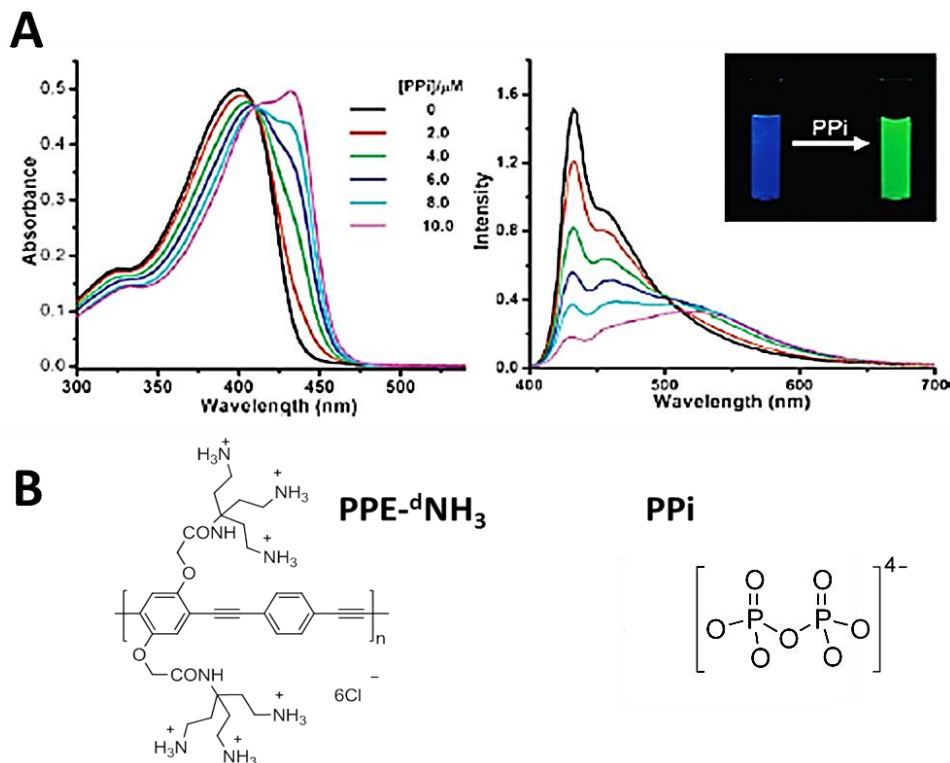


Figure 1-11. A) Absorption and fluorescence spectra of PPE-NH₃ with increasing [PPI]. Inset: fluorescence emission of the solution before and after the addition of PPI. B) Structure of PPE-dNH₃ and PPI. Reprinted with permission from Zhao X. Y., *et al.*²⁸

It is well evident that aggregation of CPEs will significantly influence the fluorescence quenching process. Whitten and co-workers⁴³ found that MPS-PPV is ion-paired with the quencher MV²⁺ to form a crosslinked structure, which allows the inter-chain exciton migration and trapping. Due to the dual function of the viologen in the quenching process, the quenching efficiency of MV²⁺ is greatly enhanced. Upon calculation, a single quencher MV²⁺ can quench ~1000 repeat units of MPS-PPV. Based on the amplification factor reported by Schanze (~80 phenylene ethynylene repeat unit

per quencher) for a single polymer chain, the huge value 1000 was the result of the combined effect of intra-chain and inter-chain electron transfer (Figure 1-12).

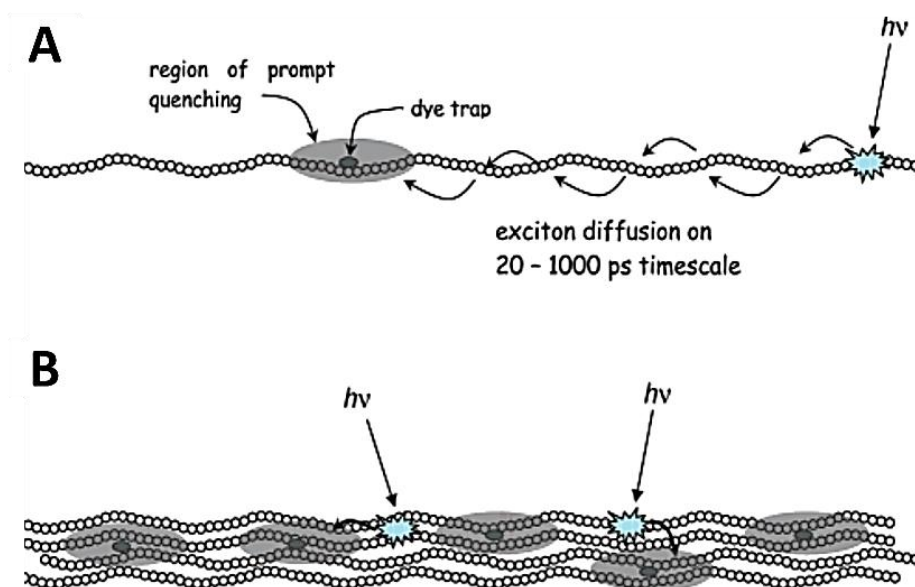


Figure 1-12. Illustration of amplified quenching by oppositely charged quencher in A) non-aggregated CPE B) aggregated CPE. Reprinted with permission from Tan, C. Y., *et al.*⁴⁵

A superlinear phenomenon on the SV plot was reported by Heeger and Bazan.^{37,}
³⁸ When a large amount of MV^{2+} was added into the polymer solution, an upward deviation was observed in the high [quencher] range in SV plot (Figure 1-13). They explained this property as a "sphere-of-action" quenching model.⁴⁶ That is when a quencher is within the quenching sphere, the quenching of fluorophores by the "apparent static" quencher is at nearly 100% efficiency. The tendency for ion-pairing between the fluorophores and quencher through electrostatic attraction enhances the local concentration of quencher around the large space that the polymer occupies. So there is always a quencher ion within a charge transfer distance, i.e., "sphere-of-action" of the polymer, leading to the superlinear quenching process. The higher the quencher concentration, the more pronounced this phenomenon.

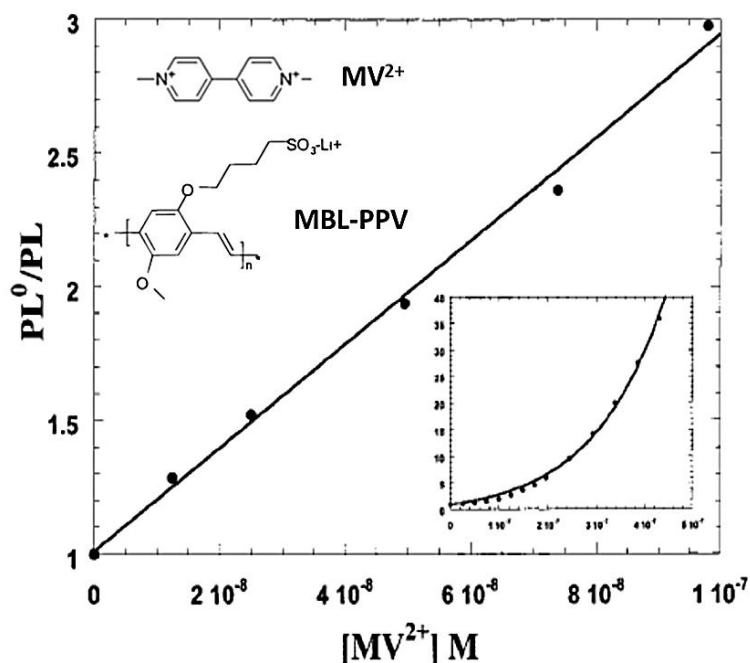


Figure 1-13. Structure of MV^{2+} and MBL-PPV and Stern-Volmer plot for MBL-PPV quenched by MV^{2+} with $[MV^{2+}]$ from 1×10^{-8} to 1×10^{-7} M. Inset: the same plot extended to higher MV^{2+} concentrations (from 1×10^{-8} to 4.3×10^{-7} M). Reprinted with permission from Eftink, M. R., *et al.*³⁴

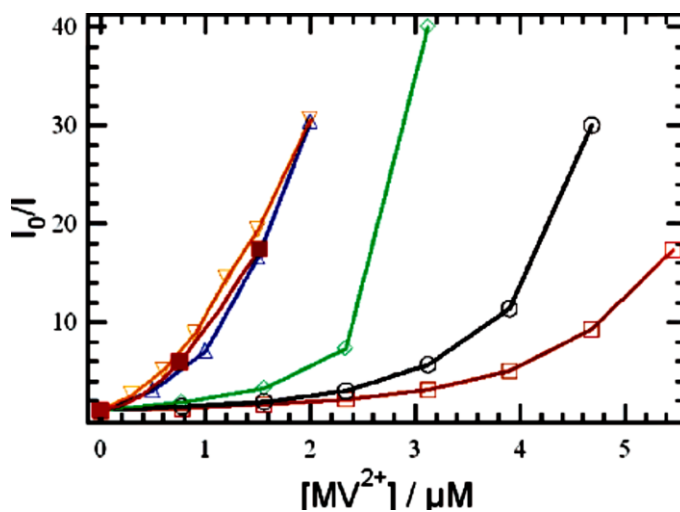


Figure 1-14. Quenching of 10 μM PPE- CO_2^- emission by MV^{2+} in water (\blacksquare) and in methanol with 0 μM (\square), 2.5 μM (\circ), 5.0 μM (\diamond), 7.5 μM (\triangle), or 10.0 μM (∇) CaCl_2 . Reprinted with permission from Jiang, H., *et al.*⁴⁷

The superlinear SV plot was also found in the aggregated polymer quenching system as reported by Schanze and coworkers in 2006.⁴⁷ It was uncovered that addition

of a certain amount of Ca^{2+} into the anionic carboxylate CPE (PPE- CO_2) in methanol could greatly enhance the quenching efficiency of MV^{2+} . The key mechanism is Ca^{2+} could induces aggregation due to its capability for effectively cross-linking PPE- CO_2 chains by complexing with the carboxyl-side groups belonging to two adjacent polymer chains. The superlinear property of SV plot was observed in the plots and it is more pronounced when more calcium ions participate (Figure 1-14).

Environmental Effect on the Conformation of CPE

From above description, it is easy to understand that the solvent has much effect on the conformation change of CPE. In 2002, Schanze and coworkers²⁴ reported that an anionic PPE (PPE- SO_3 , Figure 1-9) exists as single polymer chain in methanol, where its fluorescence properties (sharp emission peak, short lifetime, high quantum yield) are very similar to those it exhibits in good solvents (Figure 1-15). However, the quantum yield decreases substantially, accompanied by the appearance of a new broad emission band with low intensity and longer wavelength in a $\text{H}_2\text{O}/\text{MeOH}$ (1:1) solvent. In pure water, PPE- SO_3 features a broad peak in the fluorescence spectrum and a relatively low quantum yield. The longer lifetime is observed at longer wavelength. The entire change suggests that aggregation occurs in the system. The very broad band indicate the inter-chain interactions induced by the polar solvent, i.e., H_2O , which is presumably due to π -stacking between rigid polymer backbone, leading to a relatively “ordered” three dimension (3D) structure of the CPE. This statement can be supported by the red-shift and narrowing of the absorption peak as the portion of water in the mixture increases, consistent with the features appeared in the absorption spectrum when a polymer has a higher structure order and longer conjugation length.⁴⁸⁻⁵⁰

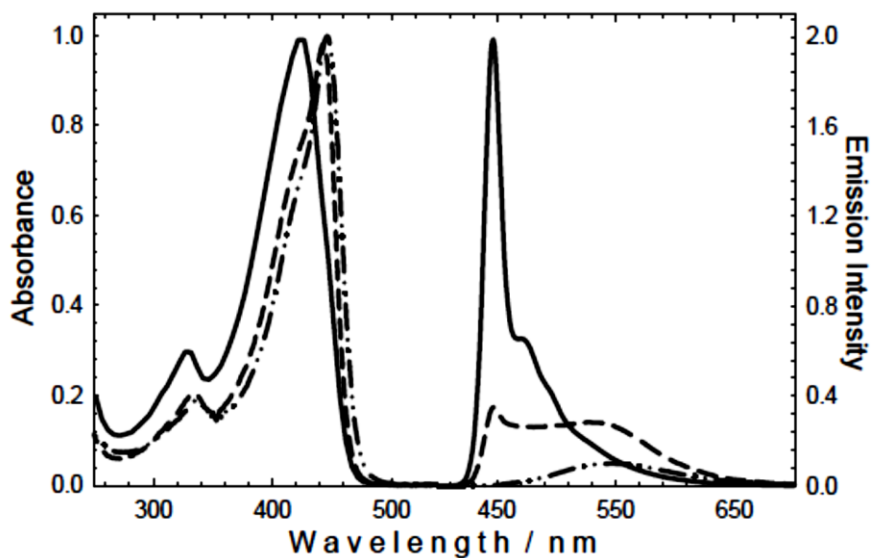


Figure 1-15. Absorption (left) and fluorescence (right) spectra of PPE-SO₃ in MeOH (—), (1:1) H₂O-MeOH (--), and H₂O (-•-). Fluorescence spectra were measured with excitation at 400 nm and normalized according to relative quantum yield. Reprinted with permission from Tan, C. Y., *et al.*²⁴

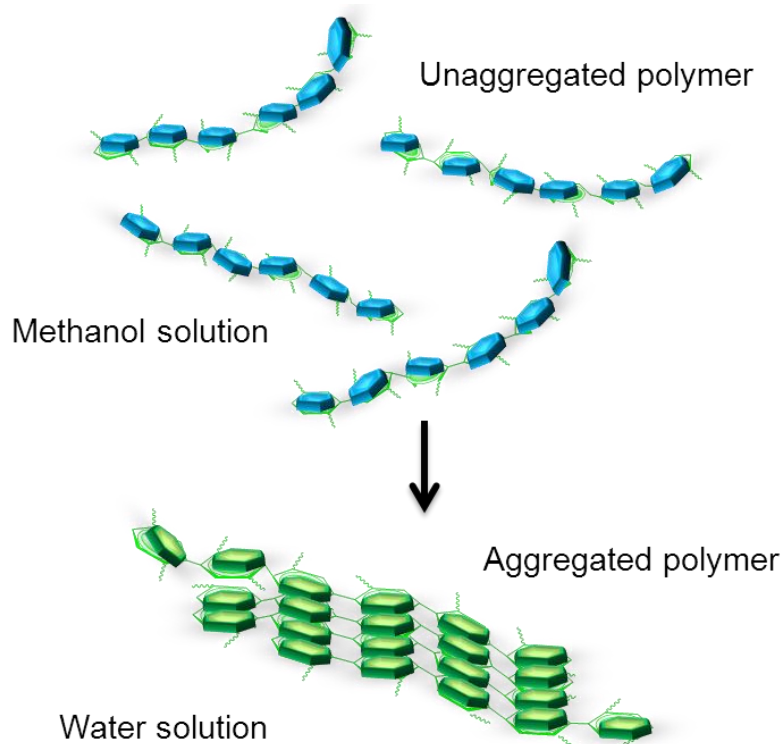


Figure 1-16. Solvent effect on the aggregation state of CPE. Adapted with permission from Tan, C. Y., *et al.*⁴⁵

In the polar solvent, the hydrophobic backbone of CPE has the tendency to stack. The ordered structure has lower surface energy, so that a well-arranged aggregation is favorable for CPE to remain soluble and stable in the water. A more optimized situation will be the polymer chains align with their long axes parallel, keeping the phenyl rings nearly co-planar (Figure 1-16). The structure is stabilized by the π - π stacking interaction and polar functional groups.

The above examples are based on the linear linked PPE. How about the solvent effect on the structure of *meta*-linked PPE? In the late 1990s, Moore and co-workers⁵¹⁻⁵³ demonstrated that *meta*-linked oligo(phenylene ethynylene)s (OPEs) that are substituted with oligo(ethyleneoxy) side chains self-assemble into a helical conformation in a poor solvent such as acetonitrile. The structure of an OPE and a simulation model created by computer explaining the transition of its conformation in different solvents are shown in Figure 1-17. This conformational transition is further studied by fluorescence and absorption spectra. The changes in the spectra for the OPE in solvent titration experiment (vary the composition of polar and non-polar solvents or vary the polarity of solvent) resemble that of quenching or aggregation process, which features excimer-like band in fluorescence emission (Figure 1-18). The observed phenomena are expected to arise from the backbone's intra-molecular π - π stacking interaction as shown in the bottom cartoon of Figure 1-18. Moore and co-workers also demonstrated that formation of the helical conformation is a cooperative effect, requiring a minimum number of 10 repeat units (one phenylene and one ethynylene unit) in the OPE chain before the process becomes thermodynamically favored.⁵¹

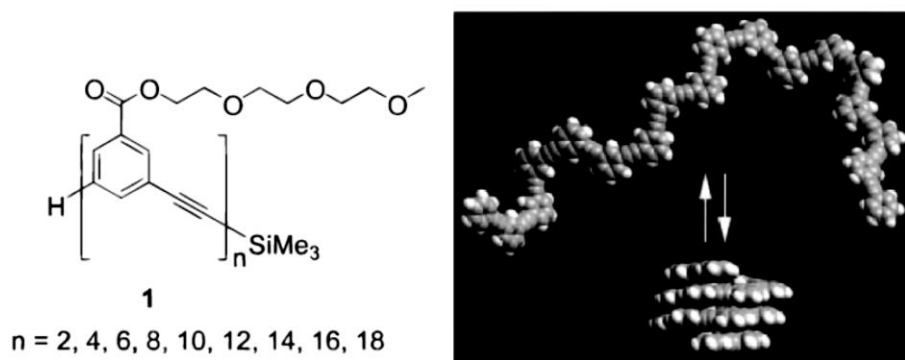


Figure 1-17. Structures of OPEs studied by Moore's group and a space-filling model showing the conformational equilibrium for OPE of length $n = 18$. Side chains are not shown for clarity. Reprinted with permission from Prince, R. B., *et al.*⁵¹

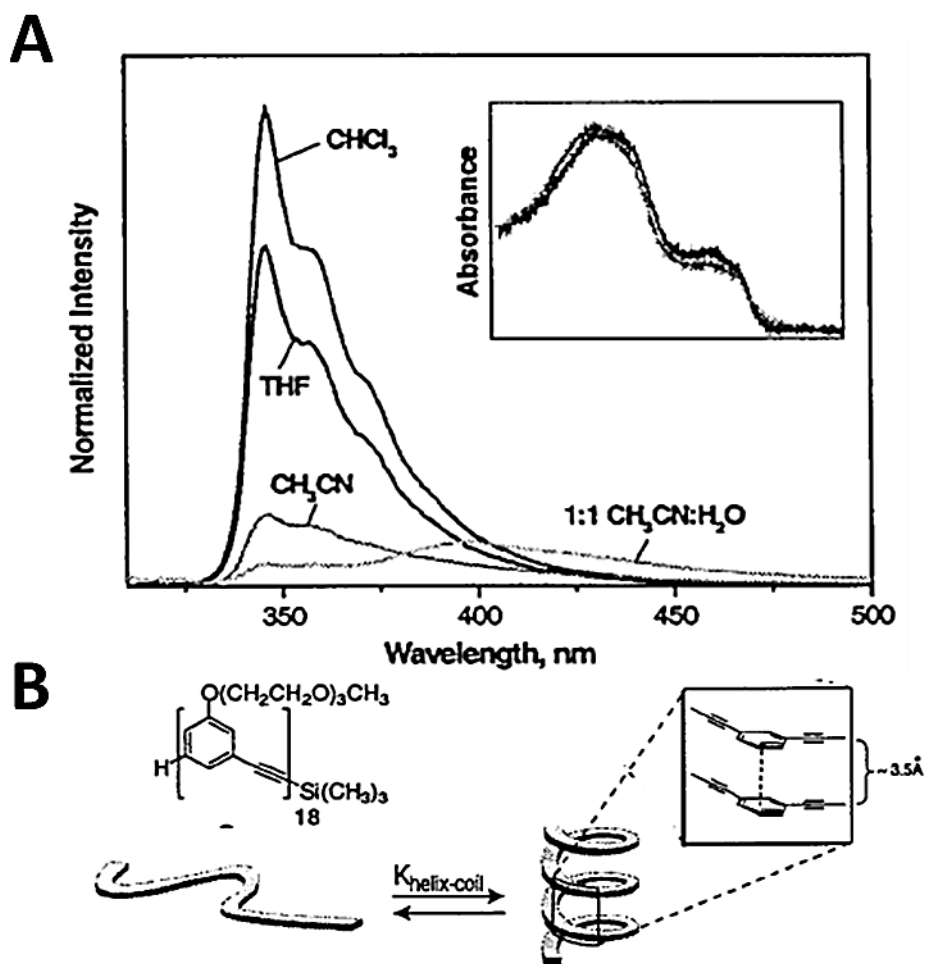


Figure 1-18. A) Normalized emission spectra of OPE in various solvents. Insert: absorption spectra. B) Structure of OPE and cartoon for coil-helix transition process. Reprinted with permission from Lahiri, S., *et al.*⁵³

Other than solvent type, the pH of solution also affects the conformation of CPEs. Schanze and coworkers²⁶ have investigated the photophysical changes of an anionic phosphonate-substituted PPE (PPE-PO₃, Figure 1-9) in the solution with various pH. As the pH decreased from 12.0 to 7.5, the absorption spectrum undergoes a red shift by 35 nm. At pH 11.0, the fluorescence spectrum has a maximum peak at 447 nm, which becomes very broad and red-shifts to 518 nm at pH 7.5. The quantum yield also decreases from 0.05 to 0.03. All the phenomena indicate that the CPE undergoes aggregation due to the decrease in pH which would result in partial protonation of the phosphate side chains. This process consequently reduces the overall negative charge density on the polymer backbone and diminishes the repulsion between different chains that hinders polymer-polymer association.

Sensing Assay Development of CPEs

In the past decade, CPEs have been developed as sensitive fluorescence-based sensors^{16, 54} for metal ions,^{55, 56} small molecules,⁵⁷ and biomacromolecules (proteins,^{43, 58} enzymes,⁵⁹⁻⁶² DNA⁶³⁻⁶⁶). The high sensitivity of this type of sensor benefits from the intrinsic fluorescence signal amplification that results from the electronic delocalization and inter- or intra- chain exciton migration. In general, there are several mechanisms for CPE-based sensing, including photoinduced electron transfer (charge transfer mechanism), energy transfer (FRET), and conformational change.

Small Ions/Molecules Sensing

For environmental and biological interests, small molecules like heavy metal ions, small organic molecules which are usually toxic hazards or dangerous, require highly sensitive and real-time detection. The following section will provide detailed examples for metal ions and small molecules sensing by CPEs.

Metal ion sensing

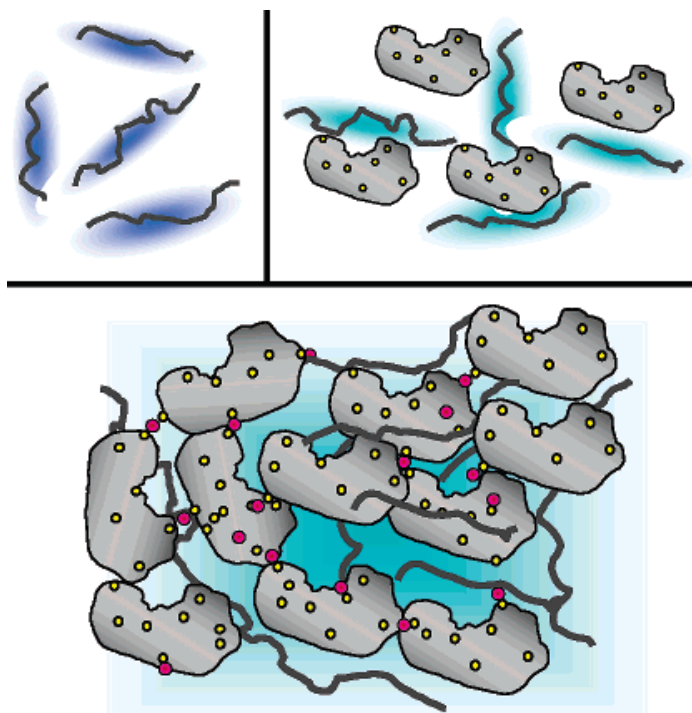


Figure 1-19. Schematic illustration of Hg²⁺-induced agglutination of the h-PPE-CO₂/papain complex. Reprinted with permission from Kim, I. B., *et al.*⁶⁷

From the above discussion, we can see that electron-deficient ions can act as an efficient quencher due to the electron-transfer quenching process. Meanwhile, many metal cations, especially multivalent ions are capable of crosslinking adjacent CPE chains by chelation or multi-binding interaction, which spontaneously induces aggregation and alters the photophysical properties of a CPE. Based on this strategy, many CPE based metal ions sensors have been successfully designed and developed. For example, in 2005, Bunz and coworkers designed a highly sensitive and selective sensor for lead ions in water by making use of the multivalent interactions between the carboxylate group on the CPE with the target ion. The presence of Pb²⁺ is signal by the amplified quenching of a homo carboxylate-substituted poly(phenylene ethynylene) (h-

PPE-CO₂, Figure 1-9), which is dissolved as single polymer chains in aqueous solution due to the high negative charge density on the side chains. A set of different divalent metal ions including Ca²⁺, Zn²⁺, Hg²⁺, Mg²⁺, Pb²⁺, Cu²⁺ and Mn²⁺ were tested individually on the polymer in pH 7.2 buffer system. Pb²⁺ has the overwhelming K_{SV} values $\sim 8.8 \times 10^5 \text{ M}^{-1}$ with at least 10 fold higher sensitivity than other ions. This high quenching efficiency is attributed to the electron transport properties of the CPE and the simultaneous bonding between the cation and carboxylates on polymer chains. Then, the same CPE was applied in another sensing project for mercury ion by the same research group. In this sensing strategy, a positively charged protein papain, known to bind to Hg²⁺ through sulfhydryl groups,⁶⁷ is added into the polymer solution and form an electrostatic complex with h-PPE-CO₂ (Figure 1-19). Only in the presence of Hg²⁺, the complexes are more prone to agglutinate and even precipitate at high [Hg²⁺], resulting in weak or no emission for h-PPE-CO₂.

The biomolecule mediated strategy was also employed in the development of a potassium ion sensor. In 2004, Leclerc and coworkers⁶⁸ demonstrated that a CPE/DNA-based aptamer complex has superior sensitivity towards K⁺ in aqueous solution. They synthesized a cationic CPE, a polythiophene (PT), which is able to couple with anionic DNA to form a more planar, potentially aggregated complex. The aptamer was intentionally selected so that it can form a quadruplex in the presence of K⁺. After addition of CPE to the aptamer/K⁺ system, the polythiophene displayed a conformation wrapping over the adduct formed by quadruplex aptamer and K⁺ (Figure 1-20A). The absorption peak locates in between that of free and aptamer-coupled CPE in the spectra (Figure 1-20B). The chromatic change corresponding to the conformational

change on CPE can be observed directly by eye. This smart strategy has been further applied by Wang and coworkers⁶⁹ in a new ssDNA mediated K^+ sensor by introducing in the FRET mechanism, which has been reported in 2005.

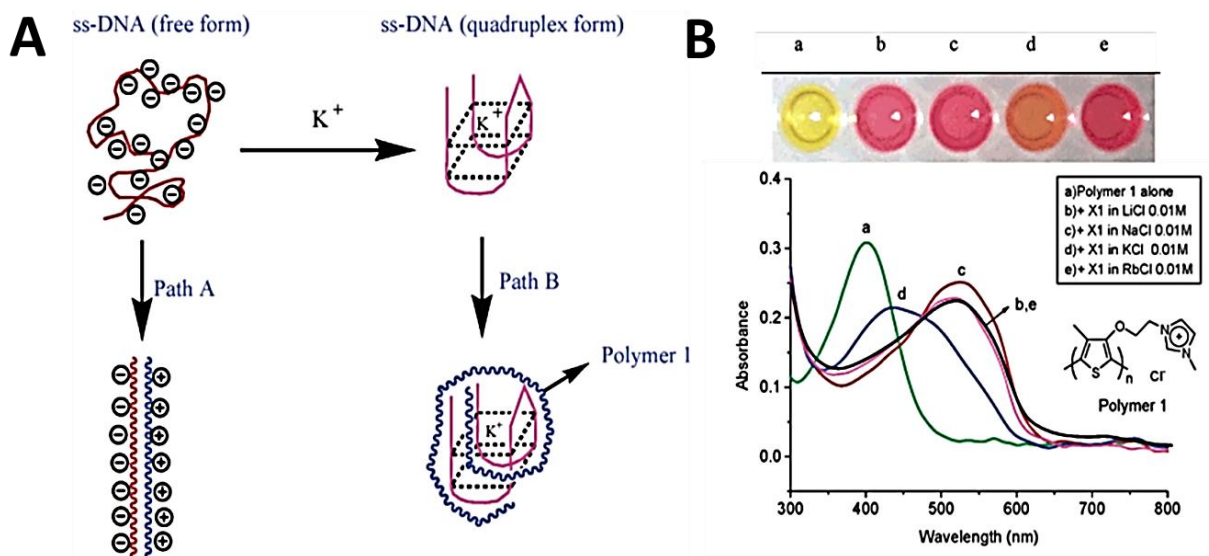


Figure 1-20. A) Sensing strategy for aptamer mediated CPE based K^+ sensor. B) Absorption spectra and visible colors of polythiophene mixed with different ions. Reprinted with permission from Ho, H. A., *et al.*⁶⁸

Small molecule sensing

Besides metal ions, many CPE based sensors have been designed for other small molecules, especially biomolecules. Water solubility of CPEs makes them applicable in the biological system. In 2002, Schanze and coworkers⁷⁰ developed a sugar sensor by making use of the high quenching ability ($K_{SV} = 2.8 \times 10^7 \text{ M}^{-1}$) of a boronic acid functionalized benzyl viologen, $p\text{-BV}^{2+}$, on an anionic CPE PPE-SO₃ (Figure 1-9). Upon the addition of sugar molecules, the strong association between $p\text{-BV}^{2+}$ and PPE-SO₃ is hindered since the sugar molecules can react with the viologen to produce a charge neutral bisboronate derivative that barely has quenching ability on the CPE (Figure 1-21A). A remarkable fluorescence recovery is observed for CPE. Particularly, a 50-fold

increase in intensity is detected for the CPE upon the addition of 10 mM D-fructose, which is significantly higher than that of D-galactose and D-glucose (Figure 1-21B). This “turn-on” sensing strategy was further applied in the PPI sensor developed by Schanze and co-workers.⁷¹ The metal ion Cu^{2+} is coupled with the PPE- CO_2 (Figure 1-9) to form a quenched system at the beginning. Upon the addition of PPI, a more stable PPI/ Cu^{2+} complex is created, which sequesters the Cu^{2+} from the CPE, turning on the fluorescence of polymer.

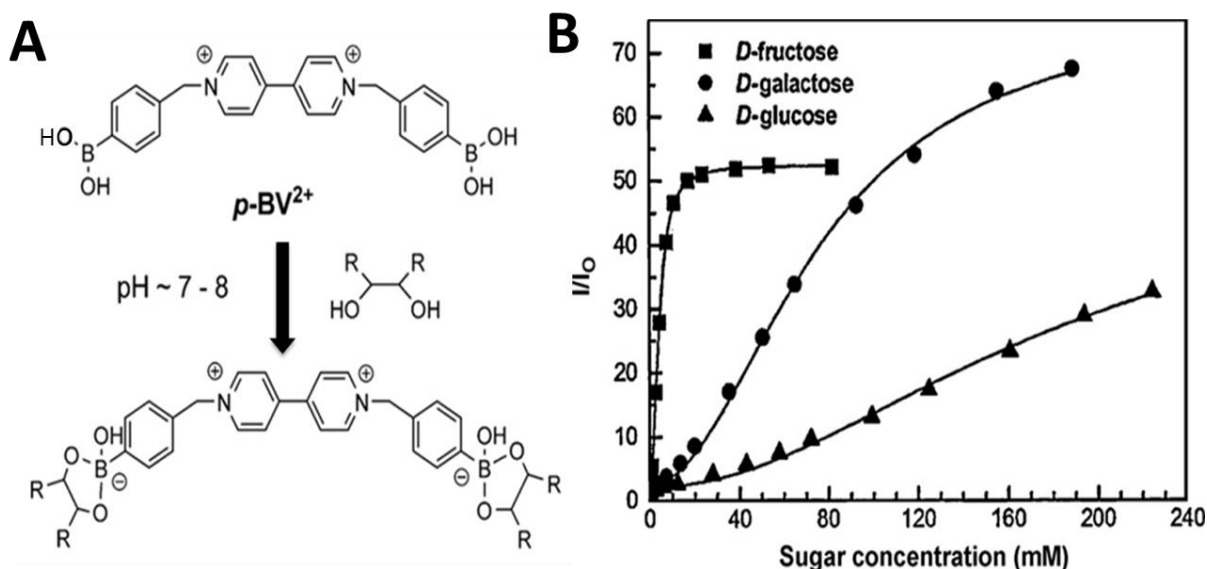


Figure 1-21. A) Interaction between $p\text{-BV}^{2+}$ and sugar. B) Fluorescence recovery titration curves against three sugars. Reprinted with permission from DiCesare, N., *et al.*⁷⁰

In addition to the examples described above, there are many other types of sensors developed for small molecules, including adenosine triphosphate (ATP),⁷² hydrogen peroxide (H_2O_2),⁷³ antioxidants,⁷⁴ $\text{Fe}(\text{CN})_6^{4-}$,⁴⁴ and $\text{Ru}(\text{phen})_3^{4+}$ ((phen)=4,7-bis(4-sulfophenyl)-1,10-phenanthroline).⁴⁴

DNA Sensing

Deoxyribonucleic acids (DNAs) play essential roles in genetic and epigenetic researches. As a special information carrier with stable and well-ordered macromolecular structure, DNA is recognized as a key target for the diagnosis of cancer and disease as well as the detection of bacteria and virus. To develop *in vitro* DNA sensors or probes, the general way for recognition of target DNA sequence lies on hybridization between DNA sequences, which is signaled typically through electrical, magnetic, or optical responses.

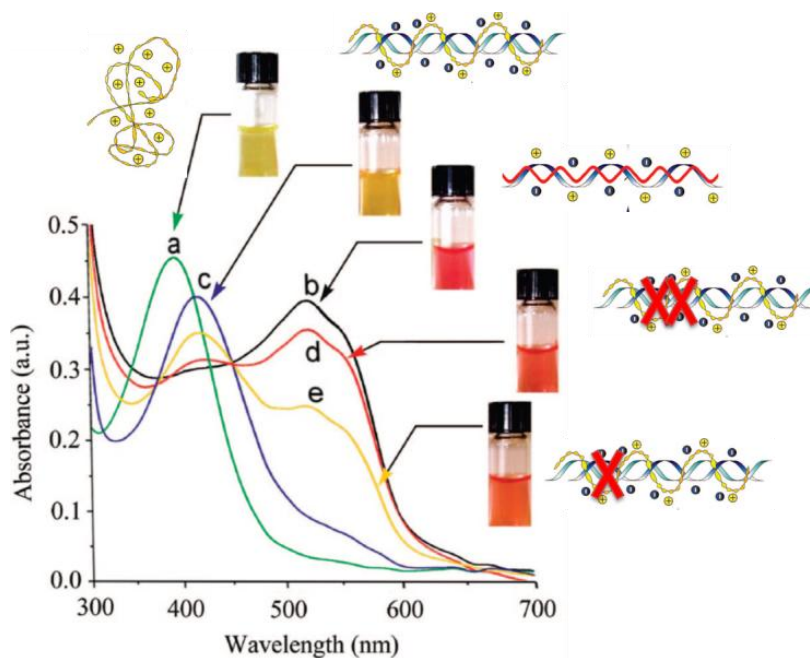


Figure 1-22. Photographs, possible structure and UV-Vis absorption spectra changes for the PT based DNA sensor: a) PT alone, b) PT/ssDNA duplex, c) PT/dsDNA triplex, d) PT/ssDNA plus a complementary target with a two-base mismatch, and e) PT/ssDNA plus a complementary target with a one-base mismatch after five minutes. Reprinted with permission from Ho, H. A., *et al.*⁷⁵

CPE based DNA probe, particularly, when it is labeled on the DNA or “heterohybridized” with a DNA sequence has been well developed in the past decade. Among the research groups working toward CPE-based DNA sensing, Leclerc group is

the pioneer who initially developed ultrasensitive polythiophene (PT)-based DNA sensors that achieve a zmol sensitivity.⁷⁵ Driven by electrostatic attraction, the cationic PT undergoes a conformational transition from a random coil to a twisted planar conformation complexing with single strand DNA (ssDNA), forming a so-called “duplex”. The 143 nm red shift in absorption spectrum affords the CPE colorimetric sensing ability: the yellow-red transition can be directly distinguished by naked eye. Interestingly, if the complementary target ssDNA is further added into the duplex system at high temperature, the color of sample turns back to yellow and a blue shift of the absorption peak is observed after 5-minute incubation. This change is attributed to the formation of “triplex” between PT and dsDNA and the loose structure of PT is more like the random coil. When two-base mismatch or one-base mismatch complementary ssDNA is added to the duplex solution, a color of orange, in between red and yellow, is observed, which corresponds to the intermediate state of tight and loose binding for the complex due to incomplete hybridization. All those changes are quantitatively detectable through the absorption spectra as shown in Figure 1-22.

They further incorporated the FRET mechanism in the design by conjugating the dye molecule onto the end of probe ssDNA.⁷⁵ Distinction between the triplex and duplex can be achieved by comparing the FRET efficiency under two circumstances: more emission of the dye molecule can be observed for triplex which is possibly due to the higher quantum yield of PT in non-aggregated state. Non-complementary or mismatched ssDNA is also distinguishable and this turn-on sensor has a detection limit as low as 3 zM toward target ssDNA. The strategy that combines PF with FRET also inspired Bazan and Wang. They have successively reported a number of applications

such as detection of DNA mismatch, single nucleotide polymorphism (SNP), DNA methylation, gene regulation, etc.^{76,77} Moreover, Bazan and co-workers⁷⁸ improved the method to a two-step energy transfer by introducing in ethidium bromide (EB), which can intercalate into the helix dsDNA and become emissive. Thus the dye molecule on the probe ssDNA acts as a convertor for energy dipole moments, bridging the polymer and EB. Hence, the non-specific interaction between non-complementary or mismatched DNA and duplex probe will not cause interference.

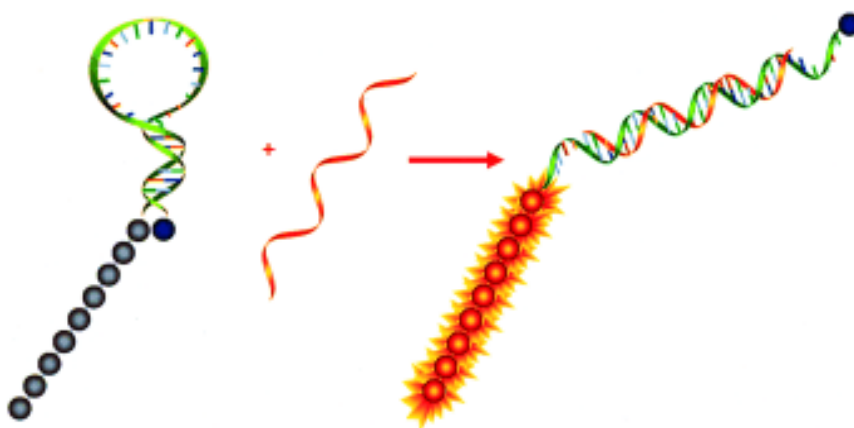


Figure 1-23. Schematic illustration of DNA detection by CPE labeled molecular beacon. Reprinted with permission from Yang, C. Y. J., *et al.*⁷⁹

A covalent conjugate between a molecular beacon (MB) and CPE was first reported by Tan and Schanze.⁷⁹ As illustrated in Figure 1-23, this sensing strategy employs a sulfonated PPE as fluorescent probe and Dabcyl (Dabcyl = 4-(4-(dimethylamino) phenylazo) benzoic acid) as quencher. It has a rapid response (at second time scale) to the presence of target DNA, which simultaneously stretches the hairpin-like DNA strand and disrupts the quenching process, in the regular hybridization buffer solution. The advantage of this sensor lies in its resistance to both ionic strength and surfactant effect, by increasing which, the nonspecific interactions, such as electrostatic and hydrophobic interactions between the target DNA and CPE chain, are

effectively diminished. The molecular beacon device was further developed by Kim's group.⁸⁰ The anionic CPE structure was optimized by introducing pendant polyethynylene glycol (PEG) groups to avoid aggregation of the CPE under higher ionic strength conditions and increase the quantum yields in aqueous solution. Dabcyl-labeled DNA sequences were conjugated to both ends of the CPE to generate a device with a stoichiometric ratio of [Dabcyl]:[CPE] as 2:1. This method also shows its capability of distinguishing single-base mismatched DNA from target DNA at the same concentration.

Protein/Enzyme Activity Sensing

Proteins are essentially involved in almost every process within cells and the constitution of organisms. A large number of proteins are various types of enzymes that catalyze tens of thousands of reactions that are vital to maintaining life. Some proteins also are important components in muscle, blood, skin, cartilage, and bones. Others participate in cell signaling, molecular recognition, cellular communication, and gene expression.⁸¹ Therefore, identification or recognition of proteins is highly important to medical diagnostics or clinical research.⁸²⁻⁸⁵ A great number of methods or strategies have been developed in the past decades including electrochemistry,⁸⁶ Raman,⁸⁷ flow cytometry,⁸⁸ fluorescence immunoassay,⁸⁹ and mass spectrometry.⁹⁰ However, the requirement for sophisticated instrumentation and proficient manipulation limits their broader application. The method combining sensitivity, simplicity and economy is still highly demanded.

CPE based protein sensing methods have drawn much attention throughout the past years.^{16, 54, 91-94} The following discussion will be divided to two sensing categories:

protein and enzyme sensing. Each category has models representing the different mechanisms of energy transfer, electron transfer and conformation change.

Protein sensing by CPE based sensor

The “quencher-tether-ligand” (QTL) model is among the earliest CPE-based protein sensing assays by making use of the electron transfer superquenching property of CPEs.^{43, 54} It was well discussed in the previous section that MV^{2+} is a remarkably efficient CPE quencher. A biotin- MV^{2+} , which has a flexible tether in between biotin and MV^{2+} (Figure 1-24), was used in the sensing strategy as shown in Figure 1-25. This ligand-quencher conjugate displays net positive charge and forms the complex with anionic MPS-PPV (structure shown in Figure 1-8) via electrostatic attraction, quenching the fluorescence of MPS-PPV with similar quenching efficiency as that of non-labeled MV^{2+} . Avidin, which has four biotin binding sites with extremely high binding affinity (K_b , $\sim 10^{15}$ M),⁹⁵ is added into the MPS-PPV/biotin- MV^{2+} system. The stronger interaction between biotin and avidin allows the formation of a more stable complex, causing the former CPE/quencher complex to disassociate. A significant increase of the polymer’s fluorescence is observed, even at low concentration of avidin (100 nM). This strategy paved a new way for development of CPE-based protein sensing methods by using the QTL model. The dequenching or “turn-on” based sensing strategy has been further extended in other sensors by many researchers.⁶⁰⁻⁶²

Besides the QTL based sensing model, another sensing strategy that utilizes the direct quenching property of some special proteins has emerged.^{58, 68, 96, 97} Usually, those proteins have an electron deficient center, such as heme moiety, which acts as an electron acceptor center like metal ions. Although the direct sensing methods lack the

exclusive specificity as antigen-antibody type, they are much simpler and labor-saving by averting the need for additional ligand design or modification.

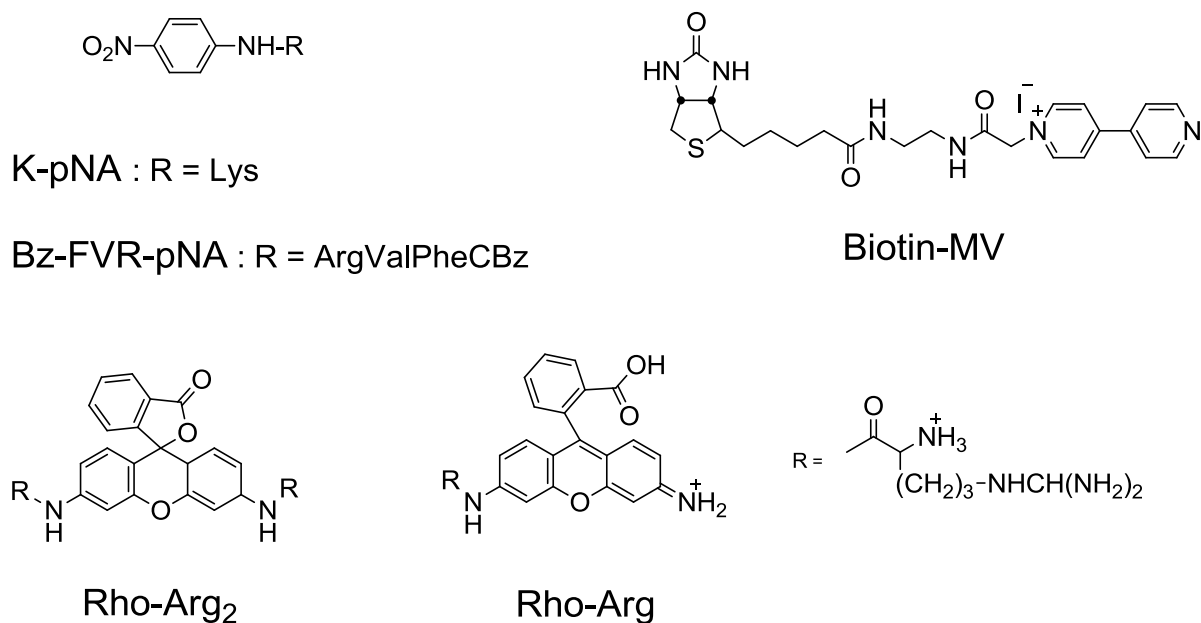


Figure 1-24. Chemical structures of quenchers or ligands.

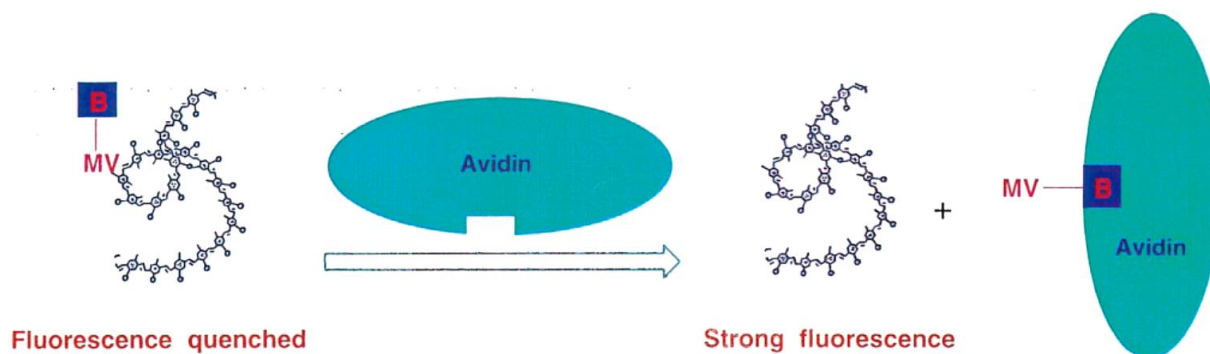


Figure 1-25. Whitten's quencher-tether-ligand based "turn-on" strategy for avidin sensing. Reprinted with permission from Chen, L. H., *et al.*⁴³

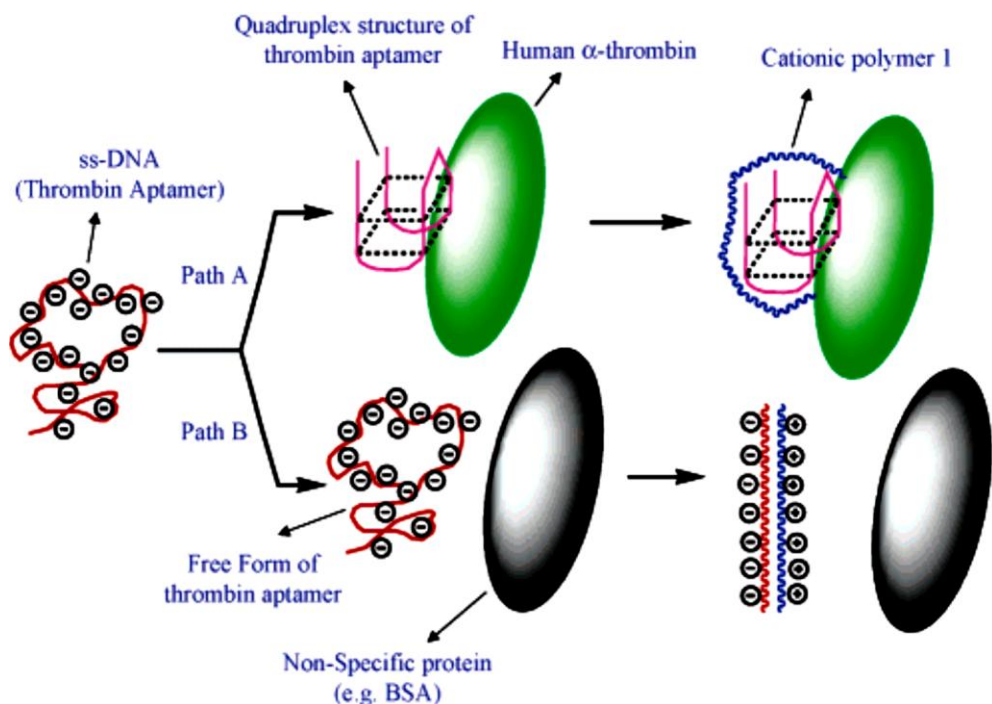


Figure 1-26. Schematic description of the specific detection of human α -thrombin by use of ssDNA thrombin aptamer and cationic polymer. Reprinted with permission from Ho, H. A., *et al.*⁶⁸

Analogous to the sensing strategy for K^+ discussed in the previous section, a sensing method for the human α -thrombin utilizing the same polythiophene and ssDNA thrombin aptamer was developed by Ho and Leclerc in the same report.⁶⁸ As shown in the Figure 1-26 Path A, the thrombin aptamer forms a quadruplex structure upon binding to the human α -thrombin. The electrostatic attraction between the cationic polythiophene and anionic DNA forces the polymer to wrap over the quadruplex, altering the conformation of polymer. De-aggregation of the polymer can be easily monitored through its photophysical properties change—a blue shift in absorption spectrum and an emission intensity increase in fluorescence spectrum. The high selectivity is demonstrated with no signal detectable when non-specific protein or

ssDNA is added. The same strategy has been applied to detect the protein calmodulin (CaM) later by Nilsson and coworkers.⁹⁸

Enzyme activity sensing

One of the most commonly used sensing strategies for enzymes incorporates the well-defined QTL model into the sensing scheme. By coupling an enzyme substrate with the quencher and mixing with CPEs, the presence of a target enzyme can be signaled by fluorescence quenching (turn-off) or dequenching (turn-on) modes.⁶⁰⁻⁶²

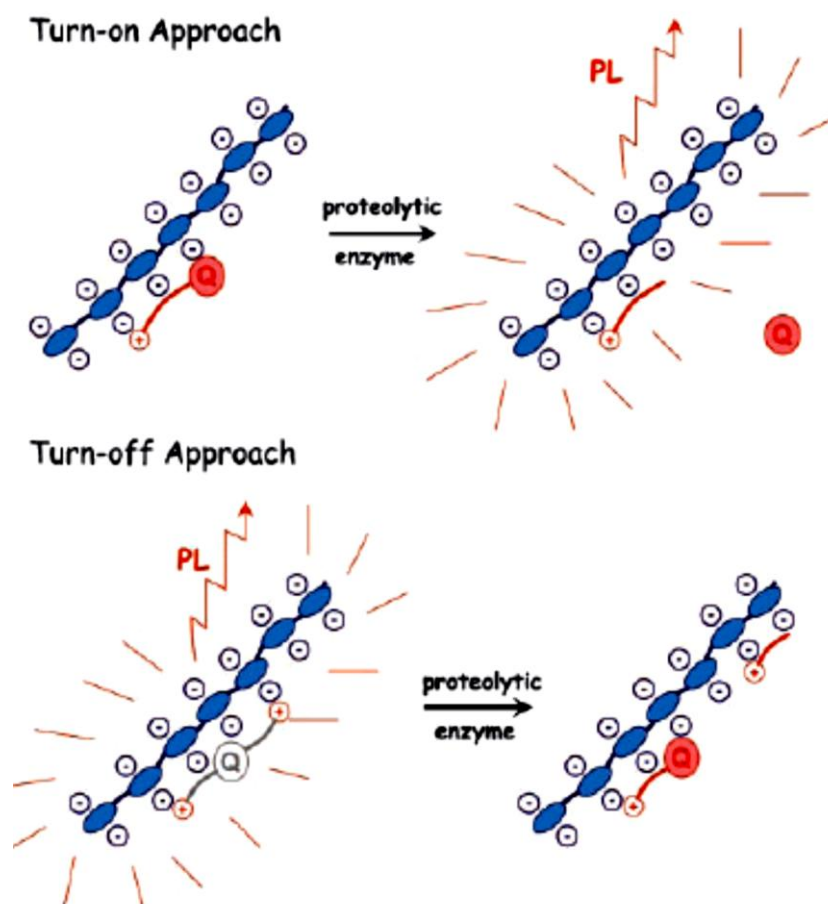


Figure 1-27. Mechanism of the “turn-on” and “turn-off” CPE-based sensors. Reprinted with permission from Pinto, M. R., *et al.*⁶¹

In 2004, Schanze and co-workers established two typical “turn-on” and “turn-off” approaches to detect protease activity.⁶¹ Commercial available fluorescence quencher-

tether-substrates were used in two strategies. Two *p*-nitroanilide (*p*-NA) labeled peptide, L-Lys-*p*-nitroanilide dihydrobromide (K-*p*NA, Figure 1-24) and N-benzoyl-Phe-Val-Arg-*p*-nitroanilide hydrochloride hydrate (Bz-FVR-*p*NA, Figure 1-24), are the substrates of two enzyme peptidase and thrombin, respectively. In the “turn-on” approach (Figure 1-27 upper), since the two *p*-NA labeled substrates display net positive charge, they ion-pair with the anionic sulfonated PPE (PPE-SO₃, Figure 1-9). The *p*-NA moiety strongly quenches the fluorescence of the polymer even at nanomolar concentration through the amplified quenching mechanism. The addition of peptidase or thrombin to the system causes peptide hydrolyzed, cleaving the *p*-NA apart from the peptide, and leaving the *p*-NA with no charge. The fluorescence of the polymer is recovered due to the lack of association between the neutral quencher and polymer.

The “turn-off” approach (Figure 1-24), comprises another anionic CPE, PPE-CO₂, (Figure 1-9) with a non-emissive peptide-derivative rhodamine substrate (Rho-Arg₂, Figure 1-24). The mixture is first excited at 400 nm and emits strongly around 470 nm. The introduction of proteolytic enzyme papain, which catalyzes the hydrolysis reaction of the peptide, separates the rhodamine and peptide segments, restoring the emissive property of rhodamine. The decreasing of the fluorescence of the polymer as well as the appearance of a second fluorescence peak at 515 nm is attributed to the singlet–singlet energy transfer from PPE-CO₂ to Rho-Arg (Figure 1-24), which has an emission peak around 515nm, giving rise to a “turn-off” sensing strategy for papain (Figure 1-27 bottom). The detection limit for this enzyme is evidenced to be 3.5 nM. This strategy successfully introduced in the fluorescence resonance energy transfer (FRET), paving another way for enzyme sensing. In addition, several groups have developed a new

FRET-based enzyme sensing strategy by just simply substituting the quencher discussed in the “turn-on” strategy with a fluorophore as an energy acceptor.⁹⁹⁻¹⁰¹ In sum, these two sensing strategies establish a novel platform for sensitive detection of enzymes, motivating the development of a variety of similar CPE based enzyme-cleavage involved sensing methods.^{60, 62, 102, 103}

Another attractive strategy appearing recently is natural enzyme substrates based model.^{102, 104, 105} Instead of sophisticated designing or labeling a substrate, it applied the naturally existing substrate directly into sensing assay. By utilizing the interaction between the substrate and a common quencher or CPE itself, the photophysical properties of CPEs can be altered significantly, displaying either “turn-on” or “turn-off” response.

Very recently, Liu and co-worker reported a “turn-on” assay by using the natural substrate Cytochrome *c* (Cyt *c*), in conjunction with an anionic poly(fluorene-co-phenylene) (PFP-CO₂), to detect protein trypsin activity.¹⁰² Naturally cationic Cyt *c* is an electron-deficient heme-containing protein, holding superquenching property. Thus it can be regarded as a natural quencher-ligand and utilized in the “turn-on” mode following the first path in Figure 1-27. The enzyme trypsin was reported to digest Cyt *c* (isoelectric point, *pI* = 10.5) into more than 15 fragments,¹⁰⁶ among which the metal-containing heme peptide fragment, responsible for the quenching effect in Cyt *c*, has a reduced *pI* = 7.1 (based on an online peptide *pI* calculator¹⁰⁷). In the pH 8.9 buffer system, the positively charged Cyt *c* can form a complex simultaneously with anionic PFP-CO₂, efficiently quenching the fluorescence with $K_{SV} = 1.32 \times 10^7 \text{ M}^{-1}$. After the addition of trypsin, the Cyt *c* is broken down, producing the metal-containing heme

peptide fragment with negative charges. The complexation of the quencher and CPE is subsequently disturbed, resulting in the fluorescence recovery for PFP-CO₂, which can be easily observed by eye.

The sensitivity for this sensor is found to be 1.7 nM. The selectivity of this assay was demonstrated by detecting three other enzymes, lysozyme, alkaline phosphatase (ALP), and thrombin, under the same condition and no recovery response is observed for all of them. By taking advantages of natural superquenching property of Cyt c, complicated design for the substrate is not needed and the procedure becomes simpler. Meanwhile, the interference and uncertainty brought into the catalytic reaction by the substrate modification are eliminated.

Conformation change based strategy also attracts much attention due to its non-invasiveness without need for covalent labeling or molecule modification. In 2009, Schanze and co-workers reported a fluorescence turn-off assay for phospholipase C (PLC) by making use of the reversible aggregation process of anionic CPE (BpPPESO₃, Figure 1-28A).¹⁰³ The BpPPESO₃ aggregates in the aqueous solution, featuring with a broad, structureless band in the emission spectrum. The addition of the natural substrate of PLC, phosphatidylcholine (10CPC), causes the increase in CPE fluorescence intensity. The zwitterion phospholipid 10CPC has the surfactant property that helps de-aggregate the polymers by forming lipid-polymer complex. However, as enzyme PLC presents, 10CPC is degraded to phosphorylcholine and a long chain (DAG) without charge. As the product molecules lose the surfactant function, the polymers are not able to maintain non-aggregation state and their fluorescence intensity turns off subsequently (Figure 1-28B).

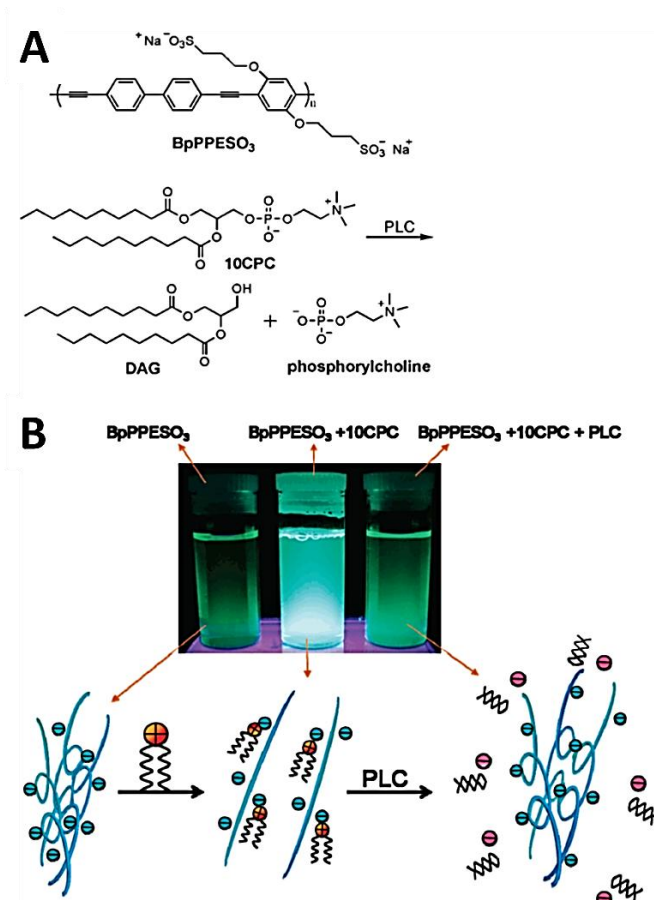


Figure 1-28. A) Structures of polymer, BpPPESO₃ and substrate, 10CPC, and reaction scheme for hydrolysis of 10CPC by PLC. B) Mechanism of PLC turn-off assay. Reprinted with permission from Liu, Y., *et al.*¹⁰³

In the previous section, copper ion has been proved to be an excellent quencher for anionic CPE. Consequently, in many reports, Cu²⁺ has particularly involved in the indirect sensing assay for enzymes activity.^{71, 104, 105, 108} In those methods, substrates or reaction products, such as PPI and amino acid, are capable of capturing or complexing with Cu²⁺, keeping the Cu²⁺ away from the fluorescent CPE and making the signal turn over. For example, in 2008, a “turn-off” sensing strategy for alkaline phosphatase (ALP) was reported by Schanze and coworker.⁷¹ The addition of PPI to the pre-quenching system of PPE-CO₂ (Figure 1-9) with Cu²⁺ readily induced fluorescence recovery. Then as the ALP is added into the system of PPE-CO₂/Cu²⁺/PPI, the hydrolysis process of

PPI is triggered, concomitant with the releasing of Cu^{2+} back to the PPE from the PPI- Cu^{2+} complex. This process is signaled by the decrease of the polymer's fluorescence intensity (Figure 1-29). The same idea has been applied in another sensing method for adenylate kinase activity by employing ATP, ADP, and AMP as substrates, which was also reported in 2009.⁹³

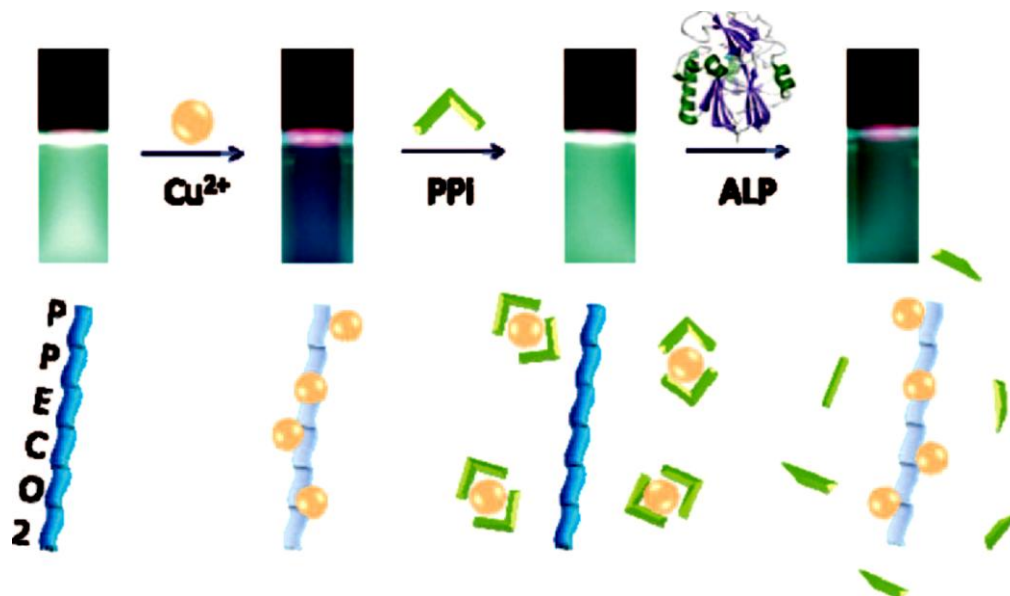


Figure 1-29. Mechanism of ALP turn-off assay and photographs of solutions illuminated with near-UV light illustrating the polymer fluorescence under the different conditions of the assay. Reprinted with permission from Liu, Y., *et al.*⁷¹

Non-specific Interaction of CPEs

CPE-based protein sensing methods have many advantages including sensitivity, simplicity and economy. However, it has its own shortcomings. One of the challenges is that too much reliance on the electrostatic or hydrophobic interactions may bring in uncertainty and unwanted non-specific interaction between non-target species with probe, causing false signals. There are a number of reports regarding non-specific effects published and reviewed.^{33, 109-111} Some solutions have been proposed such as pre-formed CPE-containing charge-neutral complex (CNC) by mixing cationic CPE and

anionic polymer in 1:1 ratio to obtain neutrality. At the expense of sensitivity, this type of sensor can be readily quenched by both cationic and anionic target analytes, eliminating the non-specific effects.¹⁰⁹ Other solutions for solving non-specific interaction including employing CPE coated microspheres^{60, 62} or grafted colloids¹¹² instead of CPE itself as the sensing probe, so that the aggregation state change will be less influenced by interfering species in the solution.

While non-specific interaction may be considered as a negative factor in sensor design, it also can be employed to develop new sensors. As aforementioned, the electrostatic or hydrophobic interaction between CPEs and biomolecules, such as DNAs and proteins, can induce conformation change of CPEs. The strategy has already shown the power in a variety of applications for metals, proteins and DNA sensors development as reported.^{33, 34, 68, 75} This strategy is much attractive because it is laborless, economic, and simple without sophisticated design on probe. Although one CPE may lack the specific detection of an analyte by non-specific interaction, an assembly of more than one polymer has the ability to provide informative and sufficient signal response for analyte recognition. More details and information will be displayed in the next topic-sensor array.

Sensor Array

In recent years, as increasingly demanded by genetic analysis, clinical diagnosis, environmental analysis, and homeland defense, the sensor that is able to distinguish or recognize more than one target analyte attracts much attention. The traditional specific recognition through lock-and-key mode requires sophisticated sensor/probe design and sufficient chemical/biological knowledge. Moreover, its high specificity, i.e., only one or one type of analyte can be detected at one time, hinders its universalization. An

alternative approach that emphasizes differential receptor-analyte binding interactions has emerged in the past two decades.¹¹³⁻¹¹⁶ The basic concept is chemical nose/tongue, which is derived from “electronic noses/tongues” that has the capability of producing human senses by mimicking working principle of nose or tongue. The probe elements in the sensor arrays are analogous to specialized sensory cells in the nose or mouth and the created pattern recognition systems are like the recognition portion in human’s brain for differentiating odors and flavors. Specifically, the response generated by the sensor array should be discernibly different for different analytes, exhibiting fingerprint characteristics. To conduct a detection by the sensor array, three basic stages are involved. Firstly, data/signals need to be collected from a relatively large pool of qualified samples with known category/type so as to build a database of reference. Secondly, a differential tool/method needs to be set up and trained so that the above samples can be assigned to their own group with relatively high accuracy. Finally, the technology can recognize new samples with little category information by comparing their signal fingerprint to those stored in the database. Thus qualitative or quantitative analysis can be performed. This type of sensor has been proved to be highly useful for a wide variety of chemicals sensing, e.g., metal ions,¹¹⁷ volatile agents,¹¹⁸ aromatic amines,¹¹⁹ amino acids,¹²⁰ carbohydrates,¹²¹ and proteins,¹²² which are quite important in quality control, production process/development, crime prevention and security, human health and environmental monitoring.

Several array based biological sensors have been developed by taking advantage of the optical perturbations of conjugated polymers driven by analyte-induced quenching or aggregation.^{97, 110, 123, 124} For instance, Bunz and Rotello¹²⁴ developed a cell sensing

strategy using the fluorescence signal change from a group of CPEs. As shown in Figure 1-30, those polymers with various pendant charged residues display distinct responses, i.e., the ratios of final and initial fluorescence of the CPEs, when mixed with different types of cells individually. A chemometrics technique, called linear discriminant analysis (LDA), is applied to process the resulting data matrix. A canonical pattern is created and each sample is well classified. This array-based sensing system is demonstrated can differentiate between cell types as well as discern cancerous from noncancerous mammalian cells. The robustness of the sensor array was further tested using unknown samples. An accuracy of 80% for identify three types of cells is obtained by using only four CPEs as the probes.

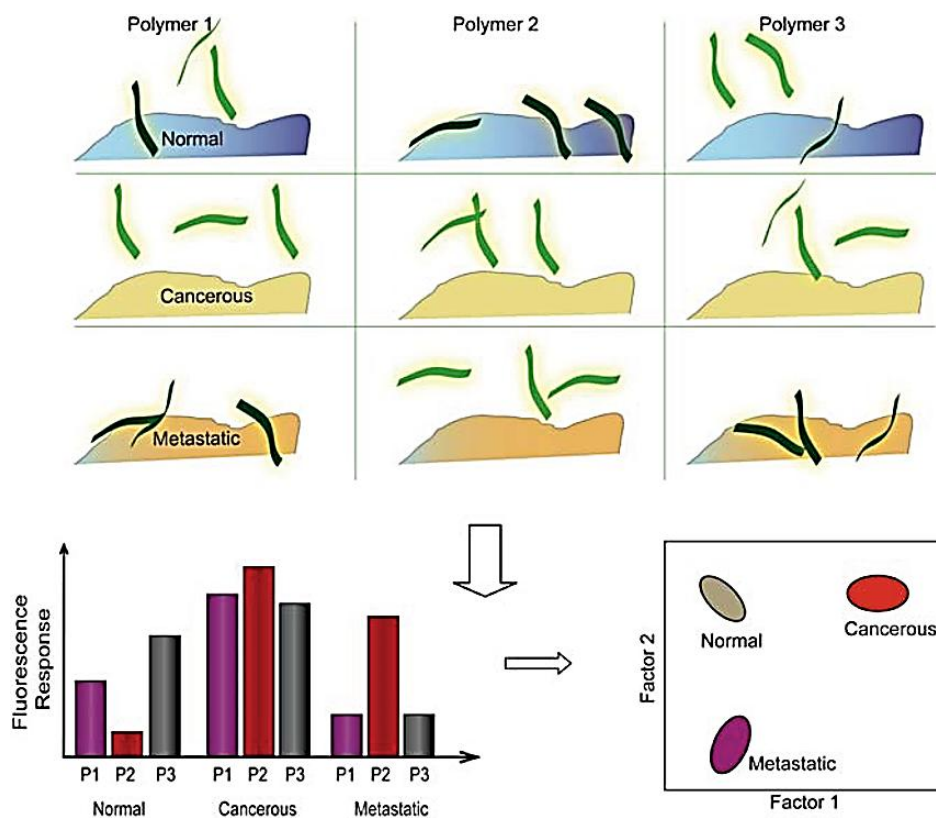


Figure 1-30. Schematic presentation of the cell detection assay by CPEs including signal response pattern and canonic score plot. Reprinted with permission from Bajaj, A., *et al.*¹²⁴

CPE based sensor arrays for efficient protein recognition have been increasingly reported and similar procedures as described above have been applied and high accuracies have been obtained (97% for 17 proteins as reported by Bunz and Rotello⁹⁷). Unlike the conventional specific markers design, the CPE sensory recognition elements do not need to be attached covalently, as they self-assemble onto the surface of cells or proteins via non-specific interaction. Without proficient manipulation and strong biological background, an ordinary technician can accomplish the test smoothly. Although having so many outstanding strengths, those novel sensor arrays still need further development in more complicated biological environments to eliminate potential interference and improve their feasibility in the real world.

Linear Discriminant Analysis

There are many tools available for the analysis of data from an array of chemical sensors. Basically, two methods are appropriate for classification purpose: if only independent variable information is required (unsupervised mode), principal component analysis is suitable; while for those that need dependent variable information (supervised mode), such as analyte classes, the linear discriminant analysis (LDA) can be applied.¹²⁵ In this dissertation, a set of data with known categories is needed to be classified in Chapter 4, where a protein sensor array is developed. LDA is more suitable for data processing and analysis and so that only LDA will be emphasized in this section.

LDA is used to separate classes of objects or assign new objects to appropriate classes by analyzing the variances between classes and within classes.¹²⁶ As one type of chemometrics, LDA tests multivariate differences between classes, optimizes the dimensionality of class, calculates the relative importance or contribution factor for each variable and classifies known and unknown objects into groups. The discriminants are

linear combinations of the measured variables, typically, in a sensor array, sensor responses. Consider that a sensor array with n variables (probes) is used to differentiate k classes of analytes, for each mixture or treatment, i.e., one analyte with one probe, m replicates are performed, so we have m sets of data for each mixture. Let t represent the individual observation for each measurement, so $t_{n m}$ is the observation for n^{th} probe at m^{th} measurement for a certain analyte. For i^{th} class, the data matrix abstracted from each measurement for this class of analyte can be written as follows,

$$X_i = \begin{bmatrix} t_{11} & \cdots & t_{1m} \\ \vdots & \ddots & \vdots \\ t_{n1} & \cdots & t_{nm} \end{bmatrix}_i \quad i = 1 \dots k \quad (1-3)$$

Take an average over the m sets of data for each probe-analyte mixture,

$$\bar{X}_i = \begin{bmatrix} \bar{t}_1 \\ \vdots \\ \bar{t}_n \end{bmatrix}_i, \quad \bar{t}_j = \frac{t_{j1} + \cdots + t_{jm}}{m}, \quad i = 1 \dots k, j = 1 \dots n \quad (1-4)$$

Where \bar{t}_j is the average of j^{th} row in each submatrix. The whole data matrix X ($k \times n \times m$) is:

$$X = \begin{bmatrix} X_1 \\ \vdots \\ X_k \end{bmatrix} \quad (1-5)$$

Let \bar{X} be the total average matrix:

$$\bar{X} = \frac{(\bar{X}_1 + \cdots + \bar{X}_k)}{k} \quad (1-6)$$

The between classes sums of squares matrix B representing the variance between classes is expressed as:

$$B = \sum_{i=1}^k (\bar{X}_i - \bar{X})(\bar{X}_i - \bar{X})^T \quad (1-7)$$

The covariance matrix can be computed as

$$S_k = \frac{1}{m-1} \begin{bmatrix} (t_1 \ 1 - \bar{t}_1) & \cdots & (t_1 \ m - \bar{t}_1) \\ \vdots & \ddots & \vdots \\ (t_n \ 1 - \bar{t}_n) & \cdots & (t_n \ m - \bar{t}_n) \end{bmatrix} \times \begin{bmatrix} (t_1 \ 1 - \bar{t}_1) & \cdots & (t_1 \ m - \bar{t}_1) \\ \vdots & \ddots & \vdots \\ (t_n \ 1 - \bar{t}_n) & \cdots & (t_n \ m - \bar{t}_n) \end{bmatrix}^T \quad (1-8)$$

So that the combined covariance matrix is:

$$S = \frac{S_1 + \cdots + S_k}{k} \quad (1-9)$$

The within class sums of squares matrix representing the variance within class is displayed as:

$$W = (m - 1) \times k \times S \quad (1-10)$$

The key objective for discriminant analysis is to figure out the best way to let $W^{-1}B$ to be the maximum, i.e., the distance between classes relative to the variance within classes is maximum. It can be achieved by calculating the eigenvectors e s of $W^{-1}B$ and scaling them such that

$$e_j^T S e_j = 1 \quad (1-11)$$

where e_j denotes the j^{th} eigenvector ($j \leq k - 1$):

$$W^{-1}B e_j = \lambda_j e_j \quad (1-12)$$

The eigenvalue λ_j can be treated as the contribution factor, i.e., how important of its eigenvector for transmitting the data information. Usually, we use the percentage of the value λ_j took over total eigenvalue, $\lambda_j / \sum_{j=1}^s \lambda_j \times 100\%$, to represent its importance. For a given n-dimensional sample vector t that belongs to a certain class, it will be projected to a new discriminant space by the operation e_j . In the new space, it is believed to be better separated from the samples that belong to other classes while getting closer to the samples that belong to the same class. So that it will have a new coordinates calculated by $e_j^T t$. Normally, s discriminant functions are available ($s = \min(n, k-1)$), so that there are s sets of eigenvalues and eigenvectors. For $s \leq 3$, the sample

can be graphically displayed in a 2D plane or 3D space. For $s > 3$, the three most important discriminant functions, usually carrying more 80% information/variation in total, can be used to create the canonic plot, although the samples may not be 100% discriminated based on the plot.

When referring to the unknown sample test, the essential rule is to assign the unknown sample to the nearest class after it undergoes the same operation to the identical discriminant space. Assume \mathbf{t}_{un} is the vector for the unknown sample, if for all $l \neq i$

$$\sum_{j=1}^s [\mathbf{e}_j^T (\mathbf{t}_{un} - \bar{\mathbf{X}}_l)]^2 \leq \sum_{j=1}^s [\mathbf{e}_j^T (\mathbf{t}_{un} - \bar{\mathbf{X}}_i)]^2 \quad (1-13)$$

\mathbf{t}_{un} is classified to the group of l . This assignment is quantitatively performed in terms of comparing the distance between the spot of unknown sample and the center of the classes in the discriminant space.

As the data for the unknown samples must undergo the operation that set up for the standard/training data, i.e., they will be projected to the same discriminant spaces, the sensing probes as well as the discriminant method must be carefully evaluated and a high accuracy for classification is preferred when handling the training data. If a low accuracy is obtained, it means the current probes or method are not sufficient to discriminant the classes, which will lead to incorrect identification of unknown sample. Therefore, a modification or replacement of probes/method needs to be considered. The last step for the analysis will be verification, that is, use a well-defined method to test the unknown sample and validate the result of LDA. The method varies from one sensor to another, relying on the properties of the signal and samples themselves.

Fluorescence Correlation Spectroscopy (FCS)

Basic Principle of FCS

Investigation of conformation or aggregation state change of CPE under various circumstances and the interaction between CPE and other molecules has been extensively conducted mainly through fluorescence spectroscopy or UV-Vis spectroscopy. Researches utilize the color (absorption) or glow (fluorescence) changes to conjecture the inner situation including inter- or intra- molecular interaction. Other techniques including X-ray scattering,^{127, 128} light scattering,¹²⁹ fluorescence anisotropy,¹³⁰ fluorescence correlation spectroscopy^{131, 132} are also involved in the exploration. Among them, fluorescence correlation spectroscopy (FCS) is emerging as a powerful tool that can achieve single molecular analysis. FCS is a statistics-based analytical technique, first introduced in the early 1970s by Madge, Elson and Webb,¹³³ which monitors the spontaneous fluctuations of fluorescent intensity of diffusing molecules within a small excitation volume (~femtoliter). Various processes including Brownian diffusion, chemical reaction or flow contribute to the fluorescence intensity fluctuations. By applying an autocorrelation function $G(\tau)$, the raw fluctuations data are converted to a decay curve, which can be analyzed by an appropriate fitting model. The important dynamic and kinetic information for a particular molecule or particle can be obtained, thus the related chemical reaction, physical interaction between molecules or change in chemical environment is revealed. The FCS is somewhat similar to another correlation related technique-dynamic light scattering (DLS). However, instead of recording the light from all the particles showing up in the excitation volume, it only focuses on the fluorescent species and this specificity can be further enhanced by selecting an appropriate emission filter.

Application of FCS

FCS has shown its large potential in many applications,¹³⁴⁻¹³⁶ e.g., study of translational¹³⁷⁻¹³⁹ and rotational diffusion,^{140, 141} protein folding,¹⁴² ligand-macromolecule binding,^{133, 143-146} hybridization reactions¹⁴⁷ in bulk solution, on surfaces or in cells.¹⁴⁸⁻¹⁵² Although FCS has been primarily employed to the analysis of biological systems, application of FCS on polymers has gained increasing interest throughout the past decade due to its high sensitivity and ability to effect single molecule analysis. For example, Van Rompaey and coworkers studied interaction between a dye labeled biomolecule and a polymer formed pharmaceutical carrier,¹⁵³ Bonn  and coworkers focused on the aggregation behavior of dye labeled diblock copolymer poly(2-alkyl-2-oxazoline),¹⁵⁴ Laguecir and coworkers investigated the conformational behavior of the dye labeled poly(acrylic acid) affected by size and pH.¹⁵⁵ Most of those applications utilized a specific dye as a tracer or directly labeled the polymer with a fluorophore. Normally, those dye molecules or fluorophores can be excited by a laser line with a specific wavelength, typically, 543 nm for rhodamine, and 488 nm for Alexa 488. Therefore, the diffusion behavior of the fluorescent molecules or particles can be monitored and the chemical environment can be deduced.

Because of their inherent fluorescence, CPEs can be observed directly using FCS. Avoidance of the tedious dye-labeling process on the target molecule makes the study of conformational or diffusional changes of the CPE via FCS simpler and more direct. For example, Jayakannan and coworkers have systematically studied the influence of chain length and molecular weight distribution on the diffusion dynamics of CPE at the single molecular level by FCS.¹⁵⁶ Cotlet and coworkers investigated the solvent polarity effect on chain conformation using FCS measurements.¹⁵⁷ By employing a FCS coupled

with a time correlated single photon counting (TCSPC) device, Masuo and coworkers determined the relationship between the probability of single photon emission and the spatial size of the CPE chains.¹⁵⁸ Most of these applications utilized a laser beam with a wavelength ≥ 460 nm as light source. However, most of the commonly used CPEs have λ_{max} close to 400 nm. Consequently, an FCS equipped with a 405 nm blue diode laser specifically for CPE detection was constructed in our lab. As far as we know, only a few papers focus on the use of FCS with a short wavelength laser, specifically, 405 nm.^{159,}¹⁶⁰ Even fewer technical data or details can be found in the literature for the construction of such a FCS system. Details about the construction will be discussed in the second chapter.

Overview of This Dissertation

This dissertation is aimed at investigating the interaction between the CPEs and other molecules including dye-ligand compounds, proteins and metallic ions as well as their sensor application for metal ions and proteins by using various optical technologies, especially, fluorescence correlation spectroscopy.

In the second chapter, the theory of FCS, including its autocorrelation function, basic equations, single-species fitting as well as the relationship between the diffusion time and molecular weight, is introduced. Then it is followed by the details in the construction of FCS setup with 405 nm diode laser. The function of each component of the setup, laser alignment and system optimization are fully described. Examination of the setup and the test results further validate the feasibility of the instrument.

Chapter 3 is composed of two parts. In the first part, a tetramethylrhodamine labeled biotin (biotin-TMR) intercalated helical CPE probe is developed as an avidin sensor by fluorescence spectroscopy through the technique of fluorescence resonance

energy transfer. In the second part, an FCS system coupled with 543 nm laser, particularly for TMR study, is employed to further study the above system. The formation of large aggregates in solutions containing helical CPE/TMR-biotin with avidin is demonstrated, giving rise to a new avidin sensing strategy. The detection limit less than 100 nM makes this method among the most sensitive avidin sensors that have ever been reported.

In the fourth chapter, study of conformation change of CPEs induced by proteins as well as the development of array-based sensing of proteins through the FCS system with 405 nm laser is conducted. A systematic study on the interaction between six different types of CPE and seven target proteins are carried out. The resulting 2D bar or 3D column response graph displays a unique signal response pattern for each protein, which is sufficient to build up a sensor array for proteins. The discriminant functions and canonic score plots obtained through linear discriminant analysis are and employed for further unknown sample test. The high accuracy of 93% for identifying unknown samples well proves the feasibility of this novel protein sensor array.

Finally, a study of meta-linked poly(phenylene ethynylene) sulfonate containing pyridine (mPPESO₃py) quenched by metallic ions is conducted in Chapter 5. The high quenching efficiency for Pd²⁺ over other metallic ions on mPPESO₃py is demonstrated by comparing their Stern-Volmer plots, giving rise to a new Pd²⁺ sensing system. Then FCS data reveals that some multivalent ions, such as Cr³⁺, Fe³⁺, can crosslink mPPESO₃py and induce the aggregation. However, aggregation is not the dominant element in the fluorescence quenching process of mPPESO₃py.

CHAPTER 2

CONSTRUCTION OF A FLUORESCENCE CORRELATION SPECTROSCOPY

As discussed in Chapter 1, fluorescence correlation spectroscopy (FCS) has already shown its power in detecting chemical and physical change of fluorescent molecules, particularly conjugated electrolytes (CPEs). An FCS system equipped with a 405 nm blue diode laser specifically for CPE study was constructed in our lab. As far as we know, only a few papers focus on the use of FCS with a short wavelength laser beam, specifically, 405 nm.^{159, 160} Even fewer technical data or details can be found in the literature for the construction of such an FCS system. In the current chapter, the details for construction, optimization and calibration of an FCS system coupled with a 405 nm diode laser will be provided.

Theory of FCS

This section follows closely the classical paper reported by Haustein and Schwille.¹⁶¹ Figure 2-1 illustrates the working principle for FCS. The measurement is accomplished by focusing an excitation laser beam onto the sample through an objective lens to form an ellipsoid-like femtoliter volume (Figure 2-2), and then collecting the fluctuating emission signals within the excitation volume. The autocorrelation function, $G(\tau)$, defined as

$$G(\tau) = \frac{\langle F(t) \cdot F(t+\tau) \rangle - \langle F(t) \rangle^2}{\langle F(t) \rangle^2} = \frac{\langle \delta F(t) \cdot \delta F(t+\tau) \rangle}{\langle F(t) \rangle^2} \quad (2-1)$$

is used to characterize the temporal fluctuation that is treated as “fingerprint” for a typical species. $\delta F(t) = F(t) - \langle F \rangle$ in Equation (2-1) represents the fluctuation of the fluorescence signal $F(t)$ as the deviations from the temporal average of the signal $\langle F \rangle$ at time t . $G(\tau)$ helps convert the raw data to a decay curve, which represents the similarity between the signal and replicate of the same signal but shifted with a time lag

τ (Figure 2-3).¹³⁶ In the early time period, typically $\tau < 10^{-6}$ s for most systems, the correlation curve is much noisy due to the after-pulse effect of avalanche photo diodes (APD), which is one of the major detector non-idealities that affect the output.¹⁶² There are some methods for after-pulse effect handling, such as coupling in one more detector pair in the system for cross-correlation,^{163, 164} or using a mathematical model to fit the after-pulse.¹⁶⁵ However, in this dissertation, only the information provided by the FCS curve without after-pulse part, i.e., $\tau > 10^{-6}$ s for small molecules and $\tau > 10^{-5}$ s for large molecules, is considered.

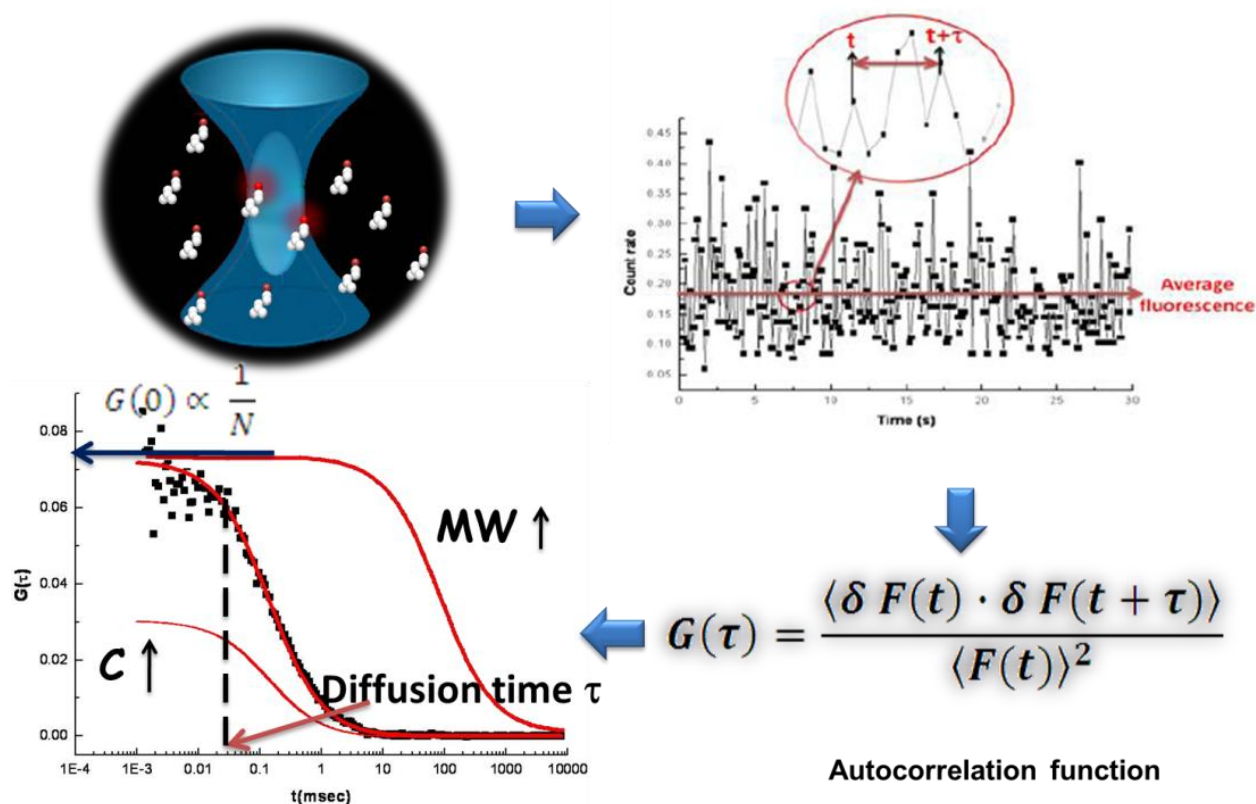


Figure 2-1. Working principle for FCS.

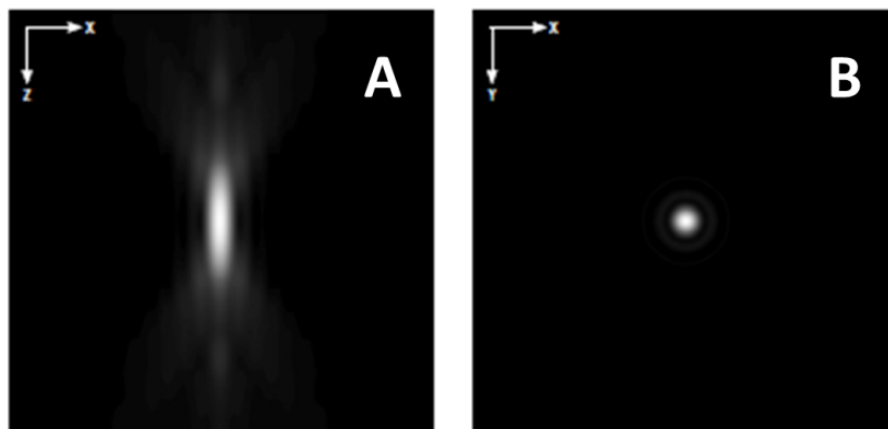


Figure 2-2. The excitation volume in A) Z direction and B) X-Y planar as generated by a diffraction-limited objective lens. Reprinted with permission from Wilhelm, S.¹⁶⁶

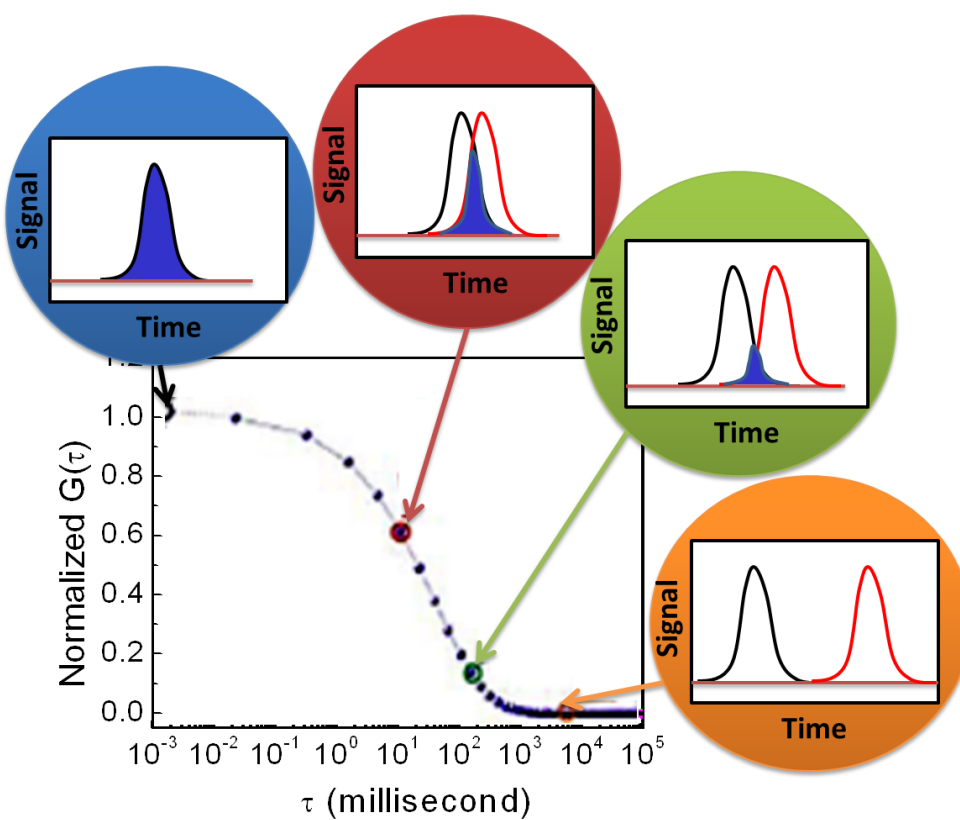


Figure 2-3. Development of an autocorrelation curve. Adapted with permission from Schille, P. *et al.*¹³⁶

The three-dimensional (3D) and two-dimensional (2D) fitting models are commonly used for fitting the correlation curve of a single-component system. The 3D equation is written as:

$$G_{3D}(\tau) = \frac{1}{N} \times \frac{1}{1 + \frac{\tau}{\tau_D}} \times \frac{1}{\sqrt{1 + \frac{\tau}{\omega_z^2 \times \tau_D}}} \quad (2-2)$$

In Equation 2-2, ω , the structure parameter, equates to $\frac{\omega_z}{\omega_r}$, where ω_z is the longitudinal radius and ω_r is the transversal or waist radius of the confocal volume (Figure 2-4); N is the average number of fluorescent molecules in the detection volume; τ_D is the average time of fluorescent molecules diffusing in the well-defined detection volume, which is characteristic of a specific molecule or particle.

When $\omega_z \gg \omega_r$, $\omega \rightarrow \infty$, $\frac{1}{\sqrt{1 + \frac{\tau}{\omega^2 \times \tau_D}}} \rightarrow 1$, a 2D model is obtained:

$$G_{2D}(\tau) = \frac{1}{N} \times \frac{1}{1 + \frac{\tau}{\tau_D}} \quad (2-3)$$

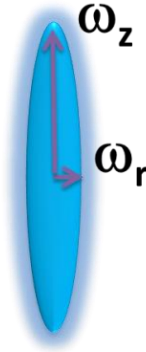


Figure 2-4. Ellipsoid-like excitation volume formed by the objective lens.

In general, two important parameters can be obtained through the fitting: the diffusion time τ and number of fluorescence molecules inside the excitation volume N , which is the inverse of $G(0)$, i.e., the reciprocal value of $G(\tau)$ when τ approaches to 0 (Figure 2-1). According to the diffusion concept, small molecules move more rapidly through the excitation volume than larger ones. So the FCS curves of larger molecules will reflect the longer diffusion time and a significant retardation of the diffusion of small fluorescent molecules can be expected when they interact with larger macromolecules.

While the increase in concentration of the molecules will cause the decrease of $1/G(0)$ accompanied with decrease of the correlation curve amplitude (Figure 2-1).

The relationship of τ_D to the molecular diffusion coefficient D (m^2s^{-1}) is given by:

$$\tau_D = \frac{\omega_r^2}{4D} \quad (2-4)$$

The waist radius is obtained from its rearranged equation

$$\omega_r = \sqrt{4D_{free\ dye} \cdot \tau_D} \quad (2-5)$$

where $D_{free\ dye}$ is the diffusion coefficient of the standard calibration dye.

The effective detection volume V_{eff} is obtained from the concentration of analyte, C , and the number of diffusing particles inside the detection volume, N :

$$V_{eff} = \frac{N}{N_A \cdot C} \quad (2-6)$$

where N_A is Avogadro's Constant. The longitudinal radius ω_z can be simply obtained from below:³⁵

$$V_{eff} = \pi^{3/2} \cdot \omega_r^2 \cdot \omega_z \rightarrow \omega_z = \frac{V_{eff}}{\pi^{3/2} \cdot \omega_r^2} \quad (2-7)$$

Usually, the 2D model is used to initially fit the standard dye sample for calibration.

By using equations 2-4, 2-5, 2-6, and 2-7, the structure parameter ω can be calculated.

As long as the experimental conditions (excitation wavelength, excitation power, cover glass thickness, solvent and immersion medium, emission filter and position of optical elements) are the same during the measurement, the detection volume theoretically does not change and neither does ω . Once the value of ω is obtained, the 3D model with the ω can be employed further to fit the other samples.

The translational diffusion coefficient, D , of a molecule is related to its size by the Stokes-Einstein equation

$$D = \frac{kT}{6\pi\eta R} \quad (2-8)$$

where k is Boltzmann's constant; T is the temperature; η is the viscosity of the solvent; and R is the hydrodynamic radius. This equation can be used to estimate the size of diffusing particles by assuming that the particles are spherical with radius R . R is related to the molecular weight (MW) of the molecule with a specific gravity \bar{v} by¹⁶⁷

$$V = MW\bar{v} = \frac{4}{3}\pi R^3 \quad (2-9)$$

where V is the molecular volume. Thus we have

$$R = \left(\frac{3MW\bar{v}}{4\pi} \right)^{1/3} \quad (2-10)$$

These equations show that the radius R and diffusion coefficient D are weakly dependent on the molecular weight. By combining Equation 2-8 and 2-10, we have:

$$D = \left[\frac{kT}{6\pi\eta} \left(\frac{4\pi}{3\bar{v}} \right)^{1/3} \right] MW^{-1/3} \quad (2-11)$$

This relationship is useful for estimating the MW of a spherical particle from its diffusion coefficient.

Construction of FCS System

An FCS system coupled with a 405 nm diode laser source was constructed in the lab. The basic setup is displayed in Figure 2-5. Details about the function of each component and the instrument construction including alignment, optimization and calibration will be described next.

Laser Optimization and Alignment

Blue (405 nm) diode Laser

The continuous-wave laser beam ideally satisfies high quality and stability requirements for FCS light source. Since most of our CPEs have high absorbance around 400 nm, a packaged, blue-violet diode laser (405 nm), is used in our system. A near Gaussian distributed and symmetric circular laser beam is critical for achieving high performance in FCS measurements. However, the laser beam from the packaged

diode laser has asymmetric dimensions and divergence in the X and Y directions due to the asymmetry of laser export slit, which strongly affects the formation of a well-shaped confocal volume in the sample. Additional assemblies including a fiber coupling spatial filter, a single mode fiber, and a fiberport collimator are employed to reshape, optimize and collimate the laser beam.

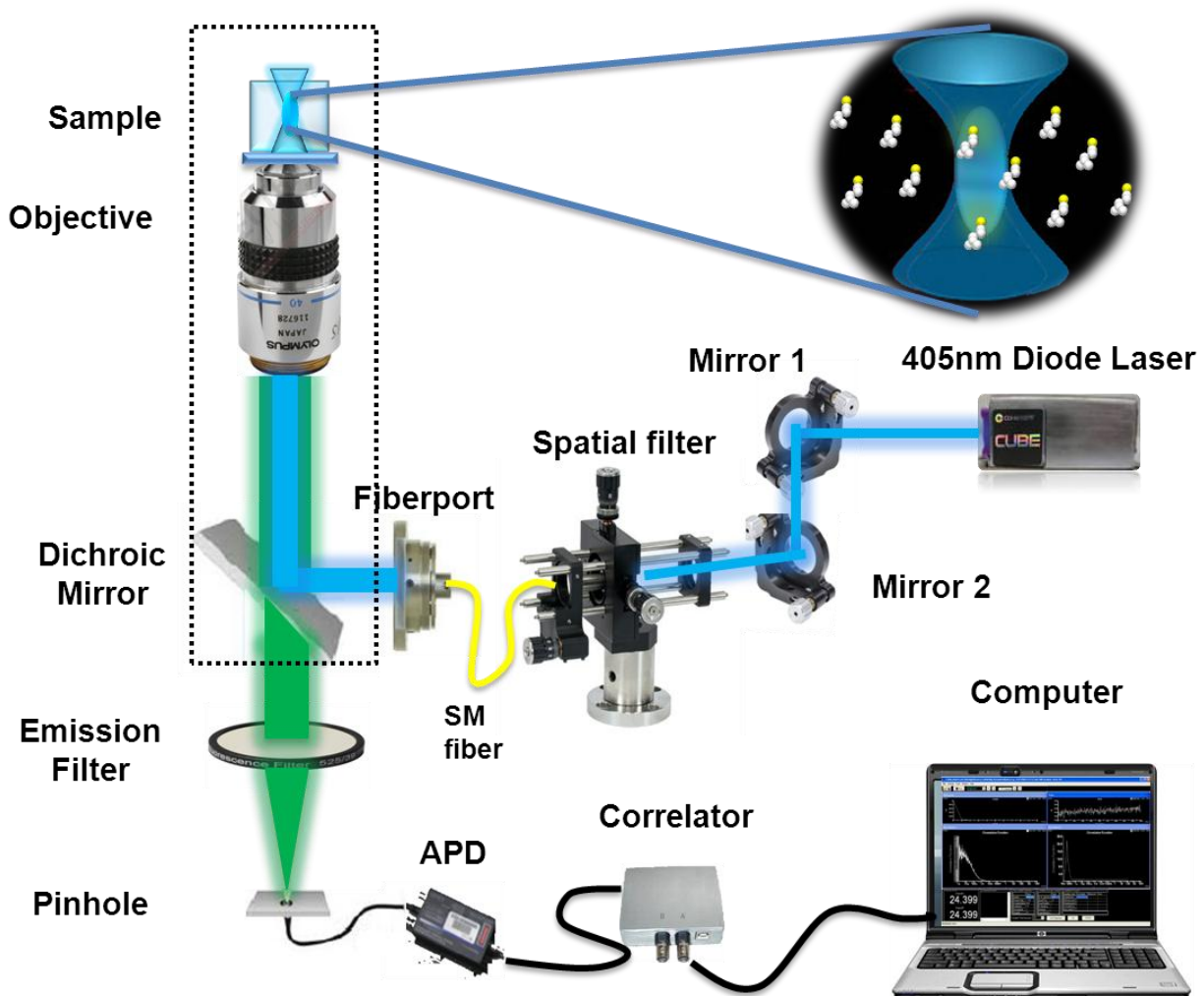


Figure 2-5. Schematic diagram of the FCS setup described in the text. Black dash line represents the outline of fluorescence microscope.

Fiber coupling spatial filter and fiberport

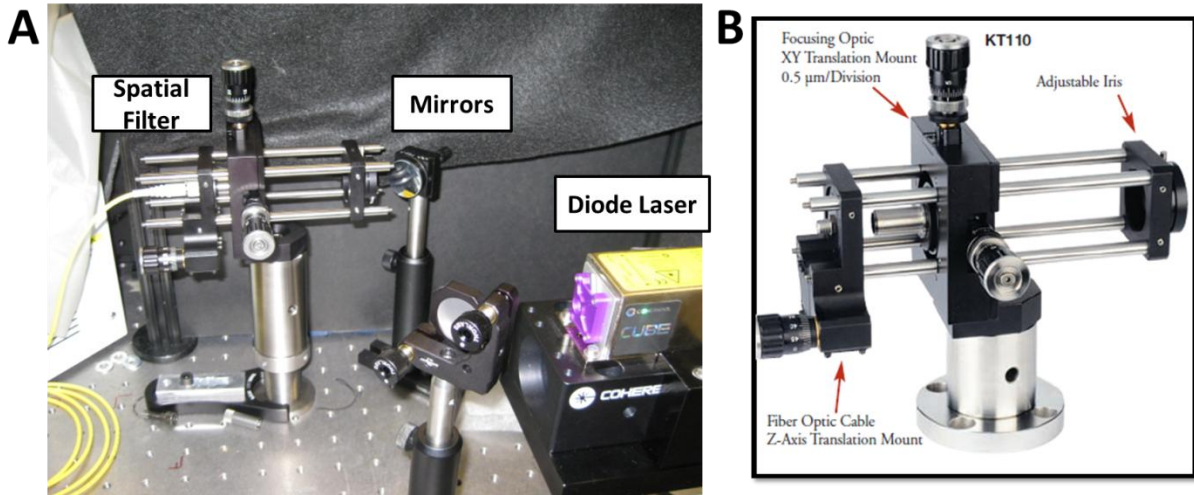


Figure 2-6. Photographs for A) excitation part of FCS setup and B) fiber coupling spatial filter. Figure B is reprinted with permission from Thorlabs.¹⁶⁸

A fiber coupling spatial filter system (Figure 2-6B) is used for producing a clean, spatially uniform, Gaussian beam. In our setup, this spatial filter is positioned after a pair of angle-adjustable mirrors (Figure 2-6A). By carefully tuning the two adjusters on each mirror, original laser beam is aligned straight into the center of a size-adjustable iris in the front of the spatial filter. Then the input intensity-noisy laser beam is first roughly filtered through the small iris. By slowly adjusting the X, Y adjusters on the focusing optic translation mount in the middle of the spatial filter, the laser beam is directed to the center of an aspheric lens that attached to the optical tube on the middle mount. A fiber that is mounted on the Z translator is carefully positioned at the focal point of the aspheric lens, allowing laser beam to be focused into the pinhole on the fiber. This optical fiber, which is a 405 nm single mode (SM), acts as a second spatial filter, allowing only the Gaussian profile of laser beam with wavelength 405 nm to transmit.

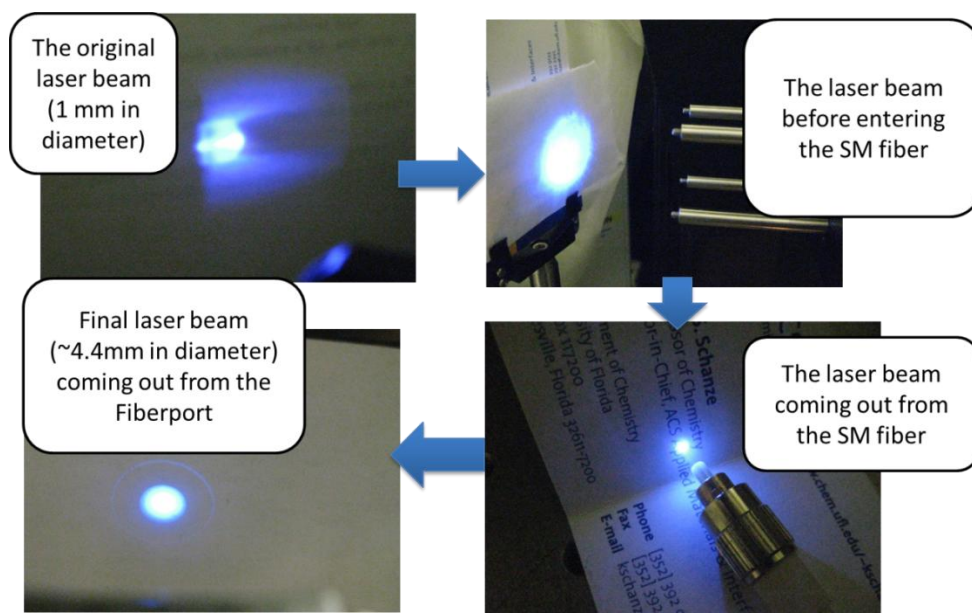


Figure 2-7. Cross-sections for laser beam in each optimization step.

A beam of light comes out through the end of the fiber, where a fiberport collimator is well connected (Figure 2-8B). Incorporated with another aspheric lens, the fiberport not only collimates but also expands the laser beam. The cross-sections for the laser beam in each optimized step are displayed in Figure 2-7 for comparison. A remarkable improvement in the laser beam quality is easily observed.

Dichroic Mirror Cube and Laser Alignment

After the filtration and expansion, a collimated, horizontally straight and clean laser beam with a circular and symmetrical cross-section, is obtained. The final diameter for laser beam is ~4.4 mm, which is more than four times larger than that of the original beam (~1 mm). This beam slightly underfills the back aperture of the objective lens. The collimated laser beam then enters the back port of an Olympus IX70 inverted microscope (Figure 2-8), reaching a 405 nm dichroic mirror incorporated in the filter cube. This dichroic mirror is designed so that it reflects more than 90% of the incident light, whose wavelength is ~405 nm, while transmitting more than 90% of the light with

wavelength above 405 nm. With an incidence angle of 45°, the dichroic mirror helps to redirect the incident laser beam upwards to the water immersion objective lens (Figure 2-9).

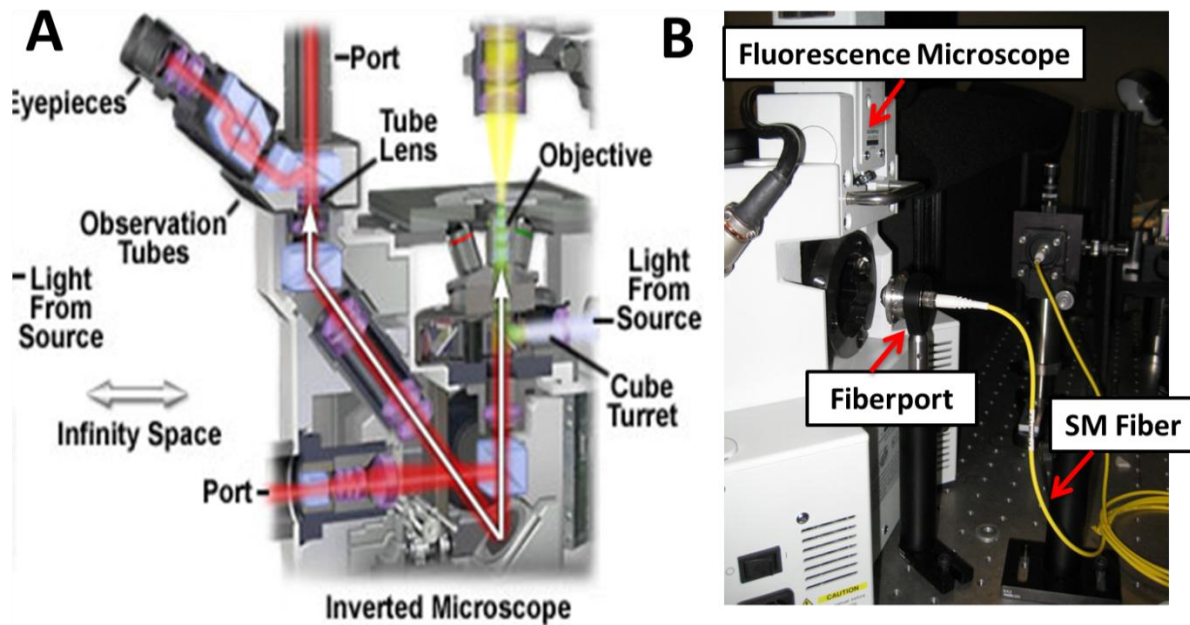


Figure 2-8. A) Inner structure of fluorescence microscope and B) photograph for a part of the setup. Figure A is reprinted with permission from Olympus.¹⁶⁹

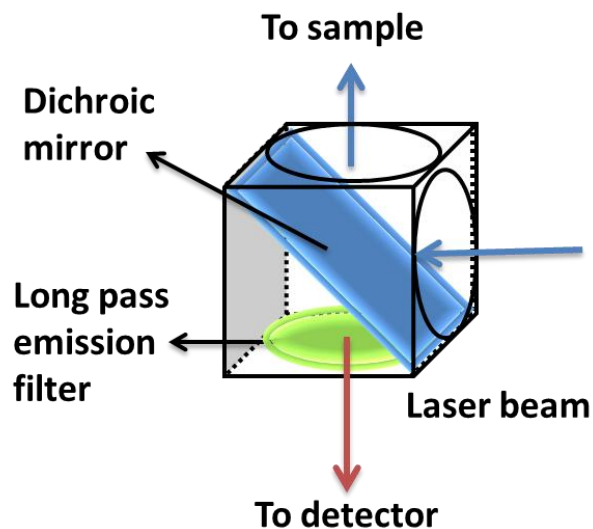


Figure 2-9. Diagram of the dichroic mirror cube.

The beam axis needs to be aligned so that the reflected axis is coincident with that of objective lens. Before screwing in the microscope objective, the alignment needs to be checked by applying two pieces of paper adhesive tape on the top of round objective lens holder and the round hole in center of the sample holding plate. If the laser beam has been well aligned, the reflected excitation spots are centered on both round circles. After the objective is placed, the laser beam coming out should be located on the center of the hole in the sample holding plate as well.

Objective Lens and Focusing

A small spot volume at the focal point in the sample is critical for achieving single molecule detection and reducing background noise in FCS measurements. The factors that affect the full width half maximum (FWHM) of the diffraction limited excitation spot formed by the objective lens, can be found in the following equation:¹⁷⁰

$$FWHM = 0.71 \times \frac{\lambda}{NA} \times \sqrt{0.51 + 0.28 \times \left(\frac{d_{pupille}}{d_{laser}}\right)^2} \quad (2-12)$$

Where λ is the wavelength of light; NA is the numerical aperture of the objective lens used; d_{laser} and $d_{pupille}$ are the diameters of the laser beam and lens pupil, respectively. The Equation 2-12 shows that shorter beam wavelength, higher objective NA , or larger laser beam diameter would lead to smaller focus. Theoretically, once the types of laser and objective lens are fixed, only expanding the laser beam would shrink the focal volume. Thus a beam expander is a necessity for most FCS systems. However, although overfilling the back aperture of the objective lens by the laser beam would form the smallest spot size with diffraction limited size, the intensity distribution inside the focal volume is complicated and may not be described by a simple model. A more desirable Gaussian intensity distribution in a small volume is achieved by

underfilling the back aperture of the objective, although trading off with a larger excitation volume.¹⁷¹

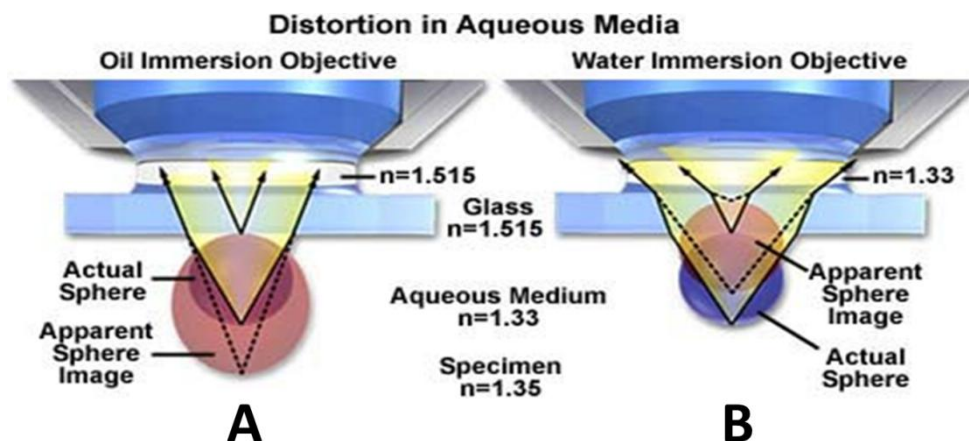


Figure 2-10 Effect of objective media A) oil immersion objective B) water immersion objective. Reprinted with permission from Olympus.¹⁷²

As one of the most critical components of the system, objective lens should be selected carefully. A higher NA of the objective lens is desirable for producing a small beam waist (Equation 1-12) as well as efficiently collecting signals. Most of the oil immersion objective lenses have NA as high as 1.5. However, a mismatch of the refractivity of the medium and sample would cause deviation of the light rays.¹⁷² For instance, using an oil immersion objective lens (refractive index ~ 1.5 for oil medium) in aqueous sample (refractive index ~ 1.33) detection may limit the position of focus point quite close to the bottom glass of sample container, so called a “shallow” focus, which would jeopardize the quality of an FCS measurement (Figure 2-10). Moreover, the working distance of the lens becomes smaller as its NA becomes larger. Since most of our measurements are done in aqueous solution, a $60\times$ water-immersion objective lens with $NA = 1.2$ is suitable. According to the working distance of our objective lens, the excitation volume is formed about $220\text{ }\mu\text{m}$ above the glass-sample interface,¹⁷³ which is relatively “deep” in the solution.

Signal Collection and Detection

The fluorescence is collected by the same objective and separated from the incident laser line through the dichroic mirror. After passing a long-pass 420 nm filter in the bottom of the dichroic mirror cube (Figure 2-9), the emission signal exits the microscope through reflection by a 50/50 optic splitter (Figure 2-8A). A band-pass filter is installed next to the output (Figure 2-11A).

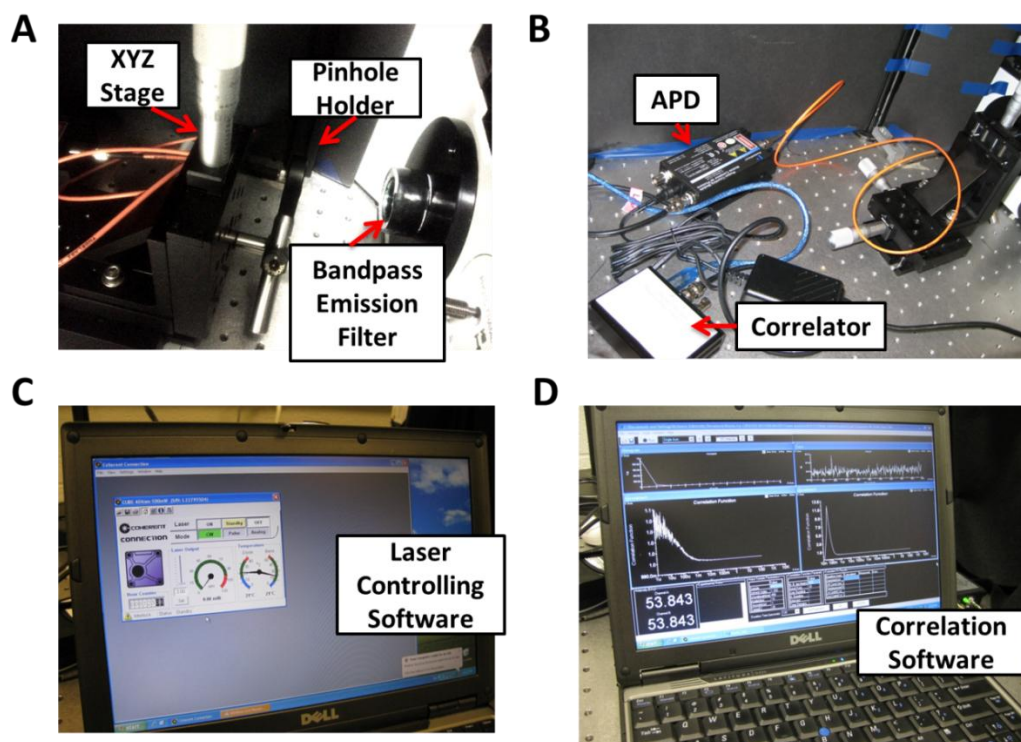


Figure 2-11. Photographs for signal detection and correlation components of FCS setup.

The filtered fluorescence is focused onto a pinhole, with 50 μm internal diameter, on one end of a multimode optical fiber (Figure 2-11A). The combination of the confocal optics components—collimator, dichroic mirror, objective lens and pinhole—help reduce out-of focus light and limit detection to the desired plane of “in-focus” light (Figure 2-12).¹⁷⁴ An XYZ travel translation stage is used to position the pinhole precisely (Figure 2-11A). The desirable detector for FCS is a sensitive single-photon counting avalanche

photodiode (APD) module, which has high quantum efficiency ($\geq 50\%$) between 500 nm and 700 nm which is the typical emission range for CPE. In this device, all the photon signals are converted to electronic signals and are amplified (Figure 2-11B). Then the signals are fed into a correlator (Figure 2-11D), where the autocorrelation function is calculated. The best result, i.e., smoothest autocorrelation curve, is obtained when the pinhole is correctly positioned.

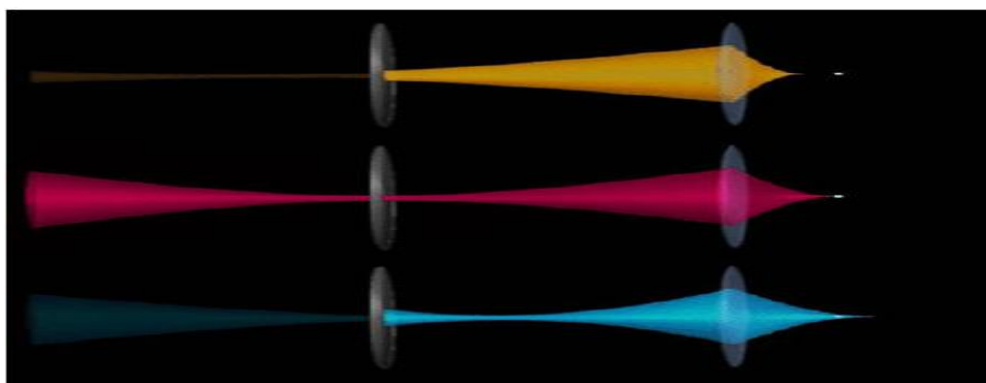


Figure 2-12. Confocal volume and optics. Only the “in-focus” emission (red) from the confocal volume passes through the pinhole. Others (yellow and blue) are blocked by the optics. Reprinted with permission from fcsxpert.com.¹⁷⁴

Potential Interference

To obtain higher signal-to-noise ratio and protect the detector, performance of FCS experiment in the dark is a requirement. Since the fluorescence fluctuation of the molecules is our measuring target, any external interference, such as vibration, needs to be avoided. Therefore, a stable heavy breadboard table, a black cover in the detection part and a quiet working place are preferred (Figure 2-13).

The laser power is controlled around 1 mW through software in computer (Figure 2-11C). Below that value, lack of intensity will affect the formation of the ellipsoid-like confocal volume as well as the signal detection, resulting in a poor FCS curve.

However, if the laser power intensity is too high, say 10 times higher, photobleaching or photon saturation occurs, which also affects the quality and accuracy of the results.

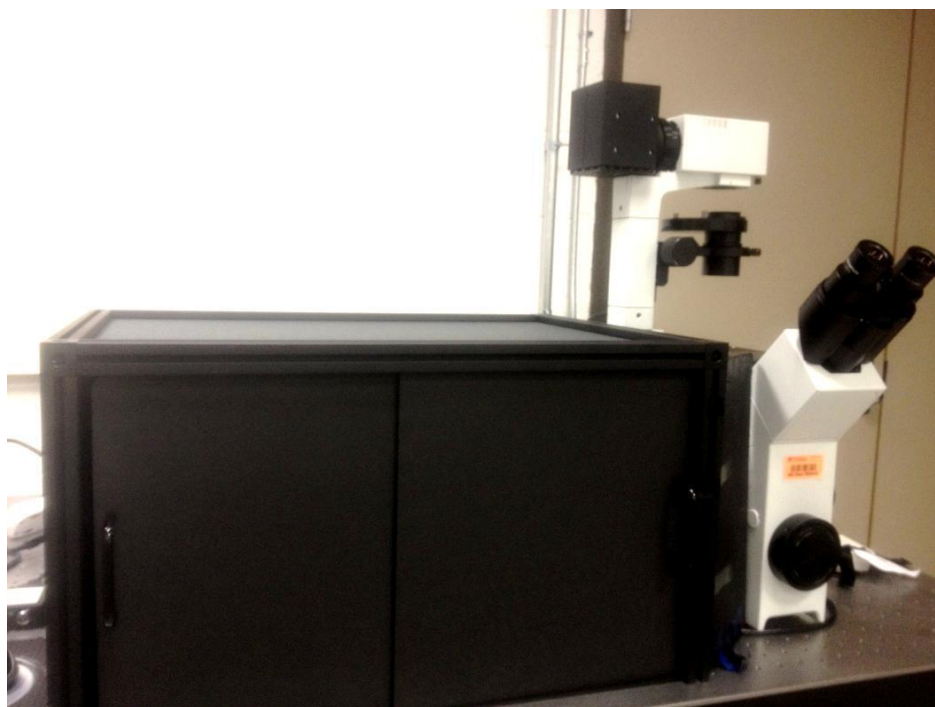


Figure 2-13. Black cover and breadboard for FCS setup.

Photobleaching is a problem which will cause an erroneously fast diffusion due to the fading of the fluorescence occurs before expected. In FCS, the photobleaching is easily observed on the fluctuation profile. The photobleaching-induced decrease in the fluorescence intensity causes a distortion on the FCS curve. Usually, a second FCS curve with longer diffusion time will show up. The recording of the fluctuation should be restarted until the stable fluorescence is obtained. It is rather important to monitor the fluorescence intensity change before saving the final FCS data.

Calibration

FCS can provide reliable information about diffusion coefficient and concentration values when the calibration is done properly. A stable and bright dye with a known coefficient is required for calibrating FCS system. Possessing high quantum efficiency

and large absorption cross section, the calibration dye must also have high photostability, which enables it to withstand the enormous power in the laser focus. In traditional FCS system, fluorescein, rhodamine and cyanine are the most popular calibrating dye. In our system, the dye must have absorbance peak extend to 405 nm, and have emission spectrum covering 450, 500, 600, or 650 nm.

In this dissertation, two emission filters at 500 nm and 600 nm are used for most of the CPEs having emissions cover either of the two wavelengths. With emission at ~500 nm, fluorescein is considered to be a good calibrating dye. Although its absorbance at 405 is relatively low, fluorescein is a pH sensitive molecule (Figure 1-2). A minor increase of pH to 8 will enhance the light absorption. Due to its high photostability and low container adsorption,¹⁷⁵ fluorescein tolerates a relatively long focusing time (>10 min) under the laser beam. For 600 nm emission system, although tetramethylrhodamine (TMR) suffers from low absorbance around 400 nm, however, the relatively high quantum yield enables it to emit relatively high intensity at 600 nm. The 2D model (Equation 2-3) is first applied to fit the FCS curve for a standard dye. The value for structure parameter ω is obtained and then it is substituted in the 3D model (Equation 2-2) to characterize the other FCS curves.

Calibration of system with standard dye should be done routinely before measurement and a recalibration is needed if the confocal volume is possibly changed for some reason, e.g., laser turned off or the optic elements realigned. For a stable system, the brightness or count rate is almost consistent for a standard dye with fixed concentration. Based on this, the routine measurement of dye sample not only helps calculating the size of confocal volume, but also keeps track on the quality of system.

Examination of FCS System

Various test experiments were conducted to examine the performance of the new instrument. The chemical structures of the compounds and polymers used in the work are shown in Figure 2-14, along with the acronyms that are used in the text. TMR and fluorescein in aqueous solution were used for calibration of the system with emission filters centered at 590 nm and 500 nm, respectively. The effective volume obtained for the confocal volume is *ca.* 0.5-1 femtoliter with ω_z in micrometers and ω_r in sub-micrometers. Based on the calculation method described above, the structure parameters are found to be 11 for emission at 590 nm, and 45 for 500 nm emission.

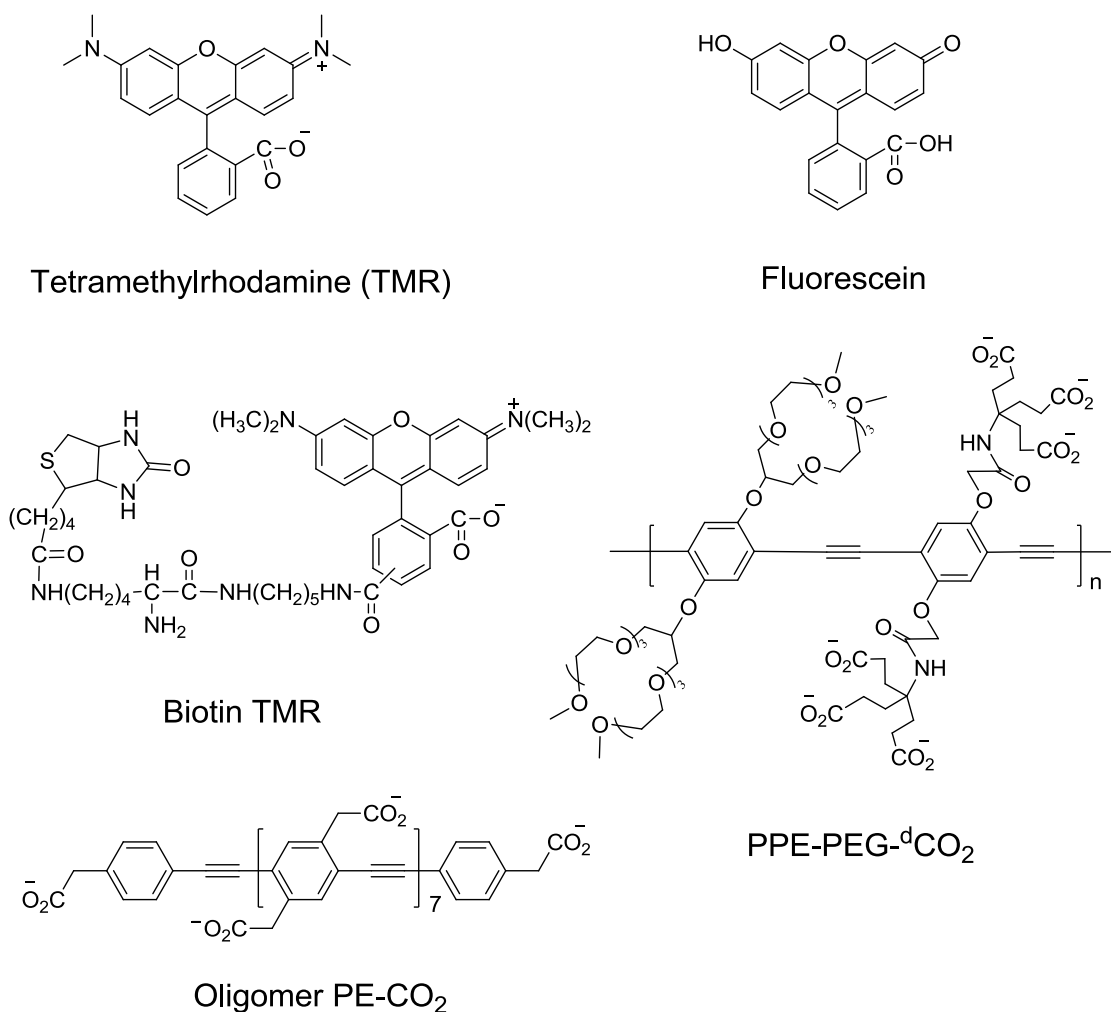


Figure 2-14. Structure of molecules that used in calibration and their acronyms.

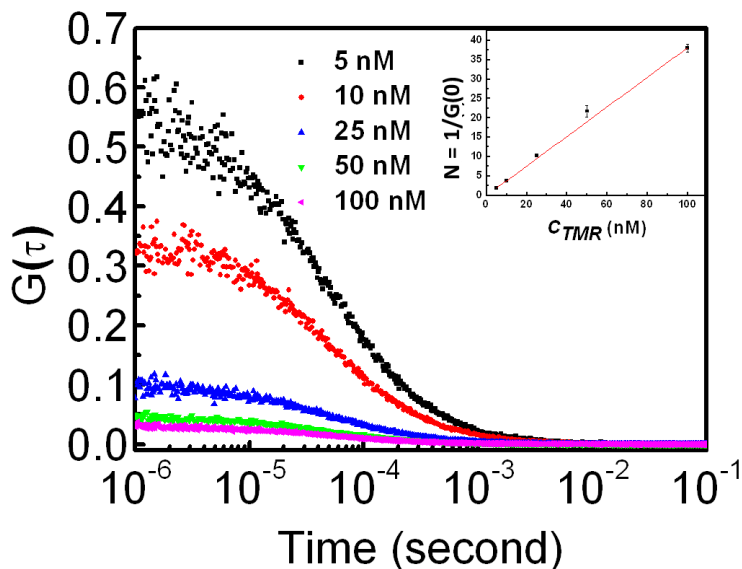


Figure 2-15. Correlation curves for TMR in water. From top to bottom the TMR concentrations were 5, 10, 25, 50, and 100 nM. The insert shows the measured average number of molecules.

A series of TMR samples with varying concentrations was tested with emission detection at 590 nm and the results are shown in Figure 2-15. As expected, due to the inverse relationship between $G(0)$ and the number of molecules in the confocal volume, a clear decrease of the correlation curve amplitude is observed as sample concentration is increased. The inset plot indicates that the number of molecules N , equal to $1/G(0)$, is linear with the increase in concentration.

A second test of the FCS setup was conducted by measuring the diffusion time of samples with different MW. In the 590 nm emission system (Figure 2-16 A), the experimentally observed diffusion time for TMR (386 Da) with a known diffusion coefficient $2.88 \times 10^{-10} \text{ m}^2 \cdot \text{s}^{-1}$ is $45.0 \pm 3.5 \text{ } \mu\text{s}$. Further FCS measurements were carried out on three samples, biotin-TMR (869 Da), TMR labeled DNA chain ($\sim 19,300$ Da), and biotin-TMR/avidin ($[\text{TMR}]/[\text{avidin}] = 1:10$, $\sim 67,000$ Da). The resulting diffusion times are 75.4 ± 0.6 , 165 ± 2 , and $294 \pm 12 \text{ } \mu\text{s}$, respectively. Based on Equation 2-4, the measured diffusion coefficients for each species are $(1.72 \pm 0.17) \times 10^{-10}$, $(0.79 \pm$

0.09×10^{-10} , and $(0.44 \pm 0.05) \times 10^{-10} \text{ m}^2 \cdot \text{s}^{-1}$. The diffusion coefficient of biotin-TMR $(1.72 \pm 0.17) \times 10^{-10} \text{ m}^2 \cdot \text{s}^{-1}$ is close to the value of $1.67 \times 10^{-10} \text{ m}^2 \cdot \text{s}^{-1}$ as previously reported by our group using a different FCS system (Chapter 3).¹⁷⁶ The diffusion coefficient of avidin/biotin-TMR $(0.44 \pm 0.05) \times 10^{-10} \text{ m}^2 \cdot \text{s}^{-1}$ compares well with the value $0.4 \times 10^{-10} \text{ m}^2 \cdot \text{s}^{-1}$ reported for streptavidin^{177,178} and $0.39 \times 10^{-10} \text{ m}^2 \cdot \text{s}^{-1}$ for avidin/biotin-TMR ([avidin]:[biotin]=1:4, 69,000 Da).¹⁷⁶ For those molecules/complex, the diffusion time increases with the increasing of the molecular weight. Assuming that they exhibit approximate spherical structure and the conditions for the highly diluted aqueous solvents (viscosity and temperature) are the same, based on the Equation 2-8, the hydrodynamic radii R_{HS} , which can be interpreted as an effective radii, are estimated to be 0.85, 1.42 ± 0.01 , 3.12 ± 0.04 and 5.55 ± 0.03 nm for TMR, biotin-TMR and biotin-TMR/avidin, respectively. The hydrodynamic radius of avidin with biotin TMR 5.55 ± 0.03 nm is larger than the value 4 nm reported for avidin-biotin complex in the literature, where the complex was modeled as a steric sphere having the same molecular volume.^{179, 180} Considering the non-spherical nature of avidin and the fact that R_{H} is the apparent size of the dynamic hydrated/solvated particle, the difference in the data is within acceptable limits.

In the 500 nm emission system (Figure 2-16B), fluorescein (332 Da) with diffusion coefficient $3.00 \times 10^{-10} \text{ m}^2 \cdot \text{s}^{-1}$ has the experimental diffusion time $23.5 \pm 3.3 \text{ } \mu\text{s}$. The oligomer PE-CO₂ (2,302 Da), PPE-PEG-^dCO₂ (~11,000 Da), and PPE-PEG-^dCO-DNA (~49,000 Da) were also investigated. Their diffusion times from shortest to longest as shown in Figure 2 are, 39.2 ± 4.0 , 54.8 ± 3.3 , $112 \pm 3 \text{ } \mu\text{s}$. The corresponding diffusion coefficients are $(1.80 \pm 0.24) \times 10^{-10}$, $(1.29 \pm 0.14) \times 10^{-10}$, and $(0.63 \pm 0.09) \times 10^{-10} \text{ m}^2 \cdot \text{s}^{-1}$.

Although it is difficult to model accurately the conformation of these polymer chains, however, we can still obtain an idea of their size by making the same assumption described above and applying Equation 2-8 again. The resulting R_H s are 0.82 , 1.37 ± 0.18 , 1.91 ± 0.19 and 3.91 ± 0.07 nm for fluorescein, PE-CO₂, PPE-PEG-^dCO₂, and PPE-PEG-^dCO-DNA, respectively.

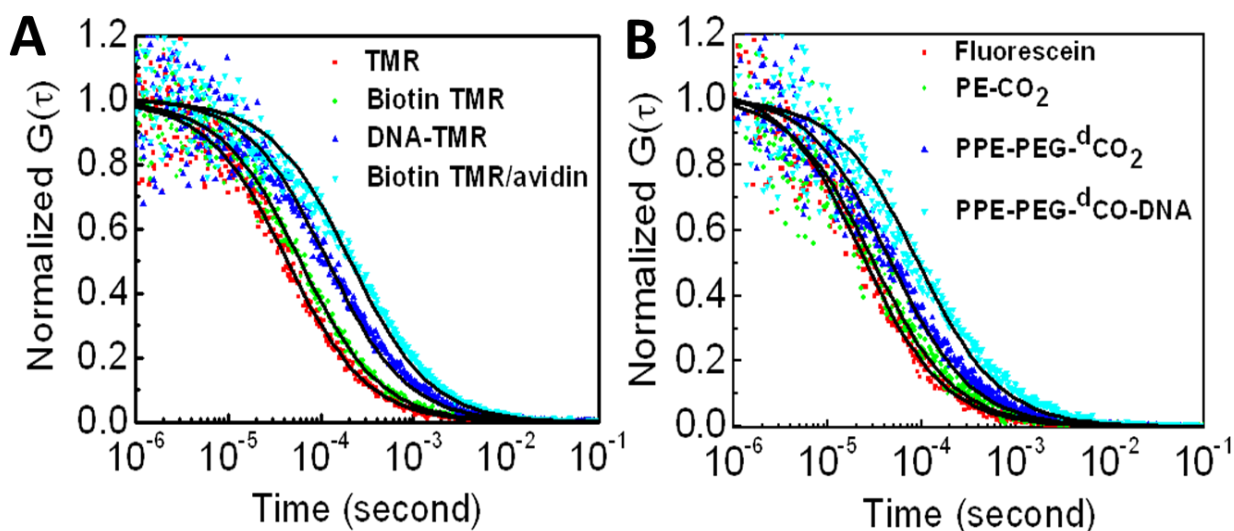


Figure 2-16. Effect of molecular weight (MW) on the correlation curves of molecules A) using 590 nm emission filter, B) using 500 nm emission filter. The black solid lines are the single species fitting curves.

A plot of diffusion coefficient versus molecular weight is displayed in Figure 2-17. A simple fitting model (red line) indicates an approximately inverse cubic root relationship between the diffusion coefficient (D) and the molecular weight (MW),

$$D = 18.19 \times MW^{-0.3} \quad (2-13)$$

When compared to Equation 2-11, the difference in the power value (-0.30 vs -0.33) is resulted from a rough assumption of spherical shape we made for the rigid-rod polymer. However, the results here are still consistent with the former conclusion—a higher molecular weight and larger particle size lead to longer diffusion time. Since the testing

results for the FCS system with 405 nm blue laser are reasonable, this instrument is reliable to be used in the following projects.

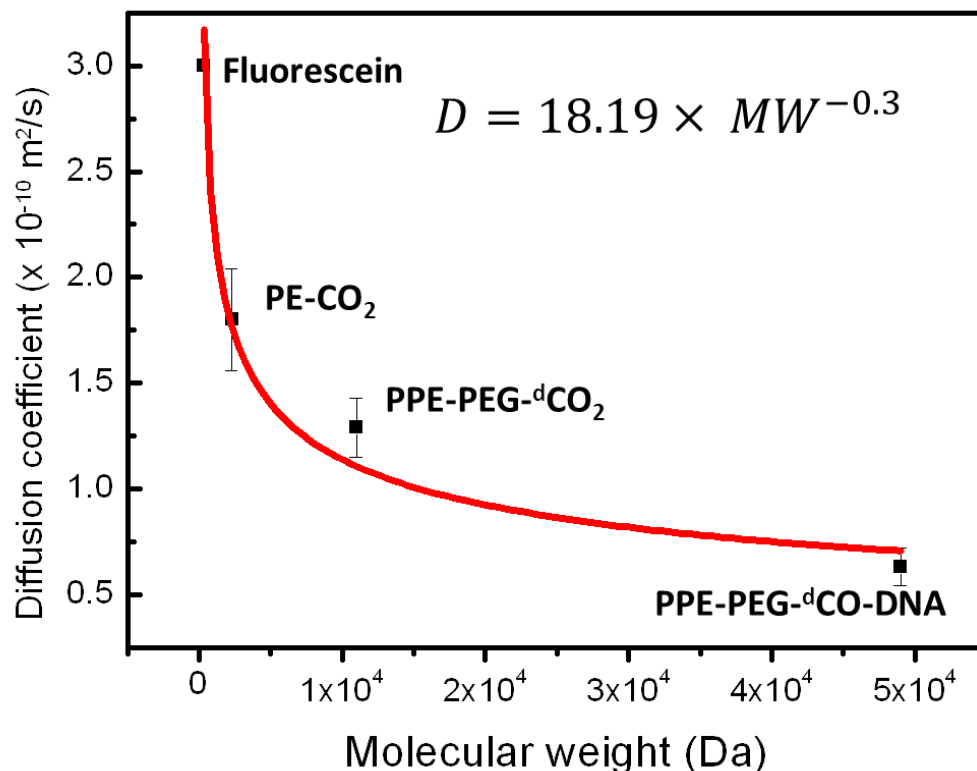


Figure 2-17. Plot of diffusion coefficient of four standard samples as a function of their molecular weight (emission filter 500 nm). Red line is the fitting curve.

Summary

An FCS with 405 nm laser as light source has been successfully constructed and the details about the alignment, optimization and calibration of the setup are provided. The examination of the newly built FCS setup further proved the feasibility of this instrument. By coupling with 405 nm laser, the application of FCS is successfully extended to the shorter wavelength region. With assistance from FCS, more insight and information regarding the CPEs properties from a microscopic motion aspect can be obtained, which is not supposed to be achieved via conventional technologies.

Materials and Methods

Materials

Oligomer PE-CO₂¹⁸¹ and PPE-PEG-dCO₂^{182, 183} were synthesized and prepared according to the reported procedures. PPE-PEG-dCO₂ was conjugated with ssDNA with sequence 5'-A10CCCAATCACTAA-3'(Invitrogen) to form PPE-PEG-dCO-DNA, using the synthesis method in the literature.¹⁸⁴ The loading ratio was ~5 ssDNAs per polymer chain. Molecular weights of oligomer PE-CO₂, PPE-PEG-dCO₂, and PPE-PEG-dCO-DNA are ca. 2,300, 11,000, and 49,000 Da, respectively. Tetramethylrhodamine (TMR) was purchased from AnaSpec, Inc. Fluorescein was purchased from Fisher. Biotin-TMR (5-(and-6)-Tetramethylrhodamine biocytin) was purchased from Invitrogen TM. Avidin was purchased from Sigma. DNA-TMR was prepared according to the literature.¹⁸⁵ All sample solutions were prepared using water distilled and purified by a Millipore purification system (Millipore Simplicity Ultrapure Water System). Buffer solutions were prepared with reagent-grade materials (Fisher). All polymer concentrations are reported as the polymer repeat unit concentration (PRU). Concentrated stock solutions of biotin-TMR and avidin were prepared in 10 mM phosphate buffer (pH 7) to obtain the desired concentrations. Fluorescein was prepared in 10 mM phosphate buffer (pH 8).

FCS Component and Measurement.

The measurements were performed in the setup constructed in house (Figure 2-6). The Olympus IX70 epi-fluorescence microscope platform and objective lens (60 \times , NA 1.2, water immersion) were purchased from Olympus. The 405 nm diode laser (CUBE) was purchased from Coherent. The 405 nm single mode fiber, 50 μ m-inner diameter multi-mode optical fiber, spatial filter system (KT110), fiberport collimator, 500 \pm 20 nm and 590 \pm 20 nm band-pass filter, and XYZ stage were purchased from

Thorlabs. The dichroic mirror cube was purchased from Chroma. The avalanche photodiode (APD, SPCM-AQR-14-FC) was purchased from Perkin Elmer. The chambered coverglass (Thermo Scientific, Nunc, Lab-Tek) was purchased from Fisher. The correlator (Flex02-12D) was purchased from correlator.com.

CHAPTER 3

THE APPLICATION OF DYE-LIGAND INTERCALATED HELICAL CONJUGATED POLYELECTROLYTE ON PROTEIN SENSING

Background

In previous work reported by our group, we have demonstrated from an optical spectroscopic study that a *meta*-linked poly(phenylene ethynylene) (Poly-1, Figure 3-1) can self-assemble into a helical conformation stabilized by the π - π stacking interactions between the phenyl rings with the ionic side chains extending to the surrounding polar solvent.²³ Due to the structural similarity between Poly-1 and double stranded DNA (dsDNA) (e.g., the π - π stacking helical backbone is analogous to π -stacked base in dsDNA; while the negatively charged side chains resemble the phosphate groups in dsDNA), some DNA intercalators featuring planar aromatic structures, exhibit identical spectroscopic effects upon binding to Poly-1 as they intercalate to dsDNA.¹⁸⁶⁻¹⁸⁸ For example, mixing $\text{Ru}(\text{bpy})_2(\text{dppz})^{2+}$ with Poly-1 leads to large enhancement of the luminescence from the Ru complex metal-to-ligand charge transfer state. The phenomenon is similar to that of intercalation of the Ru-dppz ligand into the double helix in dsDNA.¹⁸⁷

Avidin, a protein obtained from egg white, is toxic to many organisms due to its ability to deplete biotin, an essential vitamin (Vitamin H), from their environments.¹⁸⁹ The binding between avidin and biotin is extraordinarily stable and essentially irreversible.¹⁸⁹ This association has been exploited as a versatile tool for broad applications in biochemistry,^{190, 191} including enzyme linked immunosorbent assay (ELISA),^{192, 193} cell-surface labeling,¹⁹⁴ and affinity purification.¹⁹⁵

This chapter focuses on the interaction between helical Poly-1 and a dye-ligand compound, biotin-TMR (biotinylated rhodamine, 5-(and-6)-tetramethylrhodamine biocytin, Figure 3-1) as well as the influence on their interaction brought by avidin. The fluorescence resonance energy transfer (FRET) is observed when biotin-TMR and Poly-1 are mixed together, and it is not interrupted when avidin is present. However, when a pre-formed avidin/biotin-TMR is added into the Poly-1 buffer solution, disruption of energy transfer is observed, which gives rise to a novel FRET sensor for avidin with a detection limit for avidin of 100 pM. Interestingly, a systematic investigation on the fluorescence spectra of Poly-1 mixed with pre-formed avidin/biotin-TMR at various [avidin]:[biotin] ratios reveals the so-called *phenomenon steric constraint*. An FCS with a 543 nm laser, which typically excites TMR, is assisted to investigate the system. The intercalation of TMR to Poly-1 and the formation of supramolecular aggregates by Poly-1/biotin-TMR in the presence of avidin are demonstrated. The formation of aggregates also has been evidenced by atomic force microscopy (AFM), which well explains why the direct addition of avidin to polymer/biotin-TMR solution cannot interrupt the FRET. Another new avidin sensor is proposed based on the FCS curve changes with sensitivity < 100 pM.

Results and Discussion

FRET Study of Helical CPE/dye-ligand with Protein

Photophysical properties of Poly-1 and biotin-TMR

As shown in Figure 3-2, in aqueous phosphate buffer, Poly-1 absorbs in the near-UV (323 nm) and it exhibits a broad, structure-less emission band with λ_{\max} ~450 nm, which arises due to π - π interactions between the phenylene-ethynylene units that are in close proximity in the helix. The TMR chromophore in biotin-TMR absorbs at λ_{\max} ~554

nm (more photophysical data are summarized in Table 3-1). The emission of Poly-1 and absorption of biotin-TMR overlap well as shown in Figure 3-1, satisfying the prerequisite for FRET. The electrostatic attraction, as well as the hydrophobic interactions between anionic Poly-1 and net positively charged biotin-TMR, brings these two potential donor and acceptor in close proximity, typically < 0.1 nm, where FRET is permitted.³⁵

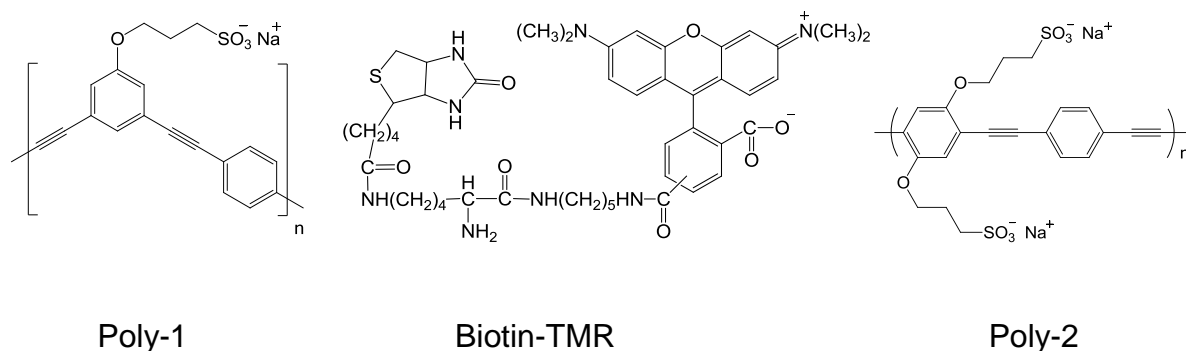


Figure 3-1. Structure of polymers and dye-ligand compound.

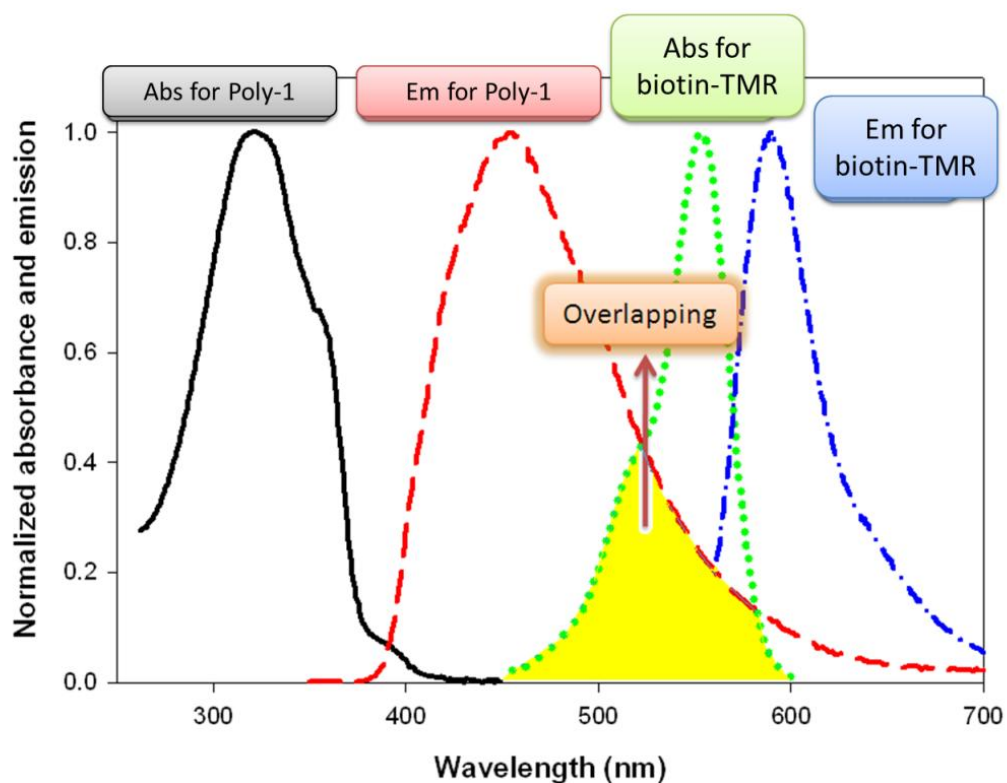


Figure 3-2. Absorption (Abs) and emission (Em) spectra of Poly-1 and biotin-TMR.

Table 3-1. Photophysical properties of TMR, Poly-1, and biotin-TMR in 10 mM phosphate buffer solution (pH 7.4). Reprinted with permission from Wu, D. L., *et al.*¹⁷⁶

	λ_{abs}^{max} (nm)	λ_{em}^{max} (nm)	ϵ ($\times 10^4 \text{ M}^{-1} \cdot \text{cm}^{-1}$)
TMR	548	575	8.39 ± 0.03
Poly-1	323	450	3.29 ± 0.07
Biotin-TMR	554	580	7.04 ± 0.12

FRET from Poly-1 to TMR

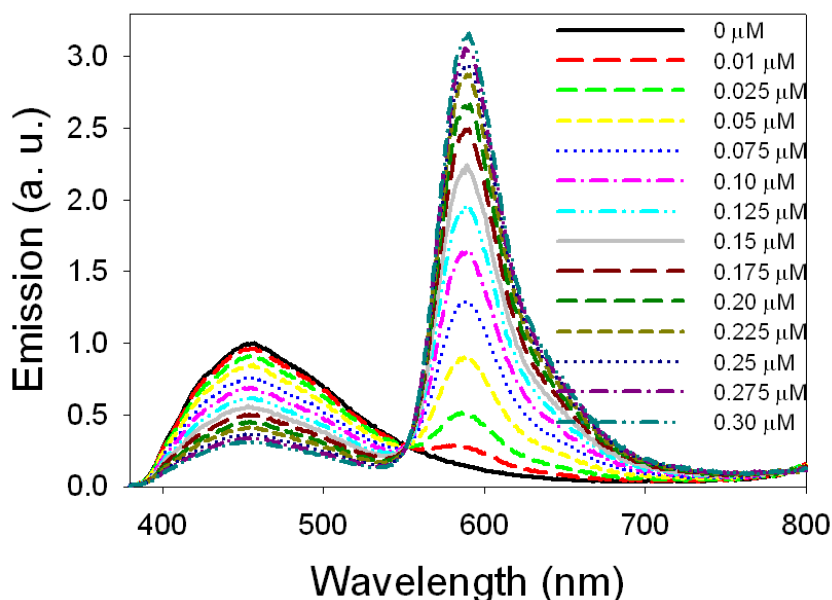


Figure 3-3. Normalized emission spectra for titration of 0-0.3 μM biotin-TMR into 15 μM Poly-1 in 1 mM phosphate buffer solution, pH = 7.4.

Figure 3-3 illustrates the changes in fluorescence when various concentrations of biotin-TMR are titrated to an aqueous buffer solution of 15 μM Poly-1. The fluorescence of Poly-1 at 450 nm is quenched, and a strong emission band from TMR appears at $\lambda_{\text{max}} \sim 590 \text{ nm}$. Importantly, under the same excitation conditions, the fluorescence from biotin-TMR alone is very weak (Figure 3-4), indicating that the FRET takes place from Poly-1 to TMR. Fluorescence anisotropy spectra (Figure 3-5), used to characterize the molecular motion via emission polarity, show that in the presence of polymer, the rotational motion of biotin-TMR is restricted in a certain orientation with anisotropy

values varying from -0.05 to 0.15, indicating the biotin-TMR locates in a confined area, presumably the helix of Poly-1, where depolarization is difficult to occur.

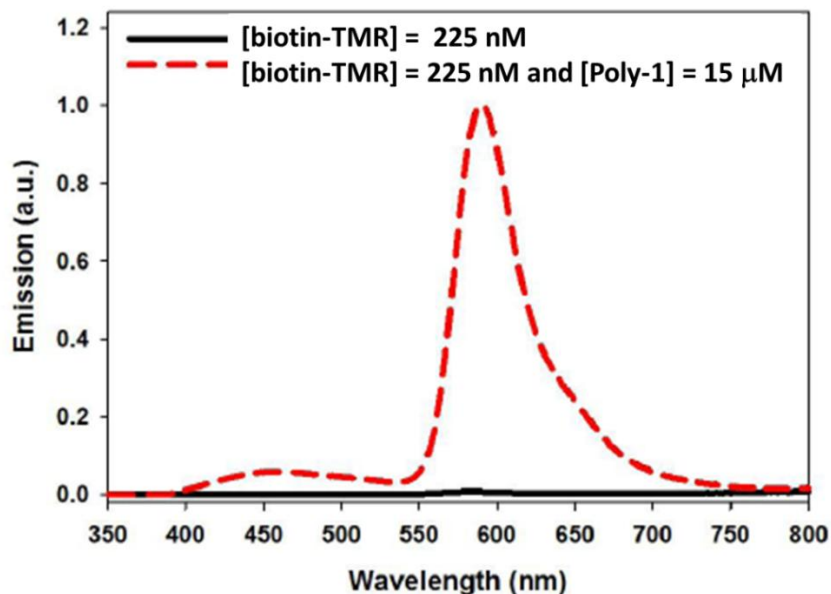


Figure 3-4. Normalized fluorescence spectra ($\lambda_{\text{ex}} = 320 \text{ nm}$) of biotin-TMR (225 nM) in the absence (—) and presence (---) of Poly-1 (15 μM) in aqueous phosphate buffer. Reprinted with permission from Ji. E., *et al.*³⁰

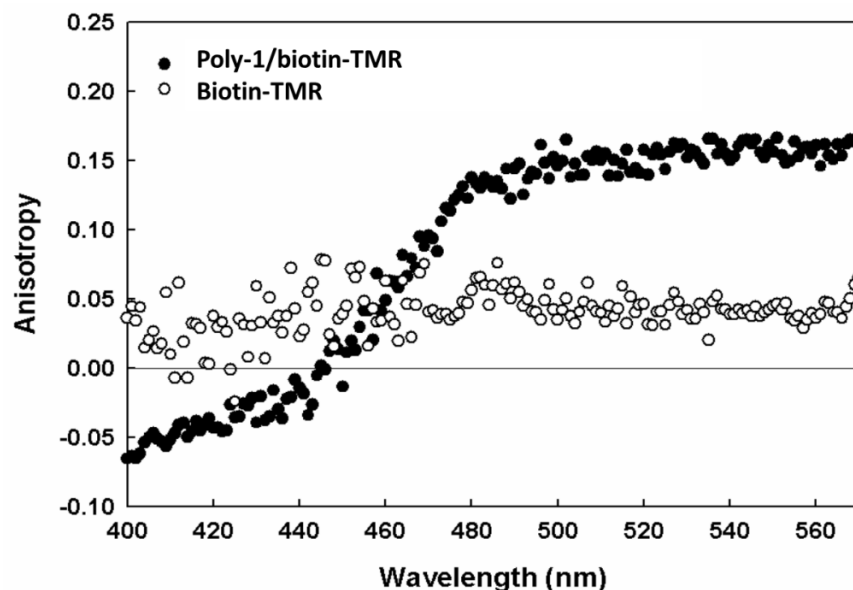


Figure 3-5. Fluorescence anisotropy spectra for biotin-TMR with and without Poly-1. Reprinted with permission from Ji. E.¹⁹⁶

Addition of avidin to Poly-1/biotin-TMR

As reported by Whitten and co-workers, in a PPV/MV²⁺-biotin quenching system ([PPV] = 1.7×10^{-5} M, [MV²⁺-biotin] = 2×10^{-6} M), the addition of only 2×10^{-7} M avidin can restore the fluorescence of PPV by 50%, due to the interruption on the charge transfer path from exciton to quencher.⁴³ So in this section, the influence avidin brings to the Poly-1/biotin-TMR system, especially to the FRET process, is under investigation. In Figure 3-3, as the [biotin-TMR] reaches 0.30 μ M, the FRET effect is approaching saturation. So here, the solution of Poly-1/biotin-TMR with [Poly-1] = 15 μ M and [biotin-TMR] = 0.225 μ M is used for avidin titration. As shown in Figure 3-6, the fluorescence of biotin-TMR is slightly quenched by avidin; however, recovery of Poly-1 fluorescence does not occur. This result suggests that avidin is unable to disrupt the FRET from Poly-1 to TMR, indicating that the rhodamine chromophore remains highly interacting with, possibly intercalating into Poly-1.

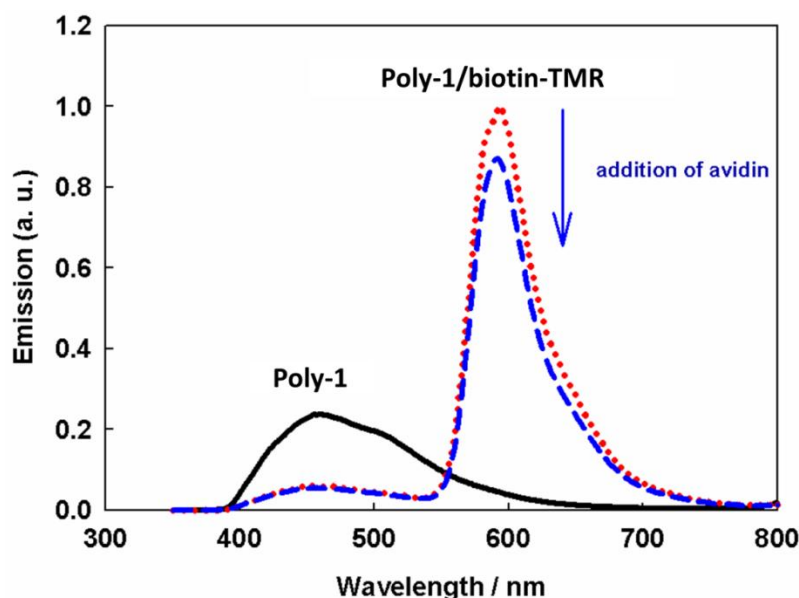


Figure 3-6. Fluorescence spectra of Poly-1 solution (—) upon addition of biotin-TMR (•••) and avidin (---). [Poly-1] = 15 μ M, [biotin-TMR] = 0.225 μ M and [avidin] = 0.065 μ M. λ_{ex} = 320 nm. Reprinted with permission from Ji. E.¹⁹⁶

Titration of preformed avidin/biotin-TMR to Poly-1

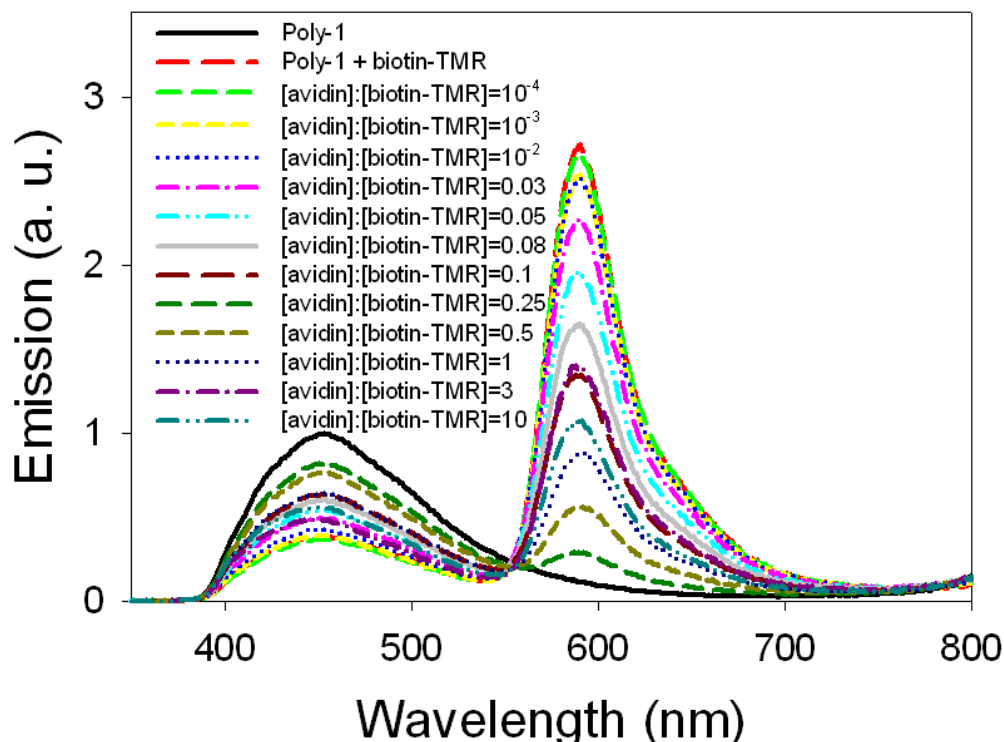


Figure 3-7. Normalized emission spectra for Poly-1 mixed with preformed avidin/biotin-TMR at various $[avidin]:[biotin-TMR]$. $[Poly-1] = 15 \mu M$, $[biotin-TMR] = 225 \text{ nM}$. Titration is done in 1 mM phosphate buffer solution, pH 7.4, room temperature.

By contrast, a discontinuous titration of pre-mixed avidin/biotin-TMR to the polymer solution was conducted. Initially, various amounts of avidin were mixed with identical amount of biotin-TMR in vials. After ~ 10 min incubation, the mixtures were added into 15 μM Poly-1 individually with final $[biotin-TMR]$ fixed at 0.225 μM . Figure 3-7 shows the emission spectra of Poly-1 solutions with varying $[avidin]:[biotin-TMR]$ in the range of 0-10. Interestingly, as $[avidin]:[biotin-TMR]$ increases, the emission of TMR first reduces gradually, followed by an increase, and then decreases again. A similar trend in spectra change occurs with 5 μM Poly-1 mixed with pre-formed avidin/biotin-TMR (final $[biotin-TMR] = 100 \text{ nM}$). The emission spectra are converted to a graph where the ratio of the fluorescence intensity at 590 nm and 450 nm (I_{590}/I_{450}) is plotted as a function of log

[avidin] (Figure 3-8). Impressively, the minimum FRET occurs at $[\text{avidin}]/[\text{biotin}] = 0.25$ for both systems with different polymer concentration, indicating that the 1:4 avidin-biotin-TMR complex is least able to interact with and undergo FRET from Poly-1. This ratio value corresponds to the four binding sites on avidin for biotin,¹⁸⁹ revealing the fact that steric constraints may prevent intercalation of the avidin bound biotin-TMR to Poly-1.

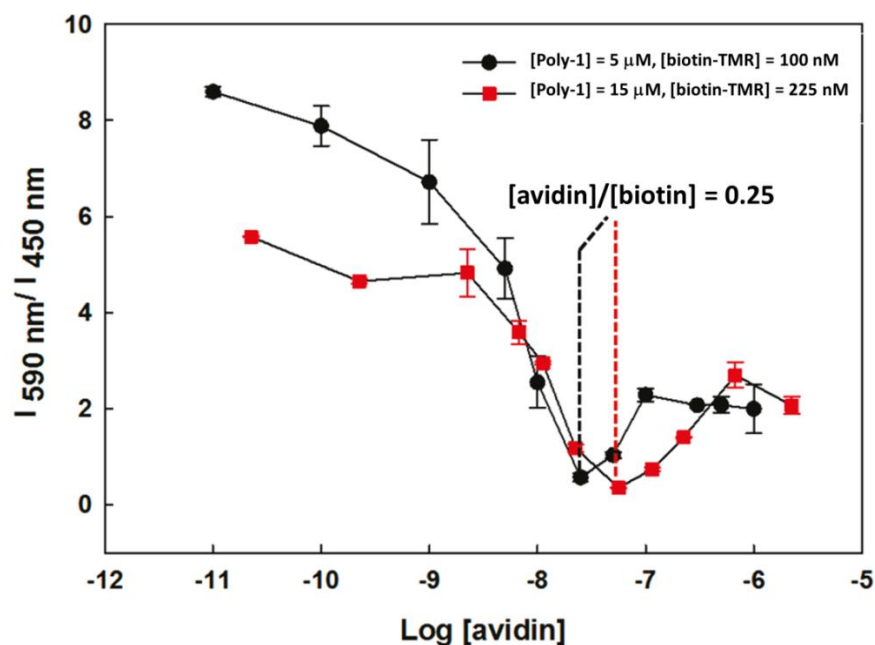


Figure 3-8. Ratio of intensities at 590 nm and 450 nm after addition of pre-mixed biotin-avidin complex at various avidin concentrations in phosphate buffer (1 mM, pH 7.4), $\lambda_{\text{ex}} = 320$ nm. For $[\text{biotin-TMR}] = 100$ nM, the analytical detection limit of avidin is 100 pM. Reprinted with permission from Ji, E., *et al.*³⁰

Figure 3-9 illustrates the possible mechanism for the complicated dependence of FRET on the $[\text{avidin}]/[\text{biotin-TMR}]$ ratio. First, for $[\text{avidin}]/[\text{biotin-TMR}] < 0.25$, there are not enough binding sites for biotin in avidin, so excess biotin-TMRs are able to intercalate to Poly-1, maintaining partial FRET response. Increase in $[\text{avidin}]$ decreases the available biotin-TMR, thus the FRET events are reduced to a minimum. However, when $[\text{avidin}]/[\text{biotin-TMR}] > 0.25$, all of the biotin is bound to avidin, but because the

protein is in excess, the avidin/biotin-TMR complexes appears with less than four biotin-TMR binding ligands. A less bulky avidin/biotin-TMR complex may be able to more effectively interact with Poly-1, perhaps allowing intercalation of the TMR chromophore, thus slightly recovering the FRET signal.

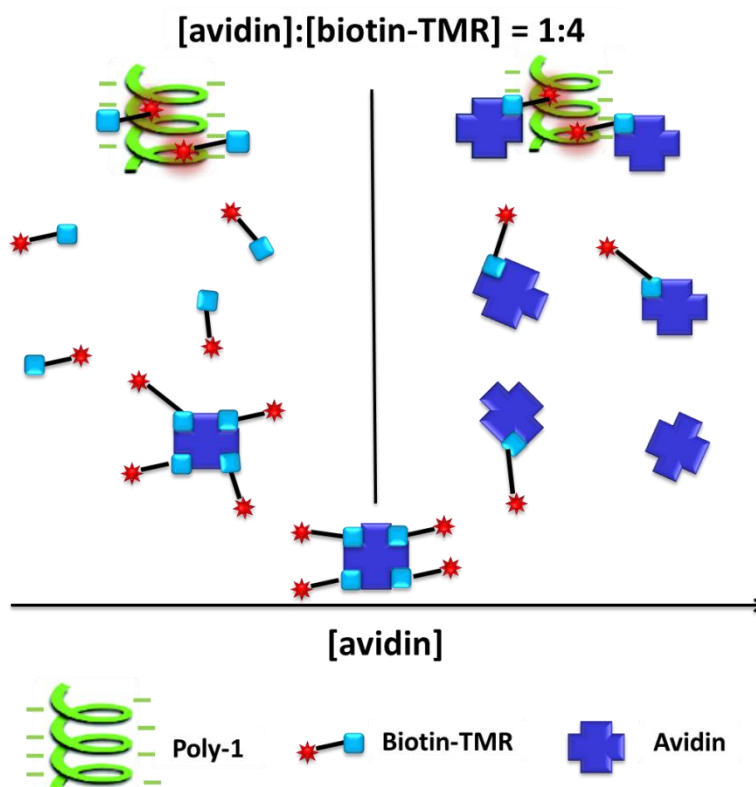


Figure 3-9. Binding of preformed avidin/biotin-TMR complex to Poly-1 as a function of added avidin concentration. Reprinted with permission from Ji, E., *et al.*³⁰

FCS Study on the Poly-1/biotin-TMR/avidin System

In order to obtain more details and insights about this system, we employed FCS in the study. The FCS system we used in this work was built by the Dr. Weihong Tan's group at the University of Florida, Department of Chemistry (Figure 3-10). The system couples with a 543 nm green laser, which excites the TMR dye. In this section, all of the FCS measurements are focusing on the diffusion behavior of biotin-TMR and its complex. Although Poly-1 doesn't have absorbance around 543 nm (Figure 3-2) and

FCS correlation signal (Figure 3-11B), it can be a “host” or “carrier” for the dye molecules, so that any diffusion behavior change of the polymer can be followed by monitoring the fluctuation of the TMR's fluorescence through FCS.

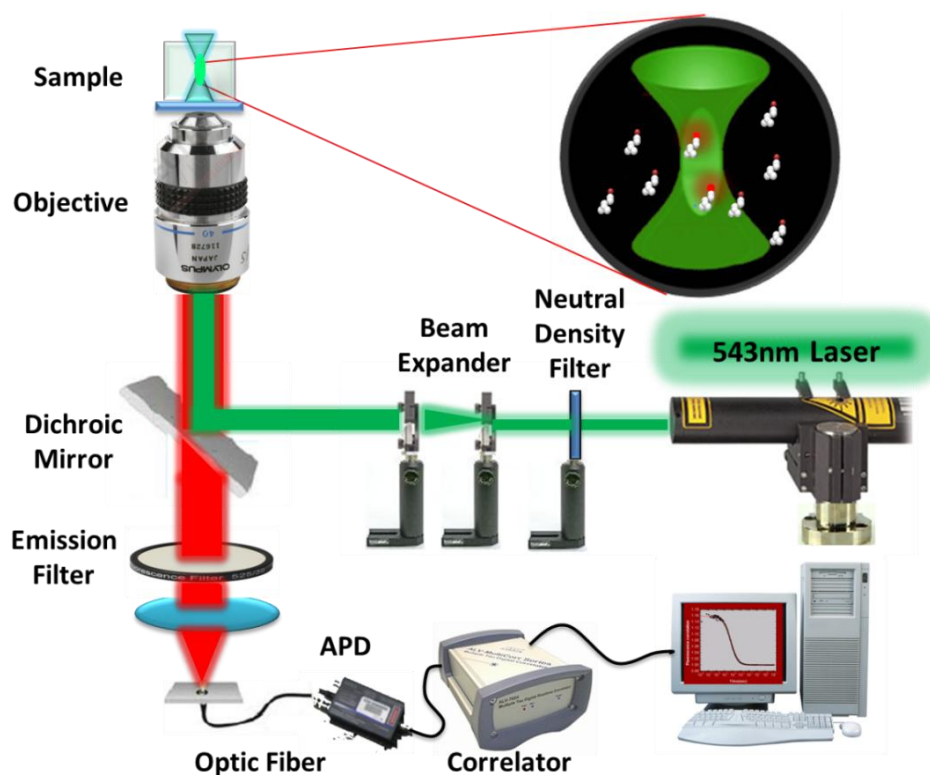


Figure 3-10. Basic setup for FCS with 543 nm Laser.

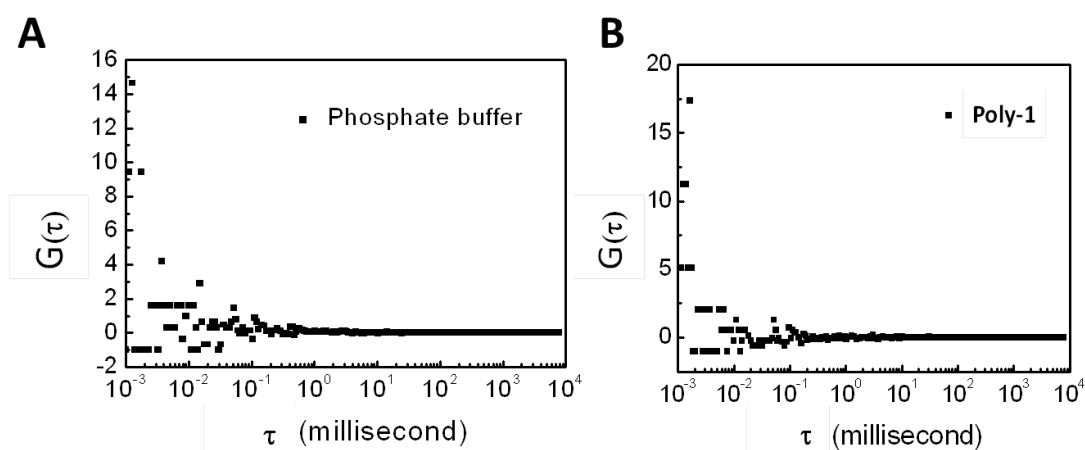


Figure 3-11. Background detection for A) phosphate buffer (10 mM, pH 7.4) B) Poly-1 (1 μ M) in phosphate buffer (10 mM, pH 7.4). Reprinted with permission from Wu, D. L., *et al.*¹⁷⁶

Diffusion behavior of four types of molecules/complex

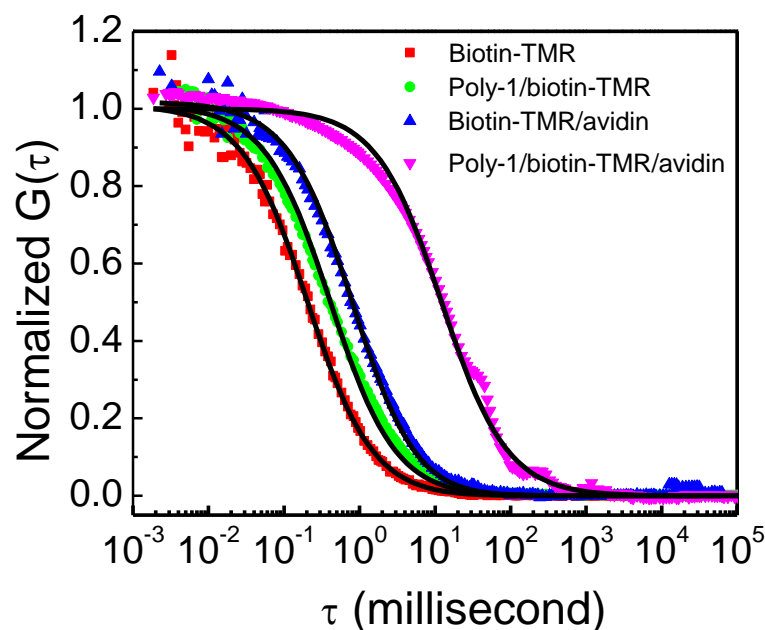


Figure 3-12. Normalized correlation functions of biotin-TMR, Poly-1/biotin-TMR, biotin-TMR/avidin, and Poly-1/biotin-TMR/avidin with $[\text{avidin}]/[\text{biotin-TMR}] = 0.25$ in phosphate buffer solution (10 mM, pH 7.4). The black solid lines are single species fitting curves. Reprinted with permission from Wu, D. L., *et al.*¹⁷⁶

The diffusion time of aforementioned molecules and complex were first measured. Using ultracentrifugation, the Poly-1/biotin-TMR complex was prepared with a molecular weight between 30 kDa and 10 kDa. The FCS experimental results are displayed in Figure 3-12 and Table 3-2. Biotin-TMR mixed with Poly-1 (Poly-1/biotin-TMR) exhibits a significantly longer diffusion time (0.79 ms) compared to free biotin-TMR molecules (0.29 ms) in neutral buffer solution. In contrast, a *para*-linked poly(poly(phenylene ethynylene)) (Poly-2, Figure 3-1), which features a similar repeat unit structure as Poly-1, but adopts non-helical in buffer solution, was mixed with biotin-TMR in a control experiment. The diffusion time for Poly-2/biotin-TMR (0.27 ms) is almost the same as the value observed for free dye molecules (0.29 ms) (Figure 3-13). The result clearly shows that the slower diffusion for Poly-1/biotin-TMR is caused by intercalative binding

instead of electrostatic attraction between Poly-1 and biotin-TMR. When biotin-TMR binds to a larger molecule of avidin (MW = 66 kDa) at a stoichiometric concentration, a longer diffusion time of 1.21 ms (Figure 3-12) is obtained.

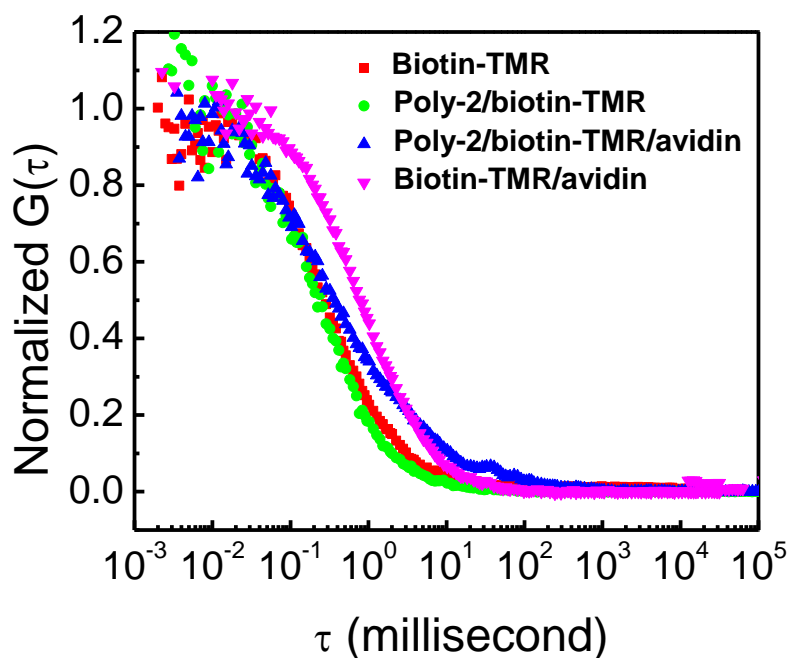


Figure 3-13. Normalized correlation functions of biotin-TMR, Poly-2/biotin-TMR, Poly-2/biotin-TMR/avidin and biotin-TMR/avidin with $[\text{avidin}]/[\text{biotin-TMR}] = 0.25$ in phosphate buffer (10 mM, pH 7.4). Reprinted with permission from Wu, D. L., *et al.*¹⁷⁶

Table 3-2. Diffusion data for four species in phosphate buffer (10 mM, pH 7.4). Reprinted with permission from Wu, D. L., *et al.*¹⁷⁶

Item	Biotin-TMR	Poly-1/biotin-TMR	Biotin-TMR/avidin ([avidin]/[biotin] = 0.25)	Poly-1/biotin-TMR/avidin ([avidin]/[biotin] = 0.25)
Diffusion time τ_D (ms)	0.29 ± 0.02	0.79 ± 0.08	1.21 ± 0.20	11.50 ± 3.40
Diffusion coefficient D ($\times 10^{-10}$ m ² /s)	1.67 ± 0.14	0.61 ± 0.07	0.39 ± 0.08	0.0371 ± 0.0164
Estimated MW (kDa)	0.869	10.0 - 30.0	69.6	NA
Calculated MW (kDa)	0.869	18.2 ± 3.2	66.3 ± 14.8	$(79.3 \pm 15.2) \times 10^3$

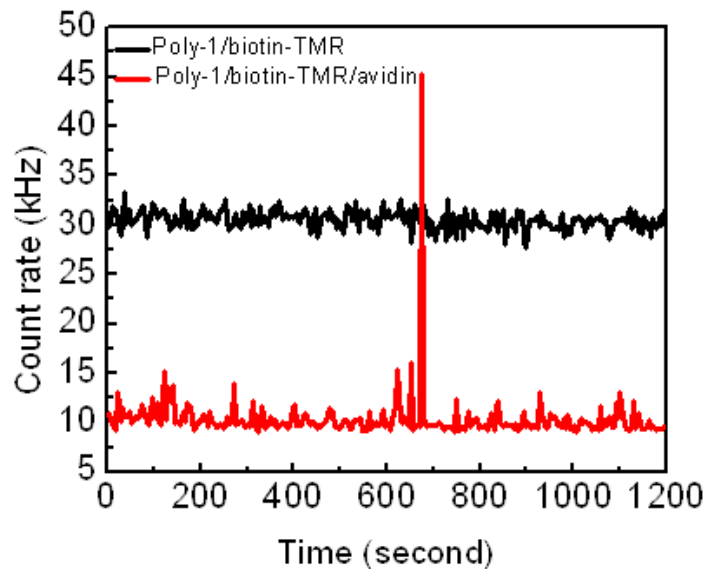


Figure 3-14. Photon counting rate (fluorescence fluctuation) during the detection time (1200 s) for Poly-1/biotin-TMR and Poly-1/biotin-TMR/avidin ([avidin]/[biotin-TMR] = 0.25) in phosphate buffer (10 mM, pH 7.4). Reprinted with permission from Wu, D. L., *et al.*¹⁷⁶

The diffusion coefficient (D) scales approximately as the inverse of the cube root of the molecular weight (MW).³⁵ Due to the inversion relationship between diffusion time (τ_D) and D (Equation 2-4), we have

$$\left(\frac{\tau_{D1}}{\tau_{D2}}\right)^3 \approx \frac{MW_1}{MW_2} \quad (3-1)$$

The approximate cube root dependence of the τ_D on MW provides a way to roughly estimate the molecular weight of each species. The FCS-based calculation results displayed in Table 3-2 are consistent to the values estimated on the basis of their chemical structure. A significantly longer diffusion time is observed for Poly-1/biotin-TMR in the presence of the avidin with [avidin]/[biotin-TMR] = 0.25, suggesting the formation of very large aggregates. The fluorescence time trajectory (count rate) of Poly-1/biotin-TMR/avidin shows pronounced spikes on a lower baseline (Figure 3-14), which are attributed to the large particles formed by the protein and polymer, passing through the excitation volume at a slow rate. It must be noted that the large molecular

weight $(79.3 \pm 15.2) \times 10^3$ kDa calculated for the diffusing particle based on Equation 3-1 is only a rough estimation due to complex structure and size heterogeneity of the large aggregates. However, it still can be evidence for the large size of the aggregation, in clear contrast with the much smaller molecular weight of the Poly-1/biotin-TMR complex in the absence of avidin.

Mechanism for formation of supramolecular aggregation

The possible mechanism for this phenomenon is illustrated in Figure 3-15. In aqueous solution, more than one biotin-TMR binds to helical Poly-1 by intercalation of TMR, extending the biotin portions towards surrounding solution and forming a “biotin-functionalized” complex. Then the avidin possessing four biotin binding sites, is added into the system simultaneously crosslinking those “biotinylated” complexes via avidin-biotin binding. The explanation for the cross-linked aggregates with avidin as the bridge, bears some analogy to the one reported by Sleiman and co-workers that the biotin-Ru-dppz intercalated dsDNAs are cross-linked through streptavidin-functionalized gold nanoparticles.¹⁹⁷

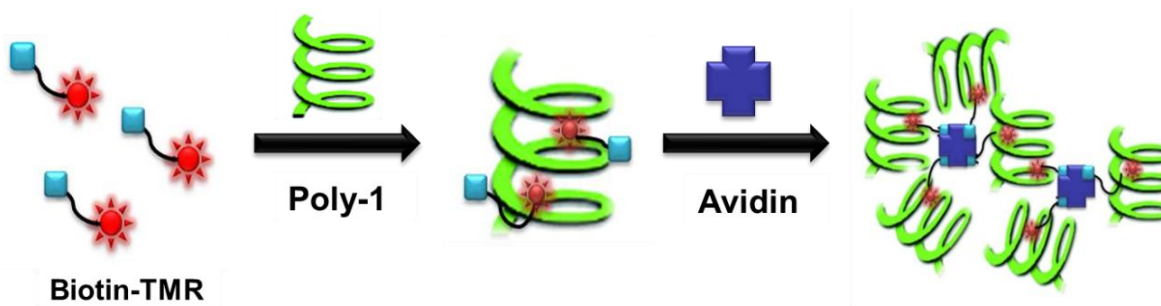


Figure 3-15. Proposed mechanism of protein-induced aggregation. Reprinted with permission from Wu, D. L., *et al.*¹⁷⁶

This interpretation of the findings is further corroborated by AFM images of dry films deposited from dilute solutions of Poly-1, Poly-1/biotin-TMR and Poly-1/biotin-TMR/avidin measured in air individually. As illustrated in Figure 3-16, deposited

particles for Poly-1 and Poly-1/biotin-TMR are well-spread out with comparatively small heights ~4 and 12 nm, respectively. In sharp contrast, the Poly-1/biotin-TMR/avidin produces much fewer and considerably larger particles (height ~200 nm) in a comparable area, which further suggests the formation of large aggregates.

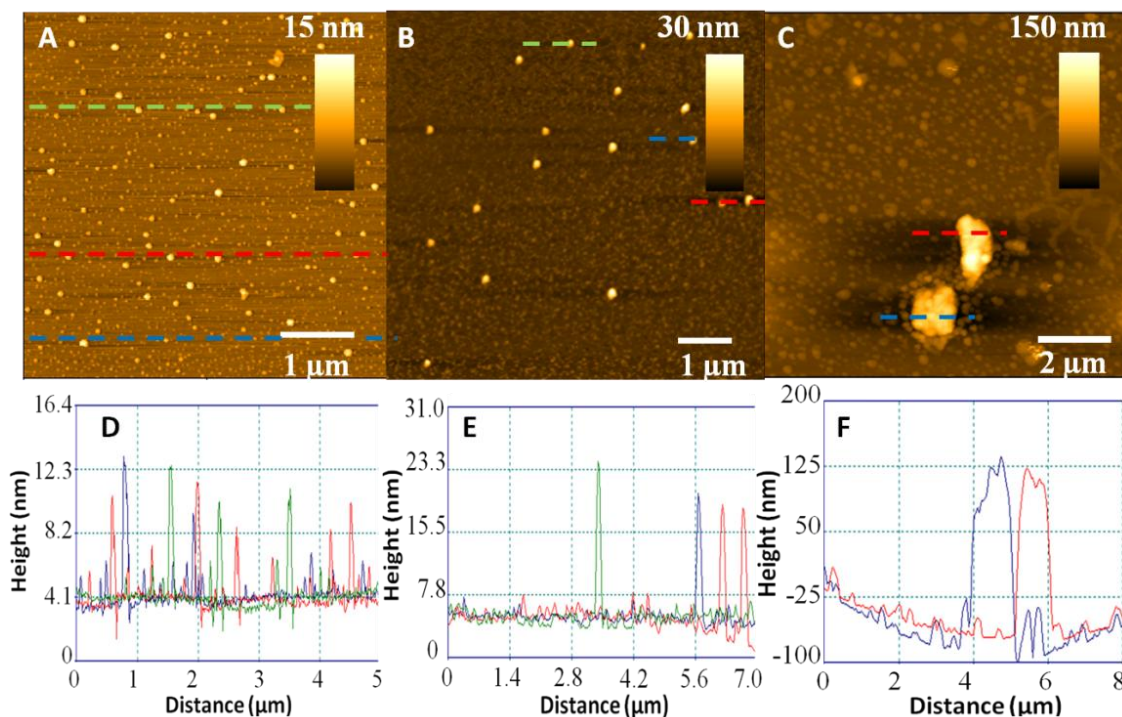


Figure 3-16. AFM images for A) pure Poly-1 B) Poly-1/biotin-TMR C) Poly-1/biotin-TMR/avidin ([avidin]/[biotin-TMR] = 0.25) Line scans for D) pure Poly-1 E) Poly-1/biotin-TMR F) Poly-1/biotin-TMR/avidin ([avidin]/[biotin-TMR] = 0.25). Different colors represent different particles. Reprinted with permission from Wu, D. L., *et al.*¹⁷⁶

Control experiment

Considering that avidin ($pI > 10$)¹⁸⁹ is positively charged in pH 7.4 buffer solution, a series of control experiments were conducted to detect the possible non-specific interaction between avidin and the anionic polymer. The first experiment was carried out on Poly-1/biotin-TMR with and without avidin in 10 mM pH 10.5 buffer, where avidin is overall negatively charged. A slightly shorter diffusion time (~0.69 ms) is observed for Poly-1/biotin-TMR. As discussed in the Chapter 1, due to the partial protonation of the

ionic side chains, CPE subjects to an aggregation behavior as pH decreases from 12 to 7. So here, the shorter diffusion time presumably corresponds to the smaller Poly-1/biotin-TMR complex resulting from the de-aggregation of Poly-1 in a higher pH solution. Nevertheless, a considerably larger diffusion time (~ 8.71 ms) is observed with addition of avidin, indicating the large supramolecular aggregate is still formed, regardless of the charge type of avidin (Figure 3-17).

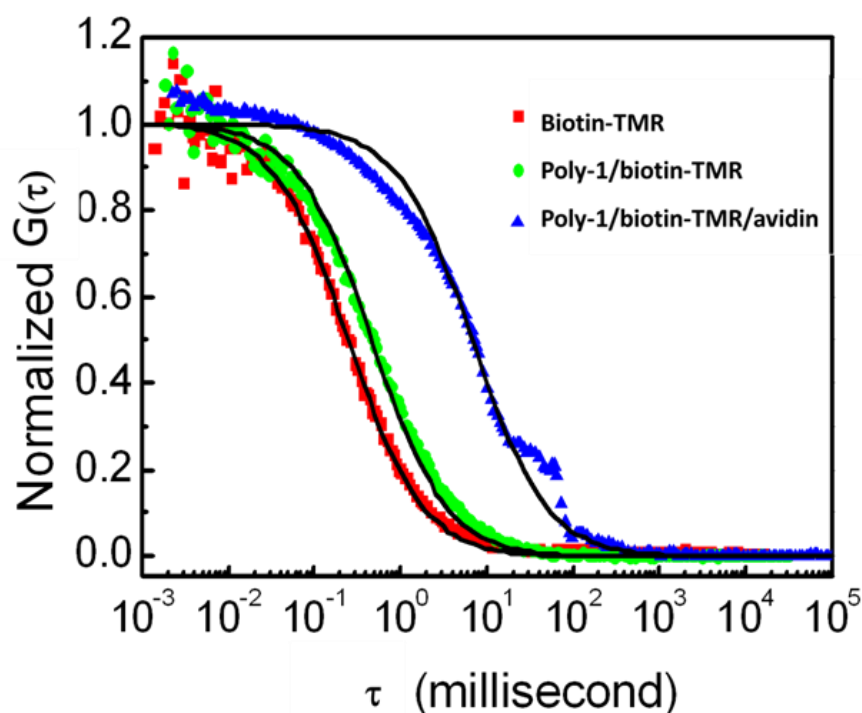


Figure 3-17. Normalized correlation functions of biotin-TMR, Poly-1/biotin-TMR, and Poly-1/biotin-TMR/avidin with $[\text{avidin}]/[\text{biotin-TMR}] = 0.25$ in phosphate buffer solution (10 mM, pH 10.5). The black solid lines are single species fitting curves. Reprinted with permission from Wu, D. L., *et al.*¹⁷⁶

Further control experiments were carried out to test whether the biotin-avidin interaction is essential to the aggregation behavior of the complex. This was achieved by replacing biotin-TMR with TMR that is still able to intercalate into the Poly-1 but has no binding interaction with avidin (Figure 3-18). Parallel FCS experiments were conducted in both pH 7.4 (Figure 3-19A) and pH 10.5 (Figure 3-19B) solutions. Not

surprisingly, the addition of avidin to the two Poly-1/TMR assaying solutions does not cause a significant change in the FCS curves, except a slight increase in the diffusion time for the Poly-1/TMR/avidin in pH 7.4 buffer solution (~ 0.89 ms) (Figure 3-19A), which arises from non-specific interaction between the polymer and protein. However, the effect is negligible when compared to that of the binding between avidin and biotin. The AFM images of deposited Poly-1/avidin and Poly-1/TMR/avidin are shown in Figure 3-20. Consistent with FCS results, no large particles are observed. The conclusion can be derived from the above findings that the non-specific interaction between avidin and polymer is not strong enough to enable the formation of huge aggregations and cause the substantial change in diffusion time. Since the pH-dependent non-specific interactions are weak and negligible, additional work regarding the avidin assay was performed in buffers with pH 7.4.

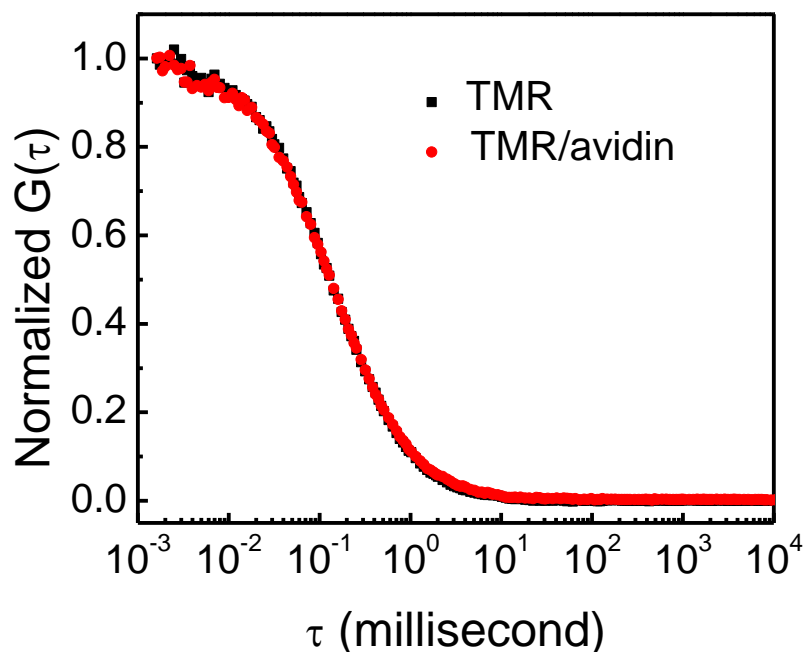


Figure 3-18. Normalized correlation functions for ligand-free TMR with and without avidin in 10 mM phosphate buffer. Reprinted with permission from Wu, D. L., *et al.*¹⁷⁶

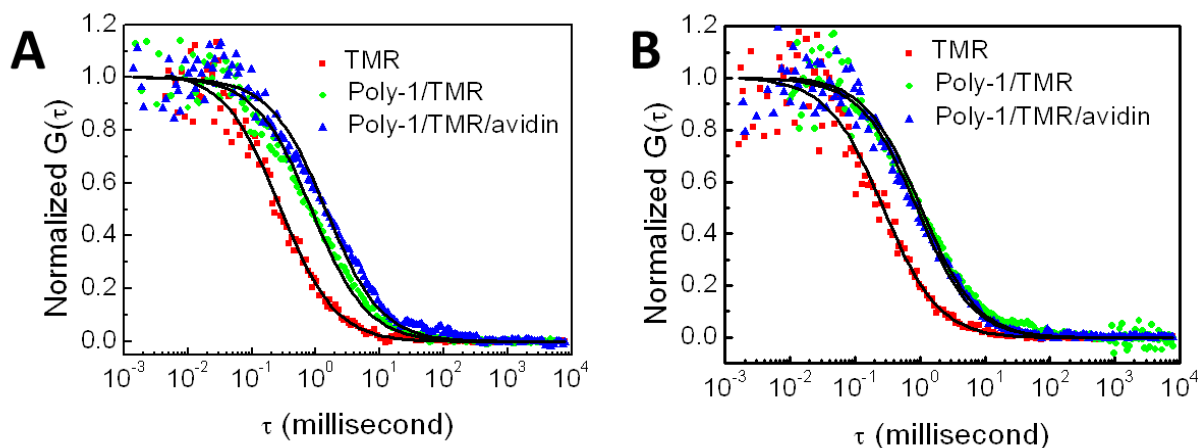


Figure 3-19. Normalized correlation curves for Poly-1/TMR and Poly-1/TMR/avidin in 10mM phosphate buffer A) pH 7.4 ([Poly-1] = 200 nM, [TMR] = 13.6 nM, [avidin] = 3.4 nM) B) pH 10.5 ([Poly-1] = 200 nM, [TMR] = 9.2 nM, [avidin] = 2.4 nM). Reprinted with permission from Wu, D. L., *et al.*¹⁷⁶

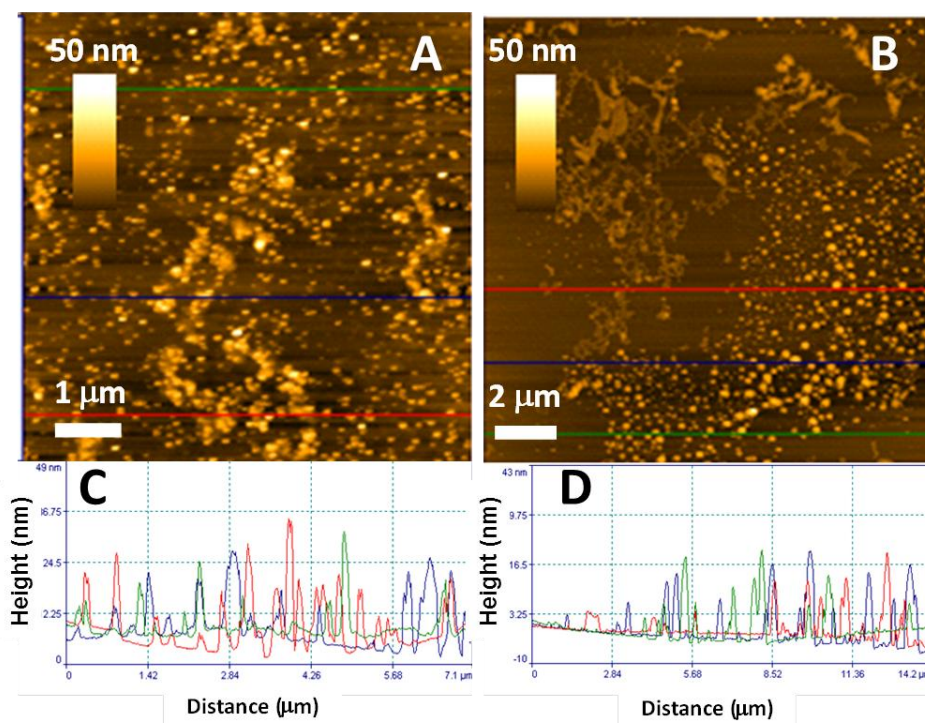


Figure 3-20. AFM images for A) Poly-1/avidin and B) Poly-1/TMR/avidin ([avidin]/[TMR] = 0.25). Line scans for C) Poly-1/avidin and D) Poly-1/TMR/avidin. Different colors represent different scans. Reprinted with permission from Wu, D. L., *et al.*¹⁷⁶

In a negative control experiment, the same amount of protein BSA ($pI = 4.7$ ³³), which has a similar molecular weight of 66 kDa with avidin but has no binding sites for

biotin was added into the Poly-1/biotin-TMR in pH 7.4 buffer. No significant change is observed in the FCS curves (Figure 3-21). All the findings shown above prove that the aggregation/crosslinking in Poly-1/biotin-TMR/avidin system is the result of the intercalation of TMR into the polymer and the binding between biotin and avidin.

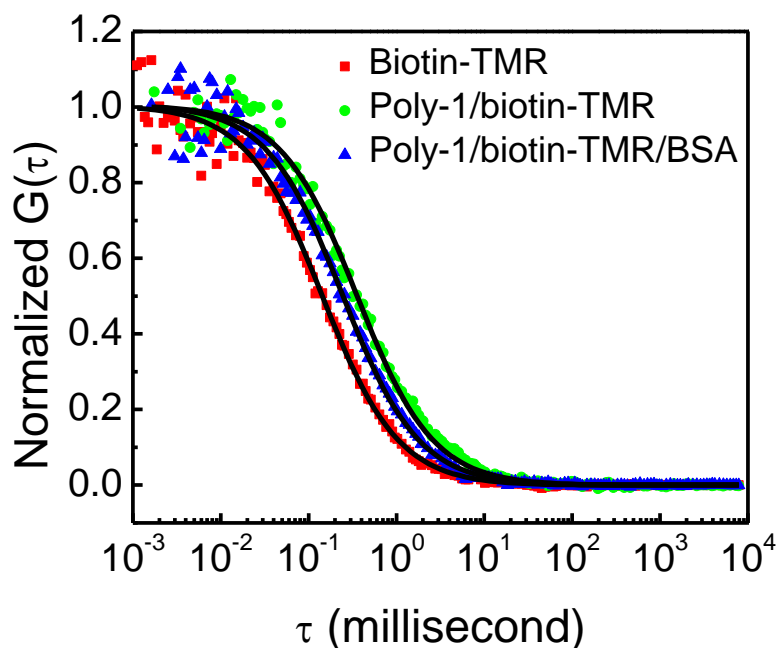


Figure 3-21. Normalized correlation functions for biotin-TMR, Poly-1/biotin-TMR and Poly-1/biotin-TMR/BSA with $[BSA]/[biotin-TMR] = 0.25$ in phosphate buffer (10 mM, pH 7.4). Black solid lines are single species fitting curves. Reprinted with permission from Wu, D. L., *et al.*¹⁷⁶

Avidin sensing strategy

The avidin-induced aggregation of Poly-1/biotin-TMR gives rise to the sensing strategy of avidin. Concentration-dependent experiments were performed by adding varying amounts of avidin into the Poly-1/biotin-TMR solution (Figure 3-22, $[Poly-1] = 102.8$ nM, $[biotin-TMR] = 7$ nM). When $[avidin]/[biotin-TMR]$ is lower than 0.1, no significant change in the diffusion time is observed. However, a noticeable distortion in the correlation curve is observed when $[avidin]/[biotin-TMR]$ reaches 0.1. As $[avidin]/[biotin-TMR]$ increasing from 0.1 to 100, the correlation curves shift largely to a

longer diffusion time. Only at a ratio of 0.25, the well-defined correlation function is obtained, indicating a relatively homogeneous distribution in the size of aggregation, possibly due to the 4:1 stoichiometry between biotin and avidin. For other ratios, especially at higher [avidin]/[biotin-TMR], the correlation curves become complicated, and cannot be simply fit by Equation 2-2, suggesting an inhomogeneous distribution of the aggregate size.

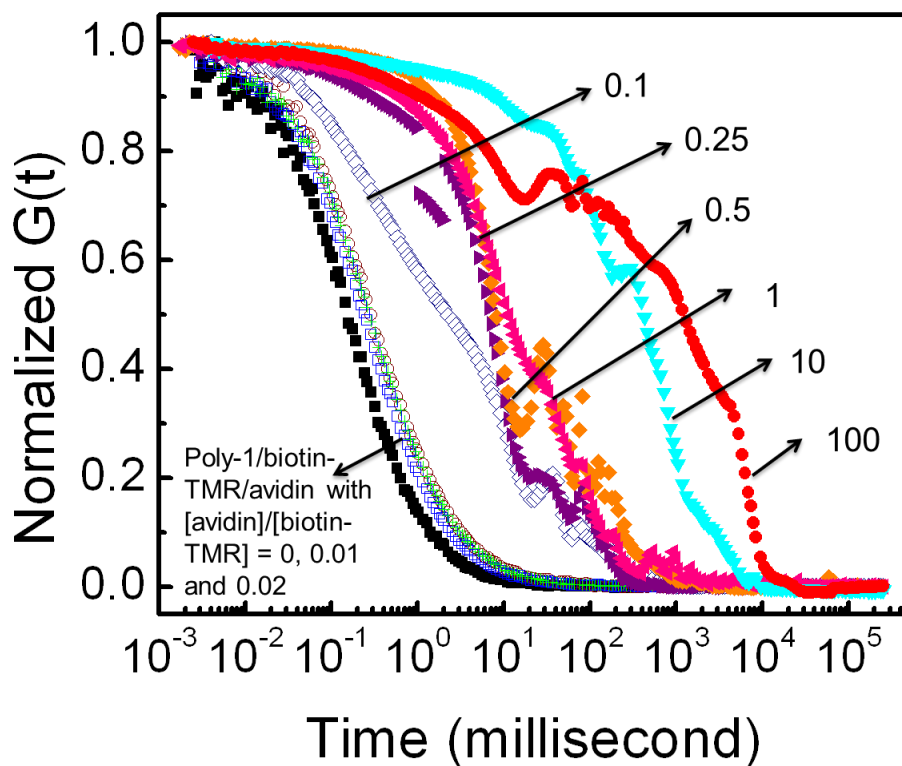


Figure 3-22. Normalized correlation functions for biotin-TMR (■), Poly-1/biotin-TMR (○), and Poly-1/biotin-TMR/avidin with [avidin]/[biotin-TMR] equal to 0.01 (□), 0.02 (+), 0.1 (◇), 0.25 (▴), 0.5 (◆), 1 (◀), 10 (▾) and 100 (●) in phosphate buffer (10 mM, pH 7.4). Reprinted with permission from Wu, D. L., *et al.*¹⁷⁶

Based on the analysis above, for our system, the critical [avidin]/[biotin-TMR] when avidin is detectable is 0.1. A Poly-1/biotin-TMR complex with [Poly-1] = 14.68 nM and [biotin-TMR] = 1 nM was further detected in the presence of 100 pM avidin. A correlation curve for Poly-1/TMR/avidin with the same concentration of Poly-1 and

avidin was also recorded for monitoring the non-specific interaction between Poly-1 and avidin. As shown in Figure 3-23, there is a slight non-specific interaction between Poly-1 and avidin ($\tau_{\text{Poly-1/biotin-TMR}} \sim 0.79$ ms, while $\tau_{\text{Poly-1/TMR/avidin}} \sim 0.85$ ms), however, the effect is quite limited. A relatively large shift for Poly-1/biotin-TMR/avidin is well detectable, even at such a low concentration. A detection limit less than 100 pM for avidin is expected for our sensing system, which is lower than most of the values reported for avidin sensing.^{26, 198-201}

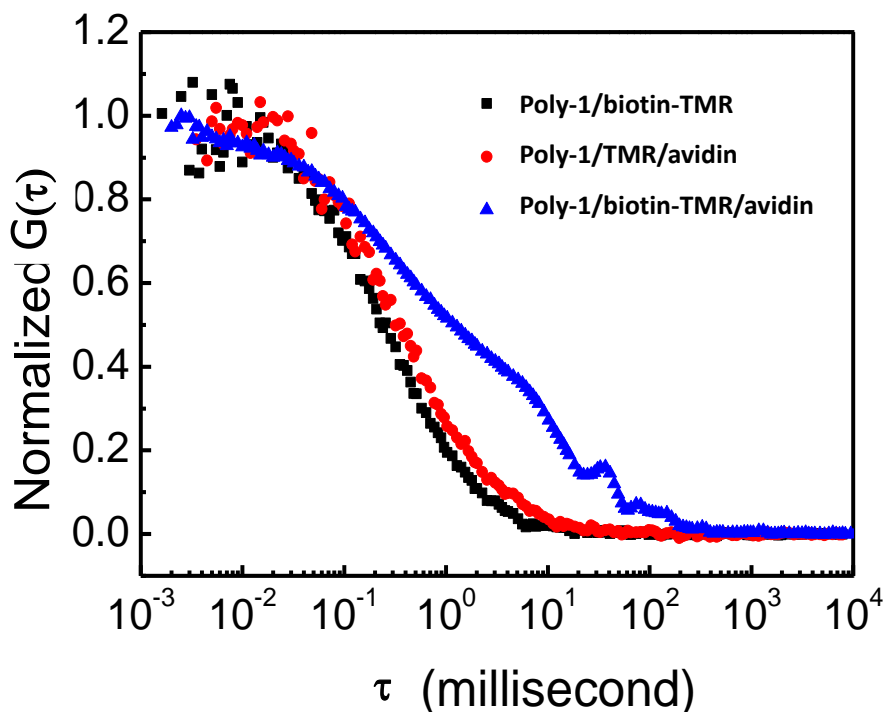


Figure 3-23. Autocorrelation FCS curves for Poly-1/biotin-TMR, Poly-1/TMR/avidin and Poly-1/biotin-TMR/avidin in phosphate buffer (10 mM, pH 7.4). [Poly-1] = 14.68 nM, [biotin-TMR] = 1 nM, [avidin] = 0.1 nM are fixed. Reprinted with permission from Wu, D. L., *et al.*¹⁷⁶

Conclusion

In summary, a fluorescent, helical CPE as the “transducer” for an avidin-biotin fluorescent sensor is first developed. The sensor response is based on FRET between an intercalated dye and the helical CPE, and interruption of this process by the

preformed avidin-biotin interaction. A systematic investigation on the fluorescence spectra of CPE mixed with pre-formed avidin/biotin-dye reveals the so-called phenomenon steric constraint. Relying on molecular recognition/hydrophobic interactions, a FRET-based discontinuous biosensing method is developed with a detection limit as low as 100 pM for the target protein. The intercalative interaction between dye-biotin and helical CPE as well as the formation of supramolecular aggregation of helical CPE/dye-biotin/avidin is further demonstrated by FCS and AFM images. A novel avidin sensing system is developed with signal response based on the diffusion behavior change of the CPE/dye-biotin in the presence of the target molecule avidin as $[\text{avidin}]/[\text{biotin}] > 0.1$. The sensitivity is < 100 pM, which is better than most of other methods reported. The two new biosensing strategies described in this chapter provide platforms for establishment of a highly sensitive biosensing system.

Experiments and Materials

Materials

The synthesis of Poly-1 and Poly-2 is described in the literature.^{23, 24} Biotin-TMR (5-(and-6)-tetramethylrhodamine biocytin) was purchased from Invitrogen. Avidin was purchased from Sigma. All sample solutions were prepared using water that was distilled and purified by a Millipore purification system (Millipore Simplicity Ultrapure Water System). Buffer solutions were prepared with reagent-grade materials (Fisher). All concentrations of polymers were provided in the polymer repeat unit concentration (PRU). Concentrated stock solutions of Poly-1, Poly-2, biotin-TMR and avidin were prepared in buffer to obtain the desired concentrations. All assays were conducted in 1 mM or 10 mM phosphate buffer (pH 7.4 or pH 10.5). Centrifugal filter units were bought

from Millipore. Membranes with both 10,000 and 30,000 molecular weight cutoff (MWCO) were used.

Preparation of Poly-1/biotin-TMR complex

The Poly-1/biotin-TMR complex was prepared by ultracentrifuging the mixture of 100 μ M Poly-1 and 10 μ M biotin-TMR in two centrifugal filter units with different molecular weight cutoff (MWCO, 30 kDa and 10 kDa) membranes under 14,000 x g. All of the polymer chains with MW higher than 30 kDa or less than 10 kDa, as well as free unbound biotin-TMR molecules, were centrifuged away. The remaining concentrated solution, which was collected for experiments, contains Poly-1/biotin-TMR complex with the MW in the range of 10 kDa - 30 kDa. Two buffer solutions, 10 mM phosphate buffers (pH 7.4 or pH 10.5), were used for sample preparation. Concentrations of two components ([Poly-1] = 9.6 μ M, [biotin-TMR] = 0.65 μ M) in the stock solution were calculated using Beer's Law,

$$c = \frac{A}{l \times \epsilon} \quad (3-2)$$

where A is absorbance. ϵ is the molar absorptivity or extinction coefficient in unit of $M^{-1} \cdot cm^{-1}$. The values for ϵ for each component are displayed in Table 3-1. l in unit of cm is the path length of the cuvette in which the sample is contained. c is the concentration of the compound in solution, expressed in M.

Negative Control Experiment by Using BSA

Protein bovine serum albumin (BSA, $pI = 4.7^{33}$), was added into the Poly-1/biotin-TMR ([Poly-1] = 102.8 nM, [biotin-TMR] = 7 nM) in pH 7.4 buffer to get [BSA] = 7 nM. The diffusion time becomes smaller (~ 0.68 ms) when comparing to the diffusion time 0.79 ms of Poly-1/biotin-TMR complex

Instrumentation.

FCS measurement

FCS measurements were performed using the homemade setup shown in Figure 3-7. The FCS was developed from an Olympus IX70. A 543 nm HeNe laser, specific for rhodamine dye, was employed as the excitation source light, which was focused onto the sample through Olympus 60x numerical aperture 1.2 water immersion objective. The fluorescence is collected by the same objective, separated from the excitation light by a dichroic mirror, then split by a 50/50 cube splitter and sent into an avalanche photodiode (SPCM-AQR-14-FC, Perkin Elmer) through a 50 μm -inner diameter optical fiber after passing through a 590 ± 20 nm band pass filter. Chambered Cover Glasses (Fisher) were used as the container for samples in FCS measurement. In each FCS experiment the fluorescence fluctuations were measured for 10-20 min. Free tetramethylrhodamine (TMR, $D = 2.88 \times 10^{-10} \text{ m}^2 \cdot \text{s}^{-1}$)¹⁴³ was used for calibration. Autocorrelation was processed by a hardware correlator (ALV 5000/EPP, ALV-GmbH, Langen, Germany).

Fluorescence spectroscopy.

Fluorescence spectra were recorded on a Photon Technology International (PTI) fluorometer and corrected by using correction factors generated with a primary standard lamp.

UV-Vis measurement

UV-Vis spectra were measured in quartz cuvettes with 1 mm light path on a UV-Vis spectrophotometer (Shimadzu, UV-1800).

CHAPTER 4

STUDY OF CONFORMATION CHANGE OF CPES INDUCED BY PROTEINS AND DEVELOPMENT OF SENSOR ARRAY FOR PROTEINS BY FCS

Background

In recent years, the interactions between CPEs and proteins have drawn much attention.^{33, 34, 97, 109-111, 123, 131} It has been well elucidated from spectra that the “non-specific” interaction causes significant change in both conformation and photophysical properties of CPEs.^{33, 34, 97, 110} For instance, Bazan and coworkers found that an anionic sulfonated PPV mixed with small amounts of various proteins, including positively charged avidin and tau as well as negatively charged bovine serum albumin (BSA) and pepsin A, would have a several-fold increase in emission intensity, which was arise from a combination of electrostatic and hydrophobic forces.³³ Bunz and coworkers also reported that BSA could enhance fluorescence of a carboxylate-substituted CPEs; While a series of proteins, such as histone, lysozyme, myoglobin, and hemoglobin quenched the fluorescence of CPE due to the formation of complex.¹¹⁰

Here, the aggregation state change of CPEs induced by interaction with various proteins is explored by focusing on the diffusion dynamics of the resulting polymer/protein aggregates. FCS has already been employed to study the conformation change of large molecules, e.g., Borsch and coworkers used FCS to monitor protein folding or unfolding transitions.¹⁴² Schwille and coworkers conducted research on the fluorescence fluctuations of green fluorescence protein (GFP) by FCS and revealed the relationship between structural changes of GFP and its fluctuations in emission, making the probing local pH possible.²⁰² Waldeck and coworkers have uncovered the three regimes in the hydrodynamic radius changing of the complexes formed by an anionic CPE and a surfactant via FCS.¹³¹ Our group has recently systematically investigated the

aggregation of a dye-ligand intercalated helical CPE induced by avidin and developed a novel avidin sensor.¹⁷⁶ Therefore, FCS is very attractive as a promising tool for monitoring the aggregation state and size change of CPEs.

The current chapter explores how the aggregation state or size of six CPEs changes when exposed to solutions of seven different types of proteins, which is accomplished by measuring their diffusion time through FCS and analyzing their diffusion behavior change. If the charge types of CPEs and proteins are opposite, the aggregation of CPEs are easily observed; by contrast, if the CPEs and proteins have the same charge nature, de-aggregation occurs for CPEs in aqueous solution. Meanwhile, other factors including charge density, protein molecular weight, and polymer backbone structure also influence the final physical state of CPEs. As a result, the final diffusion time for each CPE-protein mixture varies and the diffusion time response pattern created by the six-CPE array for a typical protein is unique, which can be utilized for protein recognition and distinction.

Subsequently, a sensor array comprising six CPE probes with various charge properties, structure characteristics and molecular scales is developed for seven proteins, which also have various isoelectric point (pI), molecular weight and structure specificity. Each type of protein can be well classified via linear discriminant analysis (LDA) of the FCS diffusion times. Combination of sensor array with LDA has been applied in many sensing strategies.^{97, 124, 203, 204} In this project, multiple LDA operations are employed for training data matrix, and creating a series of canonical plots as standard patterns for classifying different proteins. Then the technique readily identifies a series of unknown protein samples with recognition accuracy 93%. One superior

advantage for this sensing approach is noninvasive and labor-saving. Unlike the conventional sensors requiring specific markers design, the CPE probes do not need to be attached covalently but undergo self-assembly via non-specific interaction. This novel protein sensor array will make contribution to the medical diagnostics or clinical research,⁸²⁻⁸⁵ where detection of more than one protein in one single technical setting at one time is highly preferred.

Results and Discussion

Properties of Six CPEs and Seven Proteins

A set of six CPEs consisting of three with anionic and three with cationic ionic charge were chosen for exploring their interactions with proteins. The CPE structures with their abbreviations are shown in Figure 4-1 and their estimated molecular weights are listed in Table 4-1. A series of normalized absorption/emission spectra for those CPE is displayed in Figure 4-2. The first anionic CPE, P1, is a poly(phenylene ethynylene) (PPE) with poly(ethylene glycol) (PEG) hydrophilic side chains and dendritic carboxylate groups. The bulky, highly charged ionic functional groups are capable of keeping the “single chain state” of P1 by reducing the hydrophobic interchain interactions and increasing the electrostatic repulsion between polymer chains. The fluorescence spectrum of P1, which features sharp emission peak around 470 nm, evidences the dominance of non-aggregated chains in the solution. Two other anionic CPEs, P2 and P3, have similar structure featuring PPE backbone and sulfonated side groups. The only difference in structure is P2 is *meta*-linked whereas P3 is *para*-linked on the phenyl ring of the backbone. In water, P2 self-assembles into a helical conformation in aqueous solution, attributed to the intra-molecular π - π stacking interaction in their backbones.^{23, 51} P3 can form lamellar aggregates in the aqueous

solution.^{24, 26, 127, 205, 206} Both P2 and P3 have broad emission band as shown in Figure 4-2.

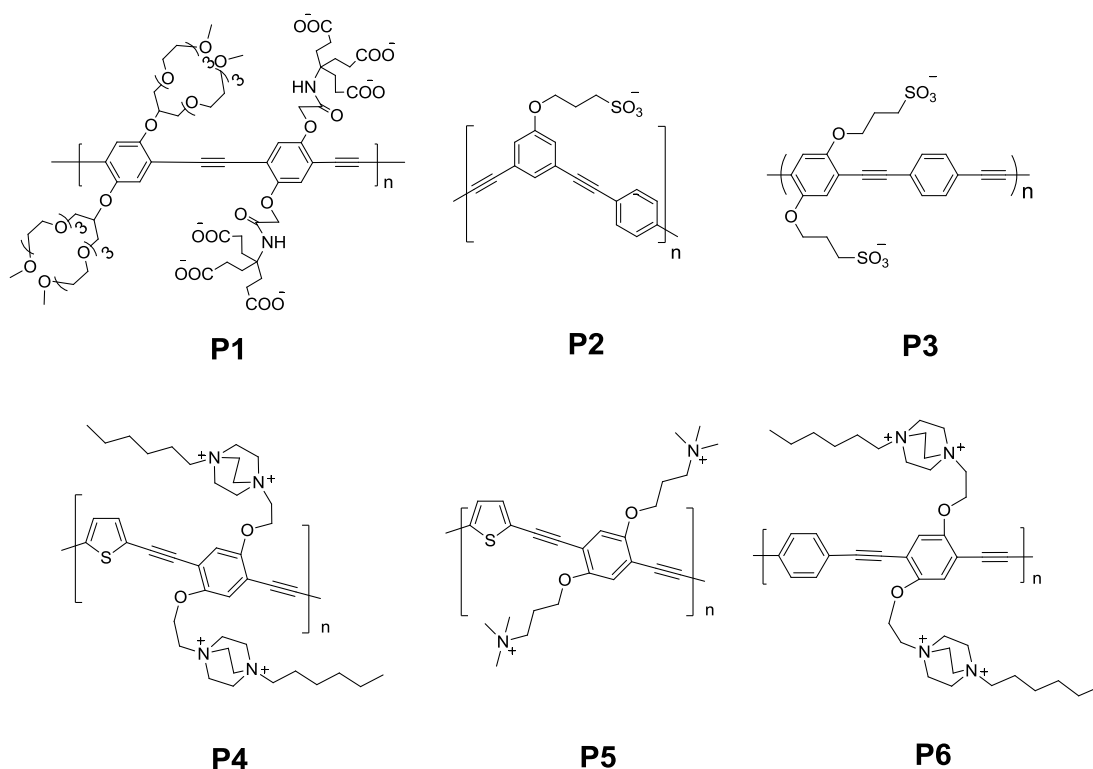


Figure 4-1. Chemical structures of six CPEs.

Table 4-1. Basic information of CPEs (diffusion times are measured in 5 mM HEPES buffer, pH 7.2, room temperature by FCS).

	P1	P2	P3	P4	P5	P6
Estimated MW (kDa)	11.0	40.0	~100.0	10-70	NA	7-70
τ_d ($\times 10^{-5}$ s)	8.4 ± 0.9	29.4 ± 3.0	101.3 ± 25.9	21.7 ± 3.9	27.3 ± 3.1	24.0 ± 8.6

The cationic CPEs P4 and P6 are less aggregated than P3 due to their relatively long cationic bisalkylammonium side groups that provide a steric barrier between the π -conjugated chains.²⁹ This statement can be proved by comparing their emission spectra (Figure 4-2), where the peaks with shorter wavelength corresponding to the higher emitting energy in non-aggregated states, are obvious for P4 and P6 but invisible for P3. While P5 displaying related broad emission band can also be explained as its shorter

side groups are not capable to prevent aggregation. Due to their various molecular weights and conformations, this set of six CPEs displays different diffusion behavior reflected by the FCS diffusion time as summarized in the bottom row of Table 4-1. It is not possible to apply gel permeation chromatography to measure the absolute molecular weights (MW) for P2-P6 due to their amphiphilic nature; however, other techniques have been used to estimate their MWs.^{23, 24, 29} The results are displayed in Table 1 with the factor that the CPEs of higher molecular weights generally display longer diffusion times.

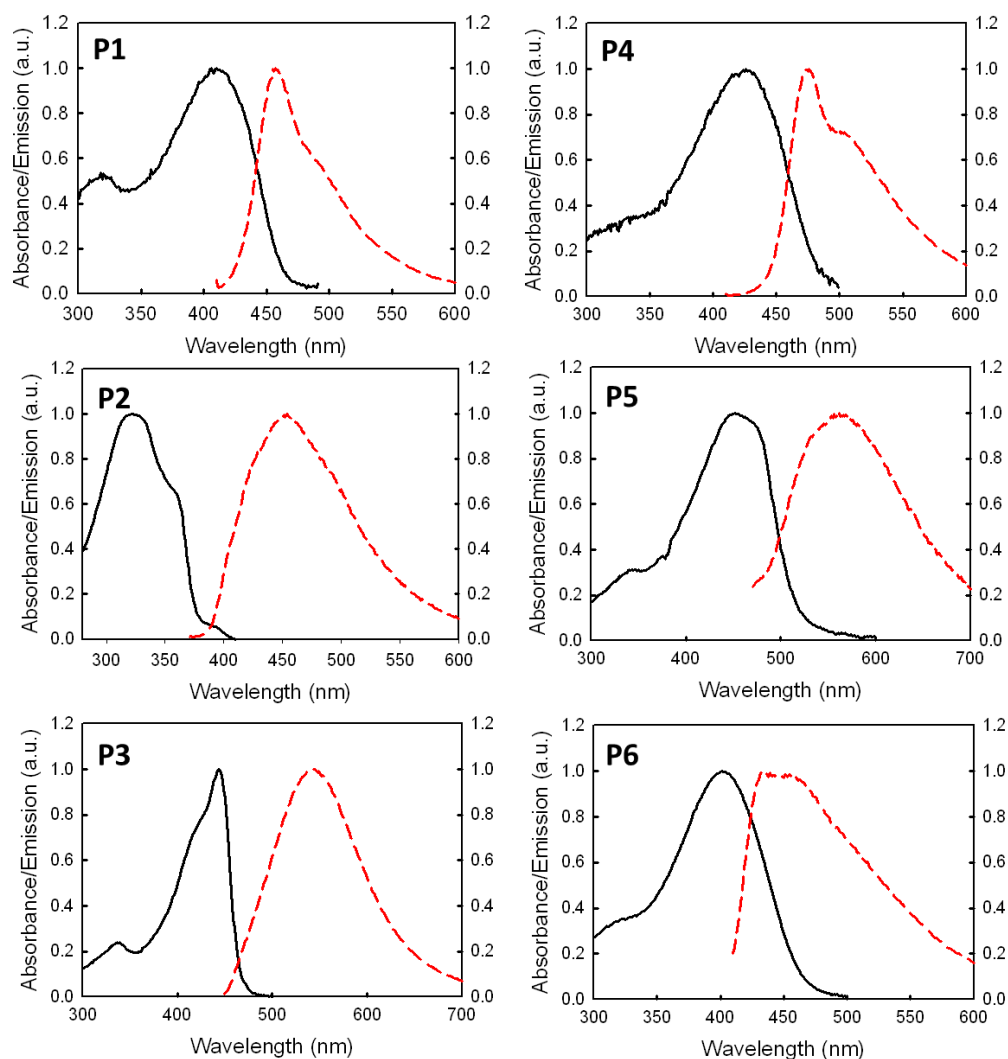


Figure 4-2. Normalized absorption and emission spectra for six CPEs.

Seven proteins were used in this work and their properties are summarized in Table 2 along with the acronyms that are used herein. Avidin and LYZ have isoelectric point (pI) > 7 , exhibiting positive charge in neutral solution; PLD2, HK3,²⁰⁷ BSA, and GOx have $pI < 7$, so they are negative in neutral solution. However, for the protein HRP, due to its complexity, it is hard to determine its pI value.²⁰⁸ Those proteins also feature different molecular weights varying from 14-200 kDa and distinct structural characteristics.

Table 4-2. Basic information of proteins.

Abbreviation	Protein	MW (kDa)	pI
Avidin	Avidin	66	10
LYZ	Lysozyme	14	11.0
HRP	Horseradish Peroxidase, type I	44	3-9
PLD2	Phospholipase D, type II	200	4.65
HK3	Hexokinase Type III	54	PI :5.25 PII: 4
BSA	Bovine Serum Albumin	66	4.7
GOx	Glucose Oxidase	160	4.2

FCS Results and Discussion

To quantitatively test the interaction between the CPEs and proteins, all the experimental conditions including concentrations of both CPEs and proteins, ion strength and pH of buffer solution ($pH = 7.2$) are fixed. The concentrations of proteins were determined through Bradford protein assay, a dye-binding assay in which a differential color change of a dye occurs in response to various weight concentrations of protein.²⁰⁹ Each of the six CPEs are mixed with seven proteins individually in 5 mM HEPES buffer with final $[CPE] = 500$ nM (in repeat units) and $[protein] = 2$ $\mu g/mL$. Twenty replicates are prepared for each CPE-protein pair and all the samples are submitted for FCS measurement in sequence.

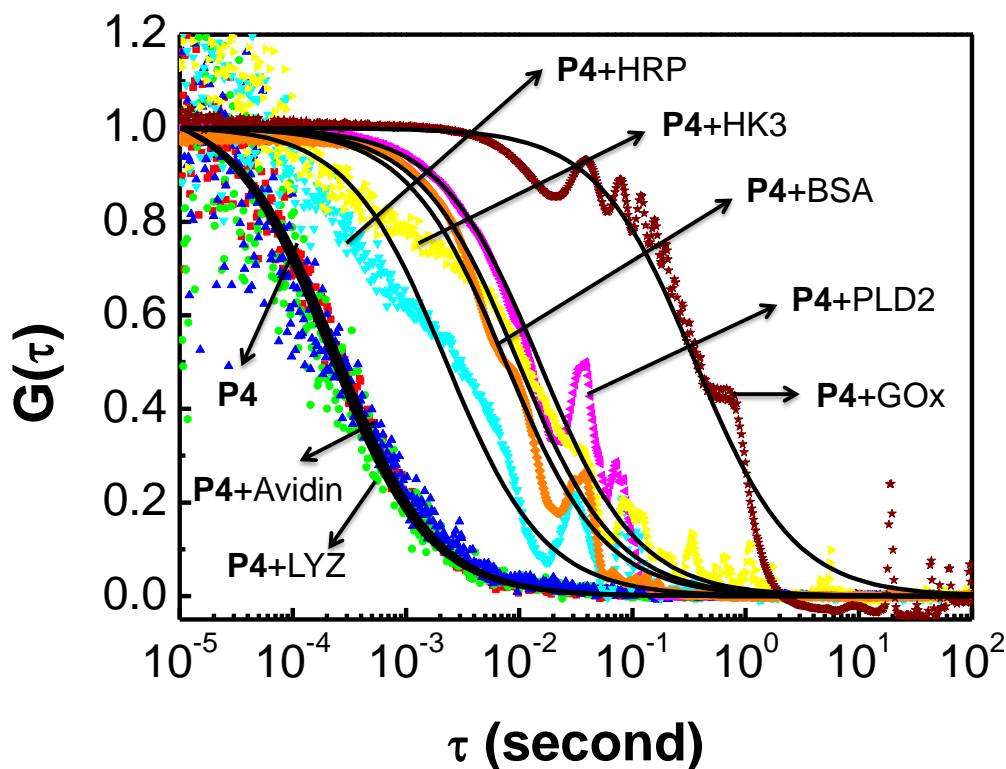


Figure 4-3. FCS curves for P4 without protein (■) and with avidin (●) LYZ (▲) HRP (▼) HK3 (▴) BSA (◆) PLD2 (▾) GOx (★) in 5 mM HEPES buffer pH 7.2. Black lines are the single species fitting curves.

Figure 4-3 illustrates a typical FCS measurement results for the cationic CPE, P4, with and without seven proteins. Based on the FCS curves, the mixtures of P4 with avidin ($\tau_d = 20.7 \times 10^{-5}$ s) or LYZ ($\tau_d = 22.5 \times 10^{-5}$ s), whose *pI* value > 10, have approximately the same diffusion times as pure P4 ($\tau_d = 21.7 \times 10^{-5}$ s). By contrast, the other 5 proteins, whose *pI* averagely < 7, to various degrees, induce the aggregation of P4 and a dramatic increase in the diffusion times. The order for the diffusion rate of P4/proteins is: HRP > BSA > HK3 > PLD2 > GOx with increasing $\tau_d = 1.95, 5.66, 7.80, 13.00$, and 219.00 ms, respectively. Due to the polydisperse nature of the aggregates, the FCS curves are the combination of several single-species curves with different diffusion times. Nevertheless, the single species fitting equation (Equation 2-2) is still

applied and an average diffusion time for each CPE/protein aggregate is thereby obtained. As stated above, HRP and HK3 are the mixtures of several isozymes. Their FCS curves are more complicated and difficult to be fit by a single species fitting equation.

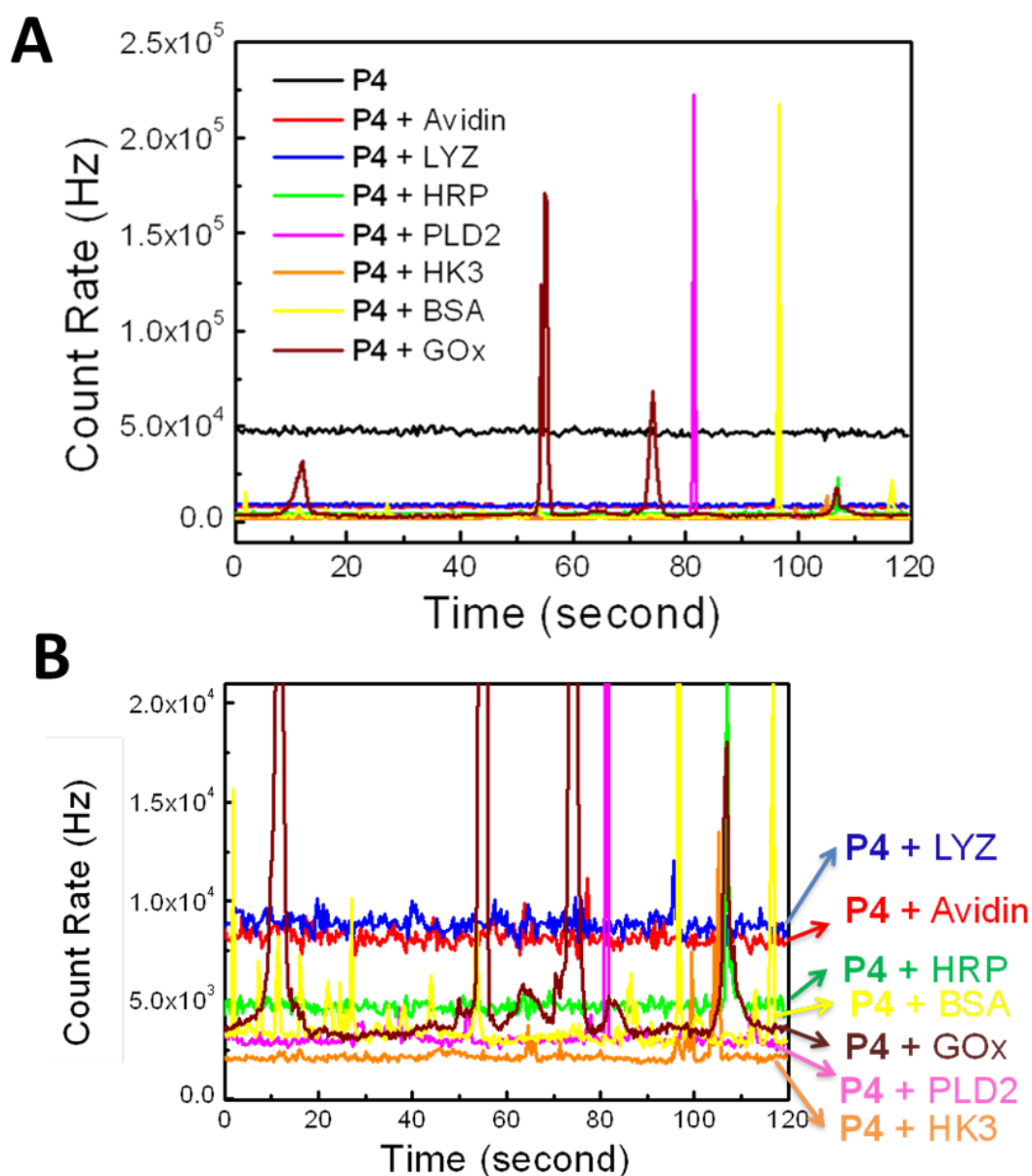


Figure 4-4. Fluctuation profiles for A) P4 without and with seven proteins and B) their enlargement ($[P4] = 500 \text{ nM}$, $[\text{protein}] = 2 \text{ }\mu\text{g/mL}$ in 5 mM HEPES buffer pH 7.2).

The fluorescence fluctuation profiles for each mixture are displayed in Figure 4-4. Higher and broader peaks are corresponding to the large aggregates passing through the excitation volume which lead to longer diffusion times as shown in Figure 4-3. Those time-dependent profiles also provide the evidence for the heterogeneity or size multi-distribution of aggregated CPEs.

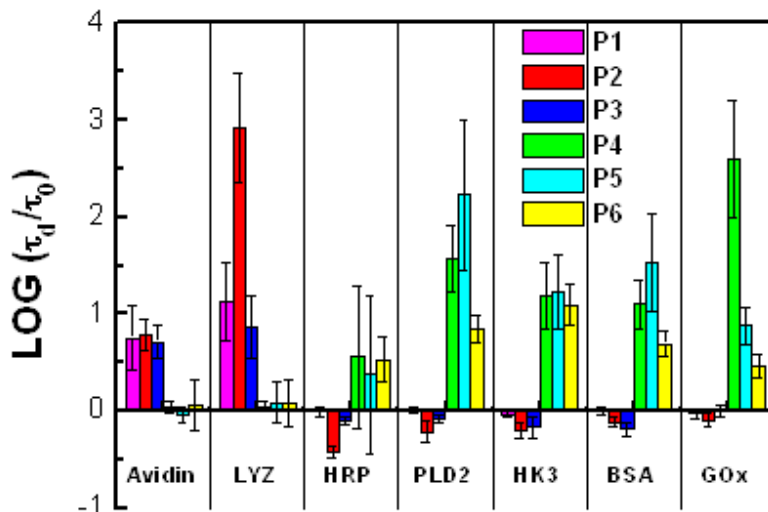


Figure 4-5. Log (τ_d/τ_0) response 2D bar pattern of six CPEs mixing with seven proteins. Bar height is the average value of twenty replicates for each CPE-protein pair.

The FCS results for all the samples are shown as a bar graph in Figure 4-5 in terms of $\log (\tau_d/\tau_0)$, where τ_d and τ_0 are the diffusion time of CPE with and without protein, respectively. The error bars represent the calculated standard deviation for 20 replicates. Figure 4-6 is the 3D column graph for the FCS results. The rows with the same color are belonging to the same protein and the charge type for each species is embodied in their abbreviations by color: negative charge is black, positive charge is red and the protein HRP with mixed pI is blue. There are several clear trends that emerge upon inspection of the data in Figures 4-5 and 4-6. First, it is clear that the diffusion time increases (i.e. $\log (\tau_d/\tau_0) > 0$) for the oppositely charged CPE/protein pairs, e.g., LYZ/P1, or PLD2/P4, due to the attraction-induced formation of polymer-protein aggregates. In

sharp contrast, when the charge of the protein and CPE are the same, especially for the pairs of anionic CPE and protein with $pI < 7$, such as PLD2/P2 or HK3/P3, the mixtures exhibit shorter diffusion time compared to the CPE alone (i.e., $\log (\tau_d/\tau_0) < 0$).

Apparently the Coulombic repulsion between two anionic macromolecules disrupts the aggregation of CPEs.

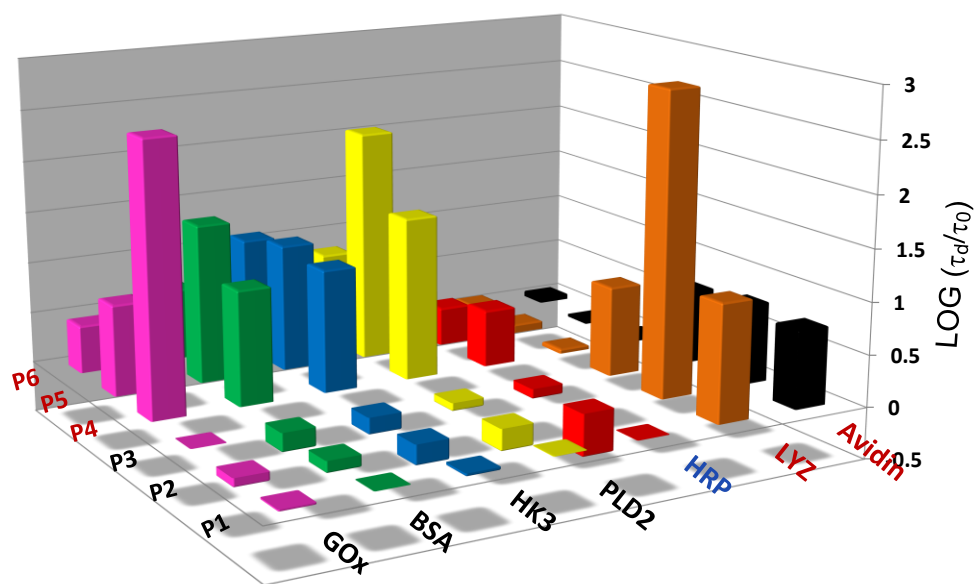


Figure 4-6. Log (τ_d/τ_0) response 3D column pattern of six CPEs mixing with seven proteins. Column height is the average value of twenty replicates for each mixture.

For the cationic CPE with positively charged proteins, e.g., LYZ/P5 or P6, some aggregation is apparent with average $\log (\tau_d/\tau_0)$ varying in the range of 0-0.1. This is likely due to the hydrophobic interaction.¹⁰⁹ The much larger error bars observed for HRP/CPE pairs (e.g., HRP/P5), is presumably due to the complexity in the mixture of protein isozymes. However, based on the average $\log (\tau_d/\tau_0)$ values for HRP with various CPEs, HRP is able to induce aggregation when mixed with cationic CPEs, while disrupting aggregation when mixed with anionic aggregated CPEs. Therefore, HRP is displaying more anionic characteristics in neutral system.

Besides electrostatic or hydrophobic interaction, other factors may also influence the final response. For example, the $\log(\tau_d/\tau_0)$ for anionic P2 with cationic LYZ is much larger compared to that of P2 with avidin. We attribute this phenomenon to the high charge density of LYZ, which has the smallest molecule weight and highest pI value. However, when considered P4 mixed with a series of anionic proteins, the molecule weight of proteins seems have impact on the final diffusion time change. The value of $\log(\tau_d/\tau_0)$ increases roughly as the increase of the molecular weight of the protein: HRP (44 kDa) < HK3 (54 kDa) \approx BSA (66 kDa) < PLD2 (200 kDa) < GOx (160 kDa). However, this trend does not apply to other types of oppositely charged CPE/protein mixtures.

In addition to the influence of the protein, the properties of polymers also influence the trends in the diffusion time changes for the CPE-protein mixtures. For example, the thiophene containing CPEs (P4 and P5) appear to form larger aggregates compared to P6 which contains only phenylene repeat units. In particular, when P4 is mixed with oppositely charged proteins (BSA, HK3, PLD, GOx), the resulting $\log(\tau_d/\tau_0)$ values are larger than those for P6 with the same proteins. This finding is consistent with the previous reports that the thiophene containing CPEs appear to have a larger hydrophobic character compared to the phenylene analogues.²¹⁰ The bond linking style in backbone may also enhance the interaction between CPE and proteins. For instance, the diffusion time for P2, a helical CPE, is greater than that of P3, which has linear backbone, mixed with oppositely charged proteins (LYZ, avidin), even though P3 has higher MW than P2 does. Consequently, the final signal response is affected by charge type, charge density, molecular weight and structure property of both proteins and CPEs. It is difficult to de-convolute each part just relying on the FCS measurement. We

are pleased to find that the six CPEs are displaying unique signal response pattern for each protein, which is much beneficial for processing distinguish and identification of proteins in the next sensory development.

Protein Sensing

Linear discriminant analysis of FCS diffusion times for protein/CPE mixtures

In order to provide more insight into the structure-property relationships for the CPE/protein mixtures, we carried out studies aimed at subjecting the FCS results to linear discriminant analysis (LDA, the details of the theory and procedures for LDA can be found in the literature).^{125, 126} As outlined below, this work leads to the development of a novel CPE-FCS based method allowing the identification of a protein in an unknown sample (Figure 4-7). As can be seen below, a single LDA operation on the entire set of data was unable to afford a high degree of accuracy due to the reason that the single LDA was originally developed for two-class problems and it is sub-optimal if multiple classes are considered.²¹¹ Thus, we applied a sequence of LDA steps afterwards to multiple subgroups of proteins and generated subspaces that have higher overall classification power.²¹²

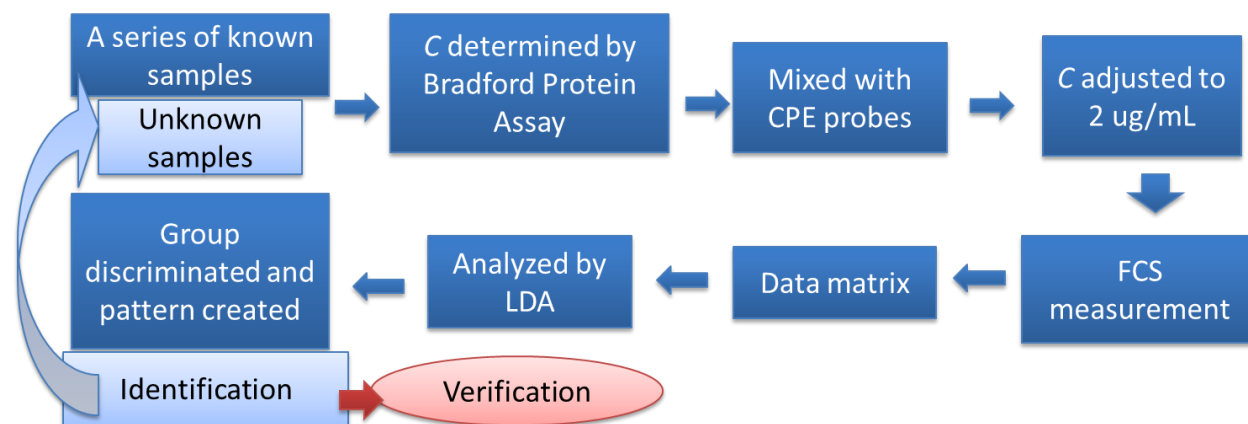


Figure 4-7. Flowchart for protein sensor array development.

The details about the multiple LDA process can be found in Figure 4-8. Initially, we used the full set of $\log(\tau_d/\tau_0)$ values to construct a matrix consisting of (6 CPEs) \times (7 proteins) \times (20 replicates) for LDA analysis (Table A-1 in Appendix A). The eigenvectors which maximize the ratio of between-class variance to the within-class variance are obtained through LDA implemented as a script in Matlab. Then the three most significant eigenvectors (carrying 82.5, 9.31, and 5.77% of the discriminant information, respectively) are used to plot sample data in a 3D discriminant space as shown in Figure 4-9A. The 6 \times 7 \times 20 samples are presented with different colors denoting the different proteins. In principle, each protein should occupy a specific region in the 3D space and the different proteins should be well separated from each other. As displayed in Figure 4-9A and Figure 4-10, three protein groups of avidin, BSA and GOx are well classified with individual accuracy $\geq 95\%$. However, mingling occurs among the categories of HRP, PLD2, HK3 and BSA with error to be 4/20, 7/20, 7/20, and 5/20, respectively, resulting in the total classification accuracy 83%.

A second LDA operation is applied using only the sub-sets of data that belong to HRP, PLD2, HK3 and BSA. A new discriminant space specifically for these four proteins is created and the improvement in the separation of groups can be easily observed (Figure 4-9B). The errors are reduced to be 2/20, 2/20, 2/20, and 1/20 for HRP, PLD2, HK3 and BSA, respectively, with an increased total accuracy 94% for seven proteins (Figure 4-10). More LDA operations are continuously applied for those groups with relatively lower individual training accuracy ($<95\%$). As shown in Figure 4-9C, D and Figure 4-10, after four times LDA operations, the total classification accuracy for the 6 \times 7 \times 20 training matrix reaches 98%, much higher than the result of a single LDA

operation, i.e., 83%. By building up multiple subspaces instead of a single large space, the protein discriminant method is well established (4 sets of eigenvalues are summarized in Table 4-3).

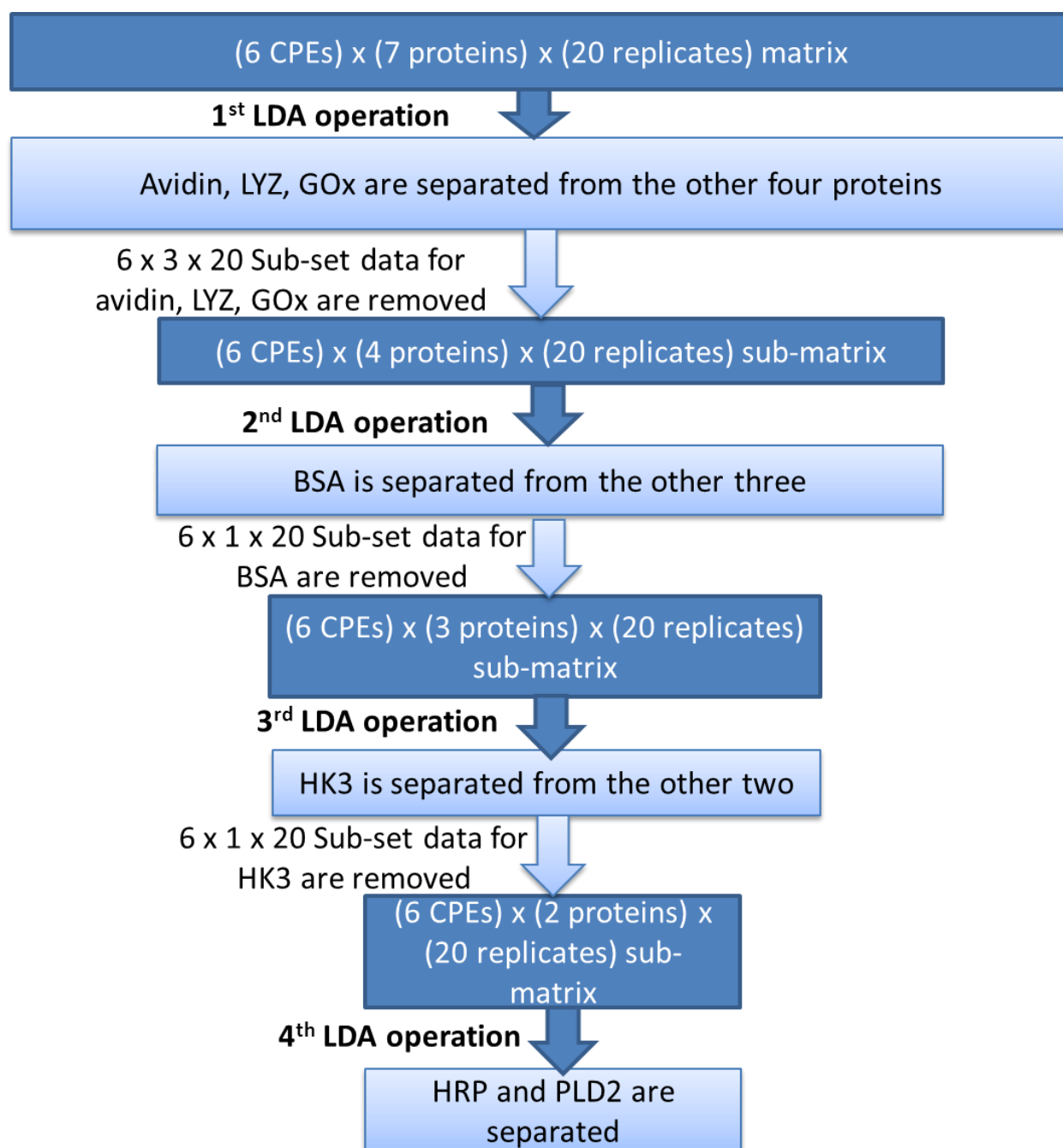


Figure 4-8. Flowchart of multiple LDA operation for training known samples.

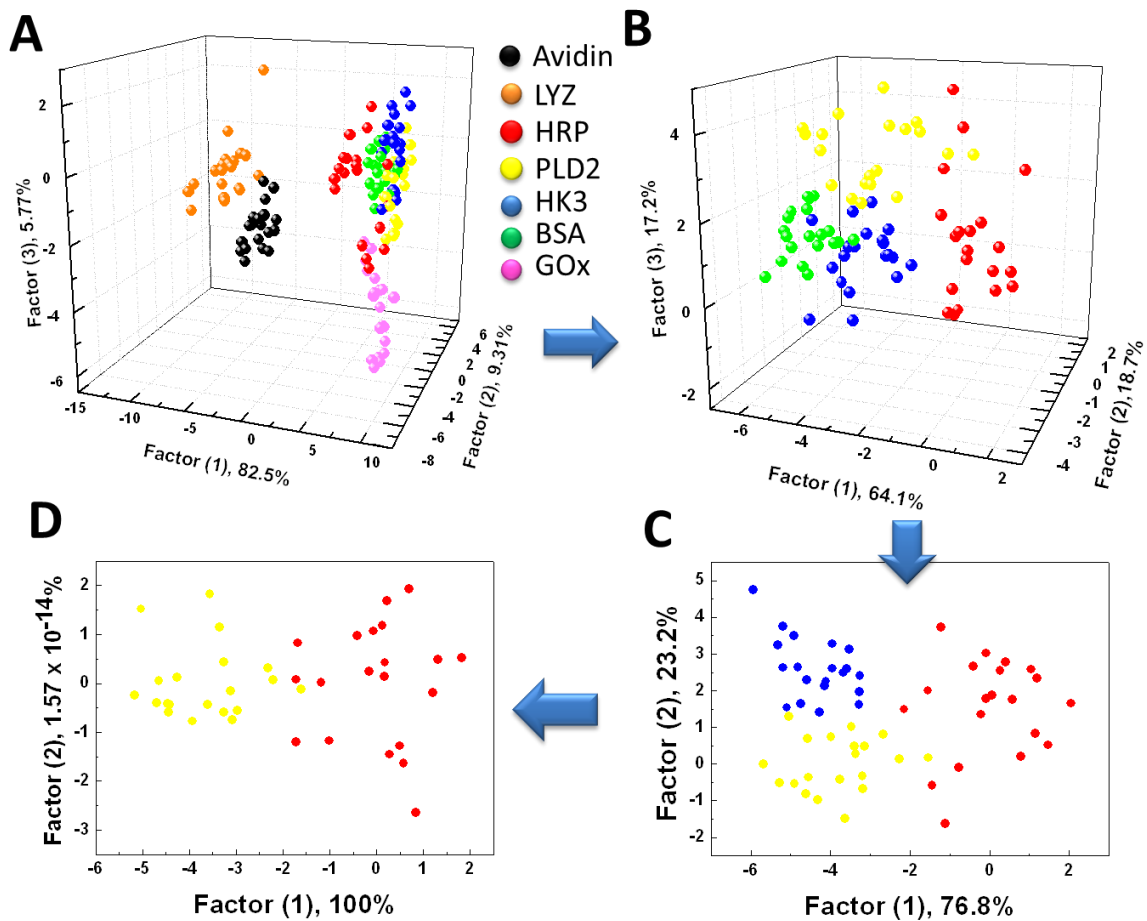


Figure 4-9. LDA discriminant spaces/plots for the diffusion time response patterns obtained with six CPE probes sensor array against A) seven proteins (avidin, LYZ, HRP, PLD2, HK3, BSA, GOx), B) four proteins (HRP, PLD2, HK3, BSA), C) three proteins (HRP, PLD2, HK3), D) two proteins (HRP, PLD2). Twenty replicates for each mixture.

Table 4-3. Eigenvalues with their percentage of each LDA operation training matrix.

LDA operation	1	2	3	Total
1 st	1.7293 (82.5%)	0.1951 (9.31%)	0.1209 (5.77%)	2.0963
2 nd	0.2026 (64.1%)	0.0593 (18.7%)	0.0543 (17.2%)	0.3162
3 rd	0.1975 (76.8%)	0.0597 (23.2%)		0.2572
4 th	0.1772 (100%)			0.1772

1 st LDA training								
	Avidin	LYZ	HRP	PLD2	HK3	BSA	GOx	Sum
Error/total	0/20	0/20	4/20	7/20	7/20	5/20	1/20	24/140
Training Accuracy	100%	100%	80%	65%	65%	75%	95%	83%

2 nd LDA training								
	Avidin	LYZ	HRP	PLD2	HK3	BSA	GOx	Sum
Error/total	0/20	0/20	2/20	2/20	2/20	1/20	1/20	8/140
Training Accuracy	100%	100%	90%	90%	90%	95%	95%	94%

3 rd LDA training								
	Avidin	LYZ	HRP	PLD2	HK3	BSA	GOx	Sum
Error/total	0/20	0/20	2/20	2/20	0/20	1/20	1/20	6/140
Training Accuracy	100%	100%	90%	90%	100%	95%	95%	96%

4 th LDA training								
	Avidin	LYZ	HRP	PLD2	HK3	BSA	GOx	Sum
Error/total	0/20	0/20	0/20	1/20	0/20	1/20	1/20	3/140
Training Accuracy	100%	100%	100%	95%	100%	95%	95%	98%

Figure 4-10. Training results for multiple LDA operation of diffusion time response for six CPE probes against seven proteins (twenty replicates for each probe-target pair).

Unknown sample test

After succeeding in classifying known samples, the detection and identification of unknown protein samples (Table B-1 in Appendix B) were further studied. Forty-two artificial protein samples prepared by a second researcher are undergoing the same protocol as described above, including determining concentration through Bradford protein assay, mixing proteins with six CPE probes individually, adjusting their

concentrations to [CPE] = 500 nM and [protein] = 2 µg/mL, conducting FCS measurements and generating final data matrix (Figure 4-7).

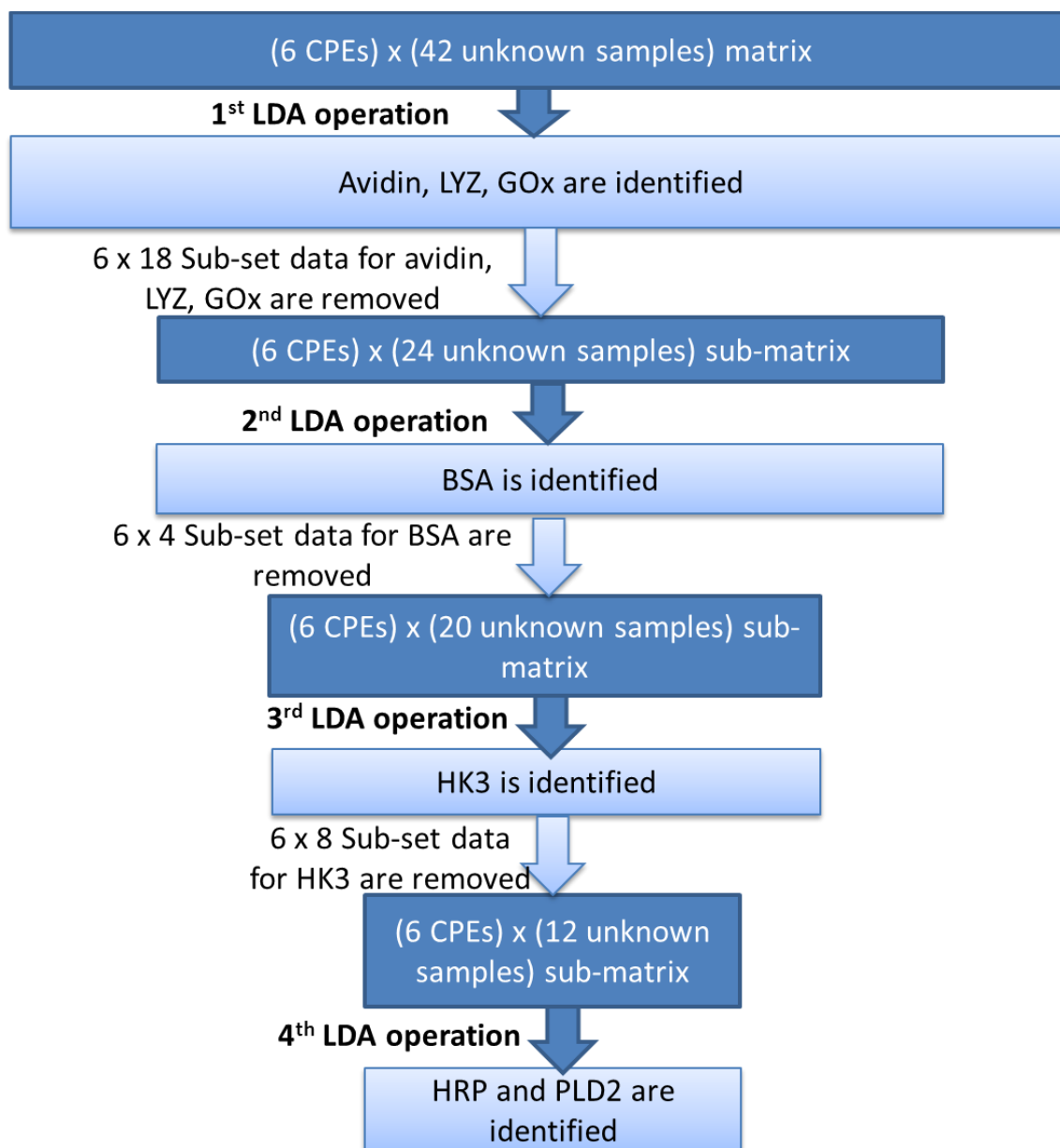



Figure 4-11. Flowchart for multiple LDA operation for testing unknown samples.

As processed by first level LDA operation, the entire unknown samples are projected to the discriminant space built up in the above training process. Based on the theory of LDA,^{125, 126} in the created 3D discriminant space, the Mahalanobis distances of each unknown spot in the space to the centroid of each class are calculated and these

unknown spots are assigned and identified according to the shortest Mahalanobis distance. Based on the classification accuracy obtained in the training process, the samples that assigned to the groups of avidin, LYZ and GOx are believed to be identified with accuracy > 95%. The sub-set data belonging to those three proteins are removed from the entire matrix, and the rest matrix is submitted for a second level LDA operation and processed in a similar manner (Figure 4-11). As four-time LDA has been operated, all of the unknown samples get identification. Verification is assisted by the researcher who prepares unknown samples. Error report is shown in the Figure 4-12. Total identification accuracy is improved from 88% (failure test: 1 for HRP, 1 for HK3, and 3 for BSA) for a single LDA operation to 93% (failure test: 1 for HRP and 2 for BSA) for a multiple LDA operation (final failure test samples are marked with star in Table B-1).

	Avidin	LYZ	HRP	PLD2	HK3	BSA	GOx	Sum
Error/total	0/6	0/6	1/6	0/6	1/6	3/6	0/6	5/42
Test Accuracy	100%	100%	83%	100%	83%	50%	100%	88%



Multiple LDA operation

	Avidin	LYZ	HRP	PLD2	HK3	BSA	GOx	Sum
Error/total	0/6	0/6	1/6	0/6	0/6	2/6	0/6	3/42
Test Accuracy	100%	100%	83%	100%	100%	66.7%	100%	93%

Figure 4-12. Test results for multiple LDA operation of diffusion time response for six CPE probes against forty-two unknown protein samples.

Based on the LDA results discussed above, we can find that proteins with $pI > 7$, e.g., avidin and LYZ, are easily separated from the rest groups with

classification/identification accuracy ~100% for both known and unknown samples, followed by GOx ($pI = 4.2$) with classification/identification accuracy 95% and 100% for known and unknown samples, respectively. HRP, PLD2, HK3 and BSA are relatively hard to be distinguished from each other, which are probably due to their similarity in charge properties, resulting in similar interaction with each CPEs and requiring further LDA processes. The complexity in the pI value for multi-isozyme mixture, such as HRP, may also bring in the difficulty in identification of proteins: the identification accuracy for HRP is relatively low. The separation of proteins with opposite charge is the easiest to be achieved, suggesting the charge type plays the most significant role in the interaction between CPEs and proteins as well as the recognition of proteins. While further discriminant between proteins with similar charge properties needs more analysis on the minor differences in data matrix. Those differences probably arise from molecular structure, charge density or molecular weight of both CPEs and proteins. As discussed above, those factors can also make their own contributions to the differentiation of proteins.

Summary

In sum, a systematical investigation was conducted on the aggregation state/size change of CPEs induced by non-specific interaction between various CPEs and proteins from a molecular dynamics aspect. By employing FCS system, the aggregation/de-aggregation of CPEs can be reflected on the diffusion behavior changes. Many factors including charge type, charge density, molecular weight and structure of CPEs or proteins contribute to the final conformational and diffusional changes of CPEs. Among those factors, charge type plays the essential role. The patterns of signal responses generated by six CPEs are discernible for different proteins, arousing the

development of a new CPE based sensor array for protein. By applying multivariate pattern recognition chemometrics, LDA, in a multiple operation mode, a series of discriminant spaces is created and seven different proteins have been successfully classified. Forty-two unknown samples were further tested and a high identification accuracy 93% was obtained, which verified the robustness and feasibility of this novel sensor array. This type of sensing strategy establishes a new protein sensing platform where the proficient manipulation and strong biological background are not required for operators. Further effect can be made upon the optimization of probes including improving the monodispersion of polymers, conjugating more versatile functional groups to the backbone or introducing in new probes. Moreover, the development of the sensor array in more complicated biological environments is necessary to eliminate potential interference and enhance their feasibility in the real world.

Material and Experiment

Materials

Avidin from egg white (avidin, A9275), lysozyme from chicken egg white (LYZ, L6876), peroxidase from horseradish, type I (HRP, P8125), phospholipase D from arachis hypogaea (peanut), type II (PLD2, P0515), hexokinase from saccharomyces cerevisiae, type III (HK3, H5000), albumin from bovine serum (BSA, A2153), and glucose oxidase from *Aspergillus niger* (GOx, G7141) were purchased from Sigma. The synthesis procedures and characterization of P1,^{182, 183} P2,²³ P3,²⁴ P4,²⁹ P5,²⁷ and P6²⁹ has been previously reported. All sample solutions were prepared using water that was distilled and purified by a Millipore purification system (Millipore Simplicity ultrapure water system). Buffer solutions were prepared with reagent-grade materials (Fisher). All concentrations of polymers are provided in polymer repeat unit concentration (PRU).

Concentrated stock solutions of the CPEs and proteins were prepared in buffer to obtain the desired concentrations. All assays were conducted in 5 mM phosphate buffer, pH 7.2 at room temperature. Coomassie brilliant blue G-250 was obtained from Sigma. Phosphoric acid and methanol were HPLC grade solvents bought from Sigma.

Bradford Protein Assay Procedure

Bradford protein assay was conducted following an instruction.²¹³ Coomassie Blue G (10 mg) was dissolved in 5 mL of methanol and displaying dark blue. The solution was added to 10 mL of 85% H₃PO₄, and diluted to 20 mL with Millipore water. The final reagent was dark red and containing 0.5 mg/mL Coomassie Blue G, 25% methanol, and 42.5% H₃PO₄. The stock solution was kept in a dark bottle at 4°C. The assay reagent was freshly prepared for each measurement by diluting 1 volume of the dye stock with 4 volumes of Millipore H₂O and it appeared brown. Six standard solutions (1 mL each) containing 0, 250, 500, 1000, 1500 and 2000 µg/mL BSA (extinction coefficient 43,824 M⁻¹ cm⁻¹ at 280 nm)²¹⁴ were prepared as standard samples. The UV-Vis spectrophotometer was set in a point-read mode at 595 nm to collect the data. A 4 mL plastic cuvette filled with millipore water was inserted to auto-zero the reading at 595 nm. 2.0 mL assay reagent and 0.04 mL of protein standard solution were mixed in a vial and it was gently inversely shaken several times. After 10 min standing, the absorbance of each stable sample was measured under room temperature, starting with the lowest protein concentration and working up. All the absorbance must locate between 0 and 2, otherwise, the outstanding sample should be adjusted or rejected and repeated. A plot of absorbance at 595 nm vs [BSA] as the standard curve was drawn through the instrument. The Bradford assay gives a hyperbolic plot for absorbance versus protein concentration, but within a range of relatively low protein concentrations, the hyperbolic

curve can be approximated reasonably well by a straight line.²¹³ A one order straight line was used to fit the points and a high fitting coefficient above 0.99 was obtained (if not, all the experiments should be restarted over). The measurement of protein samples with unknown concentration was followed the same procedure and their absorbance at 595 nm was obtained. By using the standard curve, their concentrations were easily figured out.

Instrumentation

FCS measurement.

The measurements were performed in a setup constructed in house that described in Chapter 2. In each FCS experiment the fluorescence fluctuations were recorded for 1-2 min. Free fluorescein ($D = 3.00 \times 10^{-10} \text{ m}^2 \cdot \text{s}^{-1}$)²¹⁵ was used for calibration.

UV-Vis measurement

UV-Vis spectra were measured in 1 cm light path disposable polystyrene cuvettes (Fisher) on a UV-Vis spectrophotometer (Shimadzu, UV-1800).

CHAPTER 5

STUDY OF INTERACTION OF META-LINKED POLY(PHENYLENE ETHYNYLENE) SULFONATE CONTAINING PYRIDINE WITH METAL IONS

Background

The strong photoluminescence and amplified quenching intrinsic to CPEs enable them to be ultrasensitive chemosensors for metal ions.^{16, 54, 91} The addition of oppositely charged small ions into solutions of CPEs has been reported to lead to significant changes in their photophysical properties.^{16, 42} Early studies found that some metal ions, such as Pd^{2+} and Ca^{2+} , exhibit an amplified quenching ability towards carboxylated poly(*p*-phenylene ethynylene)s (PPE) in aqueous solution.^{47, 216} The superior sensitive photophysical response of CPEs is attributed to a combination of several factors, including delocalization and rapid diffusion of the singlet exciton along the CPEs' backbone to the quencher "trap site", as well as the various interactions between CPEs and ions, such as electrostatic attraction, or chelation, through which the aggregation of CPEs may be induced.^{24, 42, 43} Consequently, a series of CPE based sensors for metal ions has been developed.^{47, 67, 216}

Pyridine has a strong binding affinity towards metal ions and many pyridine substituted macromolecules have been synthesized and developed for metal ion sensors in the past few years.^{56, 217-219} Bai and coworkers published a series of papers regarding development of pyridine derivative-containing conjugated polymer based sensing methods for Pd^{2+} or Pt^{2+} .²¹⁷⁻²¹⁹ Wang and coworkers also reported a fluorimetric detection method for copper ions using bipyridyl-substituted cationic CPEs.⁵⁶ As stated in Chapter 1 and 3, *meta*-linked PPEs have the tendency to form a helical structure in polar solvents stabilized by their amphiphilicity and π - π intramolecular stacking. Winter and Eisenbach have reported that *meta*-linked PPE provides flexibility and spatial

registry for three-dimensional molecular binding of analytical targets.²²⁰ By coupling in the pyridine units, the helical structure adopted by meta-linked CPE can be stabilized and enhanced by silver ions or H⁺.²²¹ Recently, Tan and Huang have designed an anionic CPE by combining *meta*- and *para*-linked pyridyl and phenylene ethynylene (PE) units into one polymer chain which shows high sensitivity and selectivity for silver ions.²²²

Palladium is capable of eliciting a series of cytotoxic effects which may cause severe primary skin and eye irritations.^{223, 224} Among the conventional analytical techniques used for palladium detection, such as atomic absorption spectrometry,²²⁵ plasma emission spectroscopy,²²⁶ X-ray fluorescence²²⁷ and inductively coupled plasma mass spectrometry (ICP-MS),²²⁸ colorimetric and fluorimetric based methods are expected to be more desirable due to their simplicity and ultrasensitivity.^{217, 218, 229-232} Particularly, conjugated polymer (CP) based sensors have attracted much attention.^{217, 218, 230}

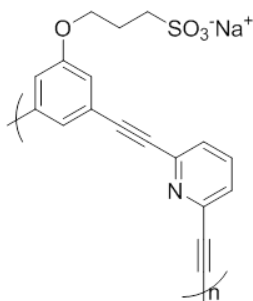


Figure 5-1. Structure of mPPESO₃py.

In this chapter, a sulfonated poly(phenylene ethynylene) (PPE) containing *meta*-linked pyridine rings in the polymer backbone (mPPESO₃py, Figure 5-1) is investigated. A solvent-induced change in photophysics is observed, suggesting a coil-helix conformation transition and an electron donor-acceptor complexation. By incorporating

the *meta*-substituted monopyridyl units, the spatial matching for selective binding is improved. Particularly, the photophysical study indicates that the strong chelation of Pd^{2+} with pyridine rings rearranges and stabilizes the helical conformation of mPPESO₃py. Moreover, Pd^{2+} ion shows overwhelming amplified quenching ability over other metal ions towards mPPESO₃py, giving rise to a novel type of Pd^{2+} sensor that overcomes the water insolubility drawback of CPs. FCS studies show that upon addition of Pd^{2+} to an mPPESO₃py solution, a poor correlation of the emission signal and a shorter diffusion time for mPPESO₃py are observed. These phenomena are presumably due to the formation of a more compact conformation for mPPESO₃py with Pd^{2+} via chelation as well as the low quantum yield for mPPESO₃py due to amplified quenching, which leads to fast fading of photons emitted by a single polymer chain. Longer diffusion time is observed for mPPESO₃py mixed with various other multi-valence ions, particularly, Fe^{3+} and Cr^{3+} , which is the result of aggregation induced by the binding between metal ions and the nitrogen atoms belonging to adjacent CPE chains. Nevertheless, electron transfer and high binding affinity between CPEs and metal ions are the dominant factors in the amplified quenching mechanism.

Results and Discussion

Photophysical Properties of mPPESO₃py

Solvent-induced photophysics change

In previous work, a *meta*-PPE was reported to adopt a random-coil conformation in a “good solvent” such as methanol (MeOH). In a polar solvent, such as acetonitrile and water, the polymer chain collapses into a π -stacking helical conformation to minimize solvent-backbone contacts while maintaining favorable solvent/side-chain interactions for solvation.⁵¹⁻⁵³ This conformational transition is reflected in the UV-Vis

absorption spectrum. Figure 5-2A shows the spectra for mPPESO₃py in MeOH titrated with water. The absorption spectrum of mPPESO₃py features two absorption bands at 387 nm and 306 nm in MeOH, both of which decrease and slightly red-shift when the volume percentage of water increases in the solvent mixture. These changes in spectra are similar to that of *meta*-oligo(phenylene ethynylene) when the random-coil to helix conformation transition occurs.⁵¹⁻⁵³ Figure 5-2B plots the ratio of the two absorption peaks (A_L/A_S , A_L and A_S are the absorbance at longer and shorter wavelength peaks, respectively) as a function of the volume concentration of water in the mixed solvents. A general decrease in the ratio is observed with increasing content of water, suggesting the coil-helix conformation transition has more impact on the absorbance at longer wavelength, which is consistent with the observation reported in the literature.⁵¹⁻⁵³

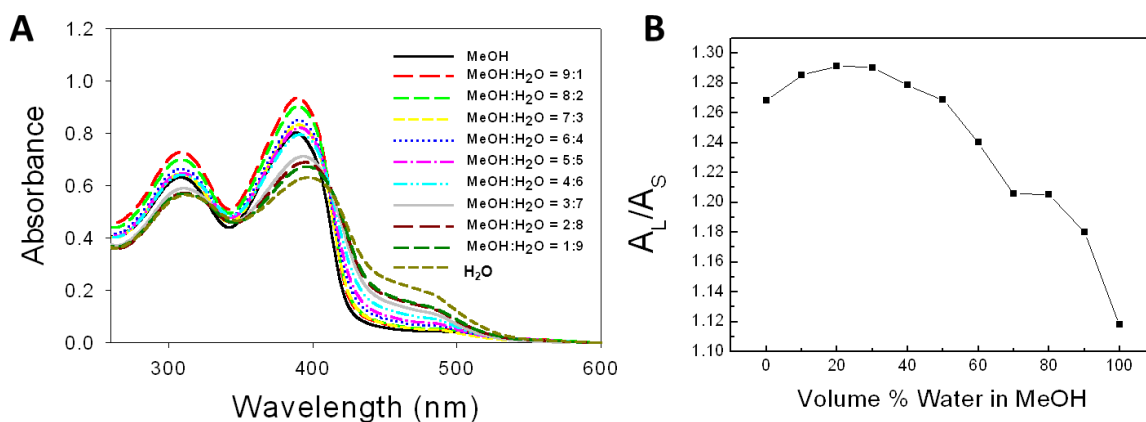


Figure 5-2. A) Absorption spectra for mPPESO₃py in solvent mixture with different component volume ratio. B) Ratiometric plot of A_L/A_S versus the percentage of water in methanol. A_L and A_S are the absorbance at longer and shorter wavelength peaks, respectively.

Note that a broad shoulder peak appears at 450-500 nm and increases with increasing volume fraction of water in the solvent, this band may be due to a charge-transfer absorption, which is similar to the spectra observed in the donor-accepter system.^{233, 234} The helix theoretically contains six aromatic members per helical turn with

π - π stacking between two identical aromatic rings, e.g., pyridyl-pyridyl. However, during the folding process of the coil-helix transition, a twist may occur due to the mismatch in the size of functional groups or steric hindrance, bringing electron-rich alkoxy substituted phenyl and electron-deficient pyridyl units in close proximity, where a donor-acceptor interaction between them takes place. As illustrated in Figure 5-3A, the solvophobicity and π - π stacking drives mPPESO₃py to adopt a helical conformation in water; while the pyridyl-phenyl interaction further stabilizes the helical structure, although it twists the helical circle. As more water is added into the mixture, more random coils tend to fold into helices and more pyridyl-phenyl pairs are involved in the complexation, thus enhancing the intensity of the shoulder peak in the spectrum.

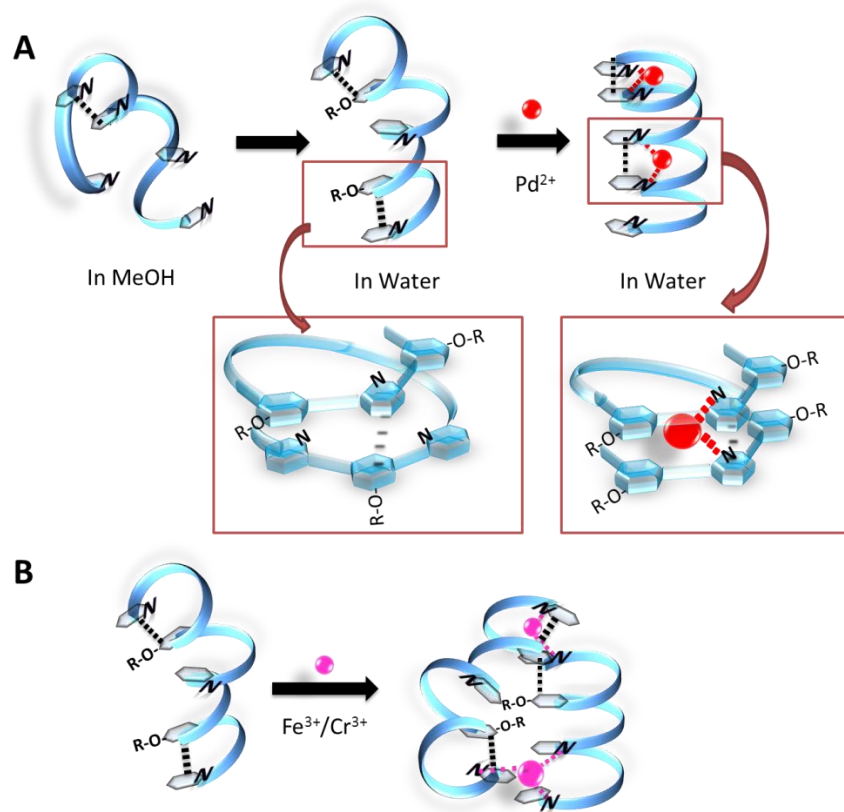


Figure 5-3. A) Mechanism of solvent- and metal ion-induced formation of helical structures. B) Mechanism of multi-valence metal ion-induced crosslinking of CPE.

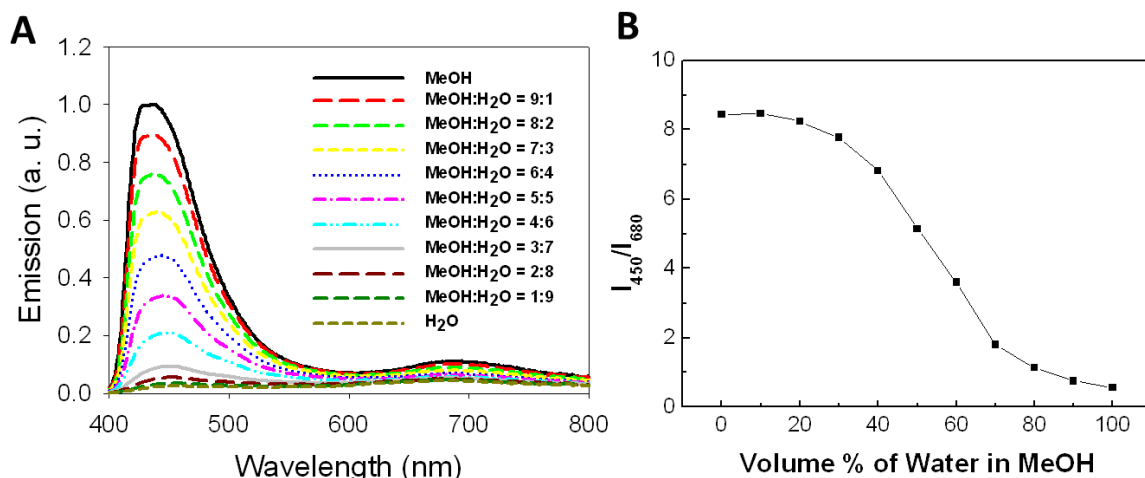


Figure 5-4. A) Emission spectra for mPPESO₃py in solvent mixture with different component volume ratio. B) Absorbance ratio of two bands versus the percentage of water in MeOH.

The solvent induced changes in emission spectra as a function of solvent are shown in Figure 5-4A. In a good solvent, mPPESO₃py features two bands with a pronounced high peak at ~450 nm and a structureless broad band around 680 nm. The 450 nm band is likely to be the emission from a relatively localized excited state. The broad band in the low energy region may emanate from an excimer-like excited state, attributed to the π -stacking hydrophobic interaction or donor-acceptor complexation.⁵¹ As more and more water is added into the solution, quenching is much more pronounced for the shorter wavelength band. A plot of I_{450}/I_{680} as a function of percentage of water in the mixture is displayed in Figure 5-4B. As expected, the ratio decreases as the volume of water in the composition increases, which corresponds to the folding process of the polymer chain undergoing a coil-helix transition.

Palladium ion-induced photophysics change

A titration of Pd²⁺ to the mPPESO₃py aqueous solution was conducted. The two absorption peaks continue to decrease and red shift, which are ascribed to the electron density change caused by the complexation of metal ions or conformational changes in

the polymer's backbone as a result of the chelation.²³⁵ The A_L/A_S keeps decreasing from 1.12 to 0.91, indicating an advanced folding process that further enhances the helical conformation (Figure 5-5B). A plausible mechanism is illustrated in Figure 5-3A: when Pd^{2+} is present, the chelation between two Ns and one Pd^{2+} causes more random coil portion to undergo coil-helix transformation. Meanwhile, the high binding affinity between N and Pd^{2+} makes the “spring-like” helical coil pressed more with Pd^{2+} as the “clip”, disrupts the charge-transfer phenyl-pyridyl interaction and rearranges the stacking of the aromatic rings, e.g., pyridyls pairing with pyridyls instead of phenyls. The closely packed core with relatively narrow helical angle enhances the π - π stacking hydrophobic interaction, leading to the further decrease and red-shift in the absorption peak as observed. The rearrangement in the helical packing structure can be evidenced by the gradual disappearance of the shoulder peak in the region of 450-500 nm (Figure 5-5A).

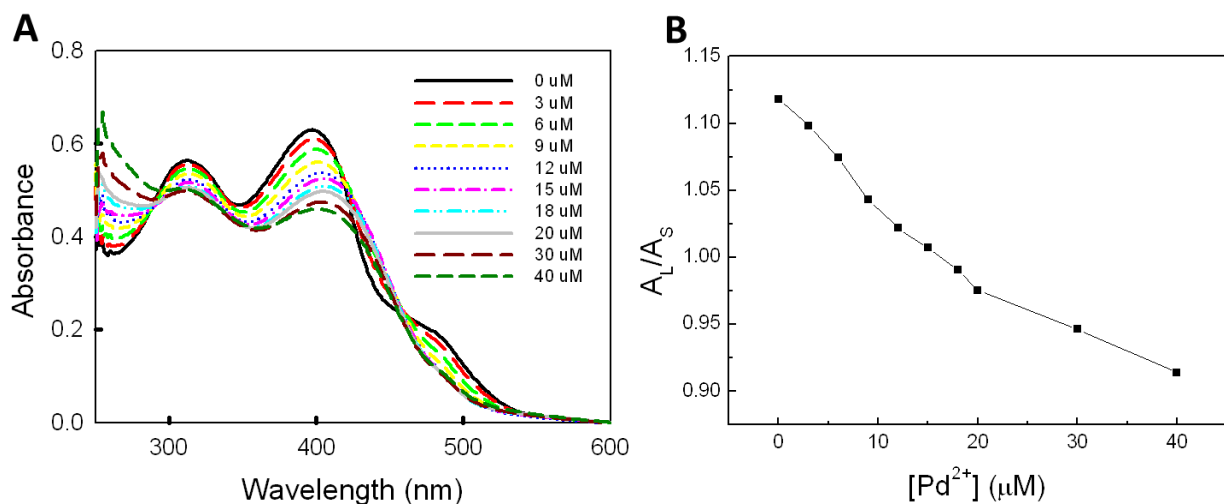


Figure 5-5. A) Absorption spectra of 15 μM mPPESO₃py titrated with Pd^{2+} . B) The absorbance ratio of two bands versus the concentration of Pd^{2+} in aqueous solution (A_L and A_S are the absorbance at longer and shorter wavelength peaks, respectively).

The quenching behavior of Pd^{2+} on the emission of mPPESO₃py is displayed in Figure 5-6 (The sharp peak around 780 nm is the second-order scattering for the

excitation beam at 390 nm). A dramatic decrease in the emission peak is observed as the $[\text{Pd}^{2+}]$ increases from 0 to 40 μM . As $[\text{Pd}^{2+}]$ reaches 30 μM , the emission of 15 μM mPPESO₃py is almost quenched and the shoulder band in the absorption spectrum disappears, suggesting the saturation of the metal-pyridyl complexation at this concentration.

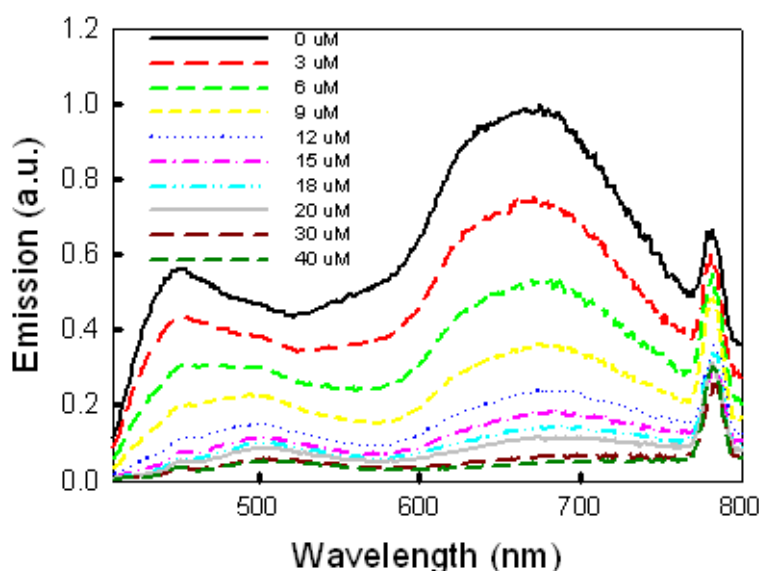


Figure 5-6. Emission spectra for 15 μM mPPESO₃py with various $[\text{Pd}^{2+}]$ in aqueous solution. The sharp peak shown up around 780 nm is the second-order scattering for the excitation beam at 390 nm.

Photophysics change of mPPESO₃py with various metal ions

High quenching efficiency of Pd^{2+} towards mPPESO₃py is evidenced when compared to other metal ions, including Cu^{2+} , Fe^{3+} , Cr^{3+} , Fe^{2+} , Li^+ , Ag^+ , Ca^{2+} , Zn^{2+} , and Mg^{2+} . Figure 5-7 and Figure 5-8 display the Stern-Volmer plots and K_{SV} bar graph for the polymer with different metal ions in water. Pd^{2+} has the highest $K_{SV} = 2.50 \times 10^5 \text{ M}^{-1}$ of all the metal ions and is ~4 times greater than that of Cu^{2+} , which has the second highest K_{SV} . The selectivity of mPPESO₃py for Pd^{2+} can be evaluated in the bar graph (Figure 5-9), where 15 μM Pd^{2+} can greatly quench 15 μM of the polymer with I/I_0 ratio >

3 times higher than that of the other metal ions at the same concentration. As the concentration of Metal ions increases, the selectivity of mPPESO₃py for Pd²⁺ over other metal ions becomes greater, which paves a promising avenue for Pd²⁺ sensor development.

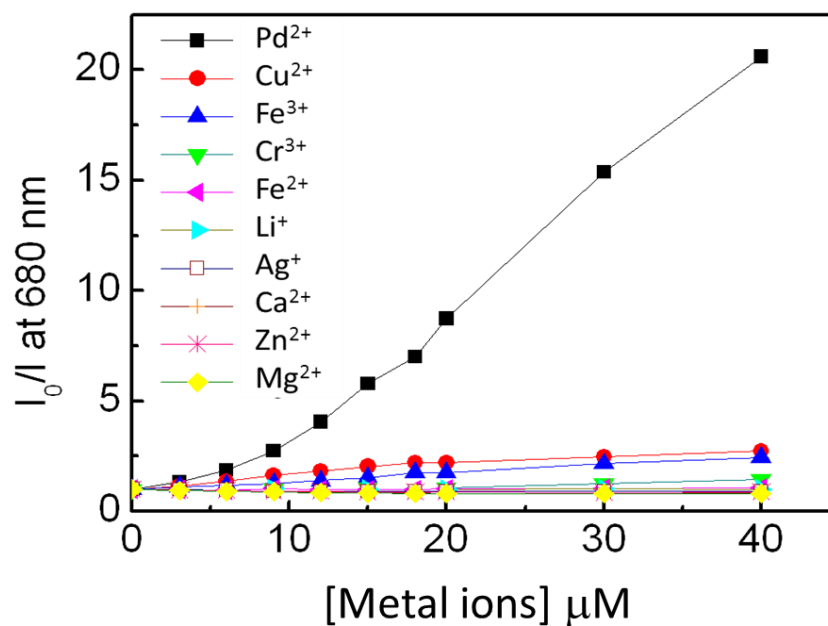


Figure 5-7. Stern-Volmer plots for mPPESO₃py with various metal ions in water.

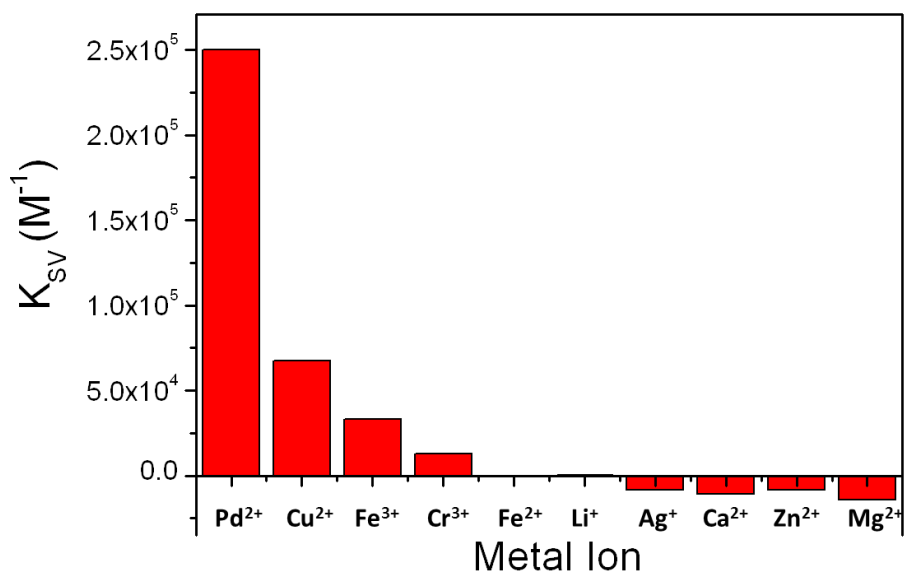


Figure 5-8. Stern-Volmer constant for various metal ions in water.

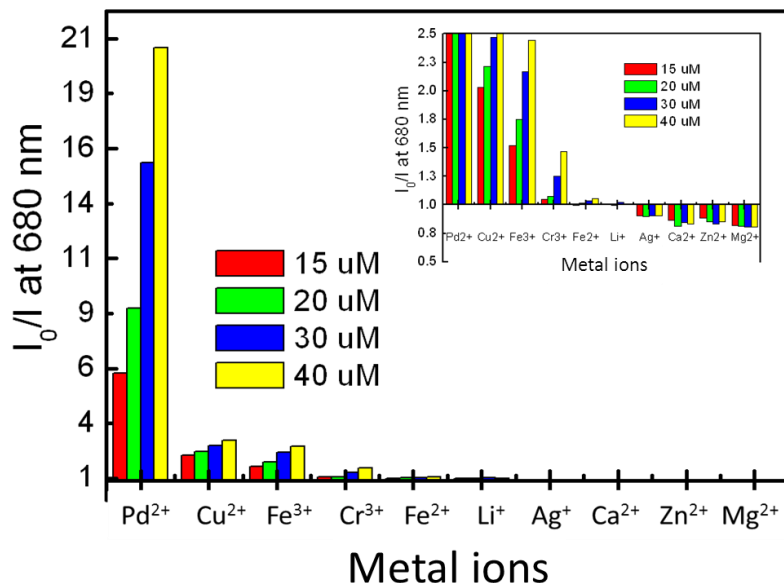


Figure 5-9. Bar graph for fluorescence quenching ratios I_0/I at 680 nm of mPPESO₃py with different metal ions at various concentrations in aqueous solution. Insert: Enlargement of lower I_0/I region. I_0 and I are the emission intensity of mPPESO₃py without and with metal ions, respectively.

FCS Study on the mPPESO₃py with Various Metal Ions

To gain more insight into the intermolecular interaction induced by metal ions, the FCS technique has been used to detect the diffusion behavior change of mPPESO₃py with and without metal ions. The diffusion time of pure polymer (15 μM) in aqueous solution is 1.39×10^{-4} s (Figure 5-10A). Upon titration with Pd^{2+} from 10 μM -50 μM , the correlation curves for the polymer become noisier at a fixed photon recording time (2 min), which are poorly fitted with fitting coefficient $\sim 84\%$ when Equation 2-2 is applied (Figure 5-10A). Recall that the correlation of the fluorescence fluctuation is accomplished by calculating the similarity between a signal $F(t)$ and a replicate of the same signal but shifted by a time lag τ , $F(t+\tau)$. Only when the two sets of signal $F(t)$ and $F(t+\tau)$ are identical, i.e., produced by the same molecule, that the similarity/correlation of signal will reach the maximum. Once the polymer chain diffuses out of the excitation

volume after its characteristic diffusion time τ_D , the correlation is greatly reduced. However, when the quencher molecules are introduced, its efficient quenching ability largely reduces the number of photons emitted by a single polymer chain or aggregate, which makes detection of the signal for the photon counting device much more difficult, resulting in a poor correlation curve. A smooth correlation curve and good fitting still can be obtained when the FCS photon recording time is largely extended, e.g., to 30 min. A decrease in diffusion time is observed as the concentration of Pd^{2+} increases (Figure 5-11). There are two possible reasons for the apparent fast diffusion. The first is failure in detecting the second photon signal that is generated by the same polymer chain/aggregate due to amplified quenching, which produces a false appearance that the polymer chain has already diffused out of the excitation volume. The second is the chelation between pyridine and Pd^{2+} compacts the conformation of mPPESO_3py , which decreases the hydrodynamic radius and accelerates the diffusion of the CPE (Figure 5-3A).

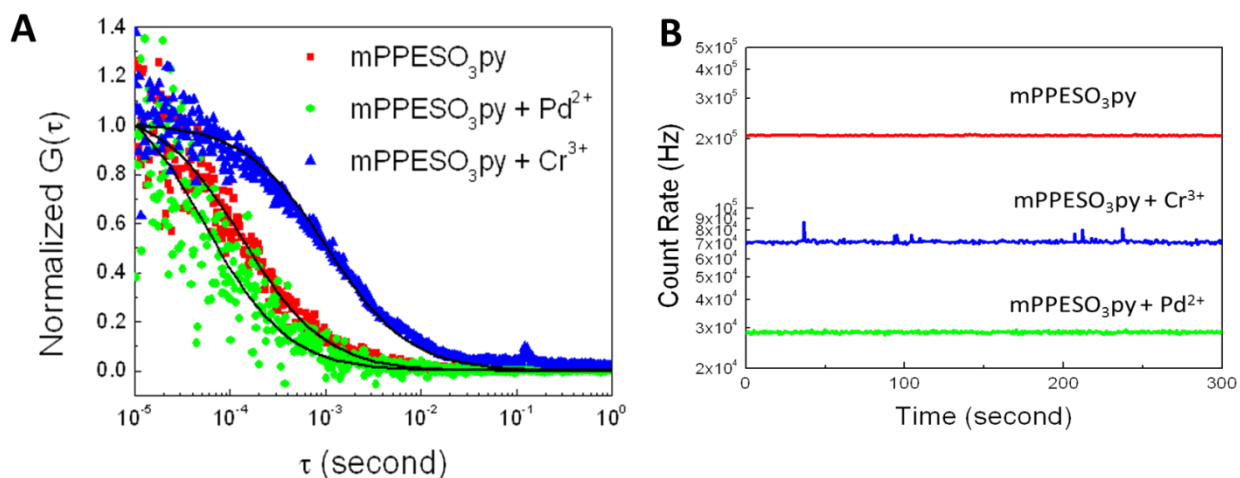


Figure 5-10. A) FCS correlation curves and B) fluctuation profiles for 15 μM mPPESO_3py without (red) and with 40 μM Pd^{2+} (green) or Cr^{3+} (blue) in aqueous solutions. Black lines in A are the single-species fitting curves.

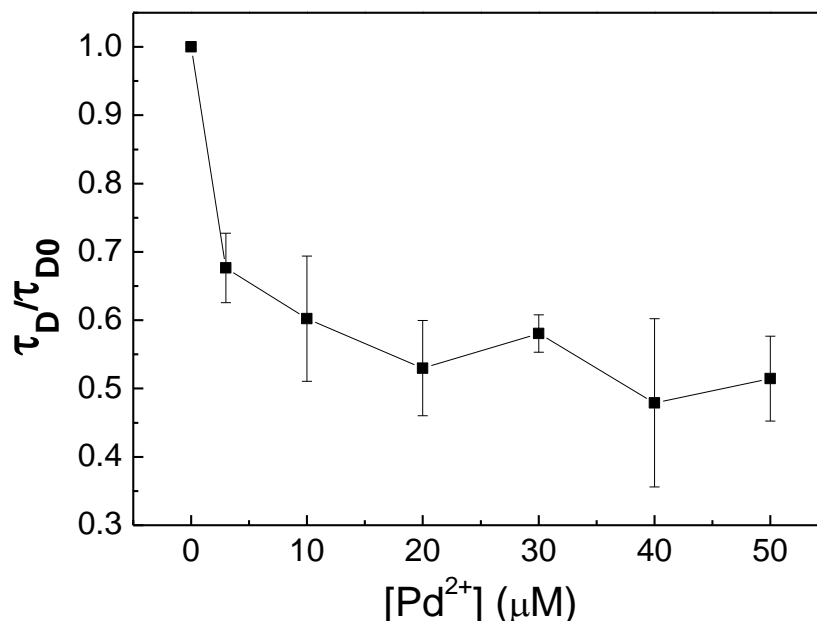


Figure 5-11. Diffusion time ratio for mPPESO₃py with different amount of Pd²⁺ measured for 30 min in aqueous solution. τ_D and τ_{D0} are the diffusion time of mPPESO₃py with and without Pd²⁺, respectively.

More FCS experiments have been done for the CPE with other metal ions. As shown in Figure 5-12, upon addition of 40 μM Cr³⁺, 15 μM mPPESO₃py undergoes large aggregation with $\tau_d / \tau_{d0} \sim 7$, where τ_{d0} and τ_d are the diffusion time of mPPESO₃py without and with Cr³⁺, respectively. A relatively smooth correlation curve can be found in Figure 5-10A (fitting coefficient $\sim 99\%$). Several spikes show up in the fluctuation profile in Figure 5-10B, indicating the formation of large aggregates. Fe³⁺ can also induce aggregation with $\tau_d / \tau_{d0} \sim 6.5$, followed by Fe²⁺ ($\tau_d / \tau_{d0} \sim 2$) and Cu²⁺ ($\tau_d / \tau_{d0} \sim 1.4$). Triply charged ions seem have higher capability for aggregation induction, which is probably due to their ability to bind three pyridyl moieties belonging to different polymers to induce interchain crosslinking as depicted in Figure 5-5B.

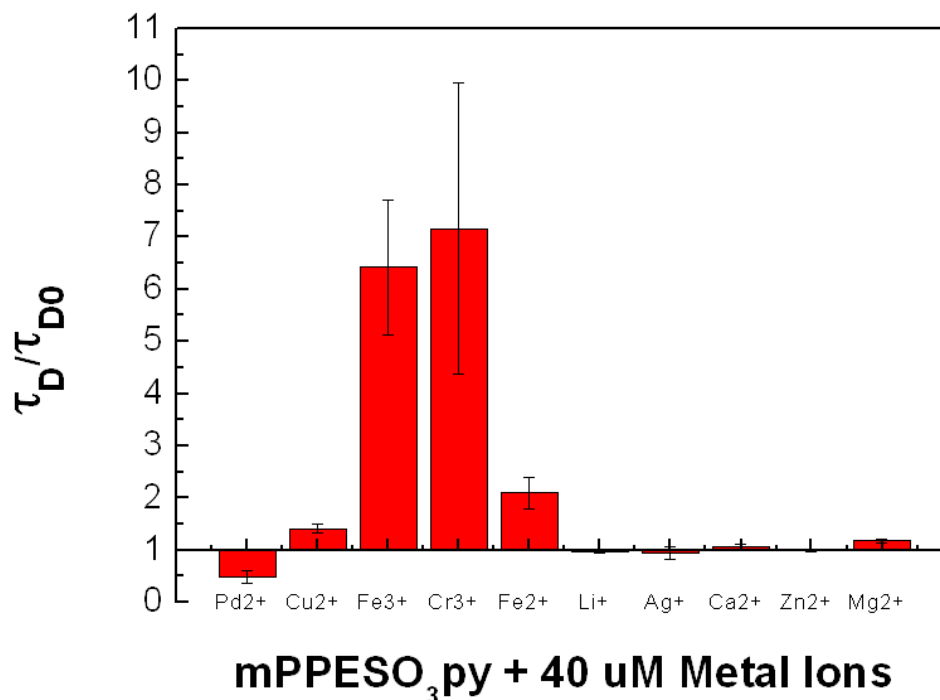


Figure 5-12. Diffusion time ratio of mPPESO₃py before and after the addition of metal ions. τ_D and τ_{D0} are the diffusion time of CPE with and without metal ion, respectively. [mPPESO₃py] = 15 μ M, [metal ion] = 40 μ M.

Although aggregation is one of the mechanisms that cause amplified quenching of CPEs,^{28, 103} it is not the dominating factor in this system. As shown in Figure 5-12 and Figure 5-8, even though Cr³⁺ possesses highest cross-linking ability, it has a relatively low quenching efficiency. The quenching ability of copper ions is second best compared to palladium ions; however, it can only induce slight aggregation in CPEs. Charge transfer from the electron-rich conjugated backbone to the electron-deficient metal ions as well as the high coupling affinity between the pyridine moiety and multi-valent ions are the dominant effects in the amplified quenching process.

Summary

In summary, the solvent-induced coil-helix transition on the *meta*-linked anionic CPE containing monopyridyl units is investigated. Changes in the photophysical

properties provide evidence for the conformational alteration of the CPE as well as the donor-acceptor complexation in the helix. On the basis of the spectroscopic study, Pd^{2+} induced rearrangement and tighter compaction in helical rings of the polymer backbone are revealed. The quenching efficiency of Pd^{2+} overwhelms other metal ions, giving rise to a Pd^{2+} sensing strategy. The FCS study shows that although the triply charged ions (Fe^{3+} , Cr^{3+}) can induce interchain crosslinking, aggregation is not the dominant factor in the amplified quenching behavior. Charge transfer and high binding affinity between CPEs and metal ions play essential roles in the quenching phenomenon.

Experimental

Materials

mPPESO3py was synthesized according to previous report.¹⁹⁶ Solutions of metal ions were prepared from their chloride salts, except for AgNO_3 and FeSO_4 . With the exception of PdCl_2 , all metal sample solutions were prepared by using water that was distilled and purified by a Millipore purification system (Millipore Simplicity Ultrapure Water System). A stock solution of PdCl_2 was prepared in dimethylsulfoxide (DMSO). The polymer stock solution was diluted with water or methanol to a final concentration of 15 μM . All concentrations of polymers are provided in polymer repeat unit (PRU) concentration.

Instrumentation

Absorption and Emission measurement

Absorption spectra were obtained on a Varian-Cary 100 UV-Vis absorption dual beam spectrophotometer. Steady state fluorescence spectra were recorded on a spectrofluorometer from Photon Technology International and corrected by using correction factors generated with a primary standard lamp.

FCS measurements

The measurements were performed in a setup constructed in house that is described in Chapter 2. In each FCS experiment the fluorescence fluctuations were recorded for 5-30 min. Free TMR ($D = 2.88 \times 10^{-10} \text{ m}^2 \cdot \text{s}^{-1}$)¹⁴³ was used for calibration.

CHAPTER 6 CONCLUSION

The water solubility and π -conjugated backbones endow conjugated polyelectrolytes (CPEs) favorable optical properties, charge interaction ability and solvent-dependent self-assembly. This class of polymers has been studied for chemical and biological sensing applications due to their superior signal amplification and increased sensitivity compared to other molecular dyes.

Fluorescence correlation spectroscopy (FCS), developed from a fluorescence microscope, is a powerful single-molecule spectroscopic technique, which utilizes the fluctuations in emission (caused by Brownian diffusion, flow, chemical reactions, etc.) from fluorescent molecules moving in and out of a microscopic confocal volume (~femtoliters). By employing FCS, the diffusion behavior, concentration, conformation/size change of fluorescence molecules, particularly, CPEs, can be monitored directly, so that a number of events, including chemical reaction, mobility, molecular interaction, self-assembly, or binding kinetics, can be detected.

The Application of Dye-Ligand Intercalated Helical Conjugated Polyelectrolyte to Protein Sensing

As described in Chapter 3, a DNA intercalator biotin-tetramethylrhodamine (biotin-TMR) is found to be capable of intercalating into a helical conjugated polyelectrolyte (Poly-1). The efficient fluorescence resonance energy transfer (FRET) from the polymer to the TMR chromophore is observed; however, the addition of avidin to the poly-1/biotin-TMR intercalation complex results in no emission recovery of Poly-1. The mixing of biotin-TMR with avidin prior to the addition of the polymer can efficiently disrupt the FRET signal. The study of the FRET response as a function of [avidin]/[biotin-TMR] affords insight into the interaction of the protein with the

intercalation complex and reveals the so-called phenomenon steric constraint. This project is further studied by FCS coupled with 543 nm laser. A remarkable increase in the diffusion time of Poly-1/biotin-TMR complex in the presence of avidin is observed. This change is attributed to the formation of large supramolecular polymer aggregates induced by the binding between the biotin units of intercalators and avidin, which gives rise to a novel sensing strategy for avidin. The detection limit of <100 pM is figured out, which is lower than that of most other avidin sensing methods reported.

New Fluorescence Correlation Spectroscopy and Application on Protein Sensor Array Development

In Chapter 2, a new FCS system coupled with 405 nm blue laser, which can directly track the diffusion of blue-emitting CPEs, is successfully constructed. Details about the theory and construction of FCS are fully discussed. This new FCS is further demonstrated its power and feasibility in Chapter 4, where a CPE-based protein sensor array is developed. Six CPEs with various structures and charge properties are exposed to seven proteins. Upon hydrophobic or electrostatic interactions, the aggregation states of CPEs in aqueous solution change, which results in the change of the diffusion behavior of the CPEs. The diversity in structure characteristics, interaction properties and the molecular scales of both polymers and proteins contribute to the variation of the final molecular size and diffusion behavior of probes, which can be recorded by FCS. The resulting data matrix is analyzed by linear discriminant analysis (LDA). The 3D signal response pattern created through LDA demonstrates the discrimination ability of this sensor array for seven proteins. The success in identification of unknown samples further verifies the feasibility of this new sensor array.

Study of *meta*-Linked Poly(Phenylene Ethynylene) Sulfonate Containing Pyridine Quenched by Metal Ions

The changes in photophysical properties of an mPPESO₃py, which is a CPE containing meta-linked pyridine rings in the backbone in various conditions are investigated. Based on the spectra, the electron donor-acceptor complex is formed between alkoxy substitute phenyl and pyridyl during coil-helix transition driven by solvophobicity and π - π stacking interaction. The polymer shows a great affinity and selectivity for the Pd²⁺ ion for the quenching efficient of Pd²⁺ greatly surpasses that of the other metal ions. FCS study further reveals that some multivalent metal ions including Cr³⁺, Fe³⁺, Fe²⁺, and Cu²⁺ can induce aggregation of mPPESO₃py due to the crosslinking between metal ions and Ns belonging to adjacent polymers. Failure in getting smooth correlation curve for polymer with Pd²⁺ is due to its compact conformation and low quantum yield which significantly affect the photon detection. The quenching mechanism is dominated by the photoinduced electron transfer (PET) process or energy transfer (ET) process instead of conformational change of mPPESO₃py.

Outlook for Application of FCS in CPE

In this dissertation, the FCS has successfully extended its application in the CPE field, providing insights into the physical state change of CPE and their interaction with other molecules from a molecular motion aspect, which cannot be explored by conventional technologies. By combining FCS with CPE, a novel platform for development of molecular sensing methods has been established, showing its potential and specificity. As CPE-FCS based biomolecule sensing methods are just proposed and initialized, further development can be made by optimizing the CPE probes

including modifying the molecular weight distribution and quantum yield of polymers, conjugating more versatile functional groups to the backbone. Sensing assays for some potential analytes other than proteins, such as ssDNA and dsDNA, can be designed and tested. Moreover, the development of these sensing assays in more complicated biological environments is necessary, so that the potential interference can be eliminated and their feasibility in the real world can be enhanced.

For the FCS setup, a temperature controlling accessory may be installed on the sample holder to achieve CPE-based enzyme activity sensing, which requires a temperature higher than room temperature. In addition, if one more set of detector is introduced in, by applying different band pass emission filters, the study of fluorescence resonance energy transfer can be conducted. A cross-correlation of the emission signals can also be achieved by just upgrading the correlator.

Besides the application on the biosensors discussed above, some fundamental research can be carried out on the interactions between CPEs and other molecules such as small ions, surfactants or between different CPEs. If an organic-solvent resisted container is used, such as quartz sample well, the investigation of polymers can be done in organic solvents, which has many benefits for those conjugated polymers that have poor water solubility.

APPENDIX A
TABLES OF TRAINING DATA

Table A-1. Training matrix of Log (τ_d/τ_0) of six CPE sensor array (P1 – P6) against seven proteins (1 = avidin, 2 = LYZ, 3 = HRP, 4 = PLD2, 5 = HK3, 6 = BSA, 7 = GOx) with [CPE] = 500 nM and [protein] = 2 μ g/mL in 5 mM HEPEs buffer, pH 7.2, room temperature.

P1	P2	P3	P4	P5	P6	Protein #
1.015	0.856	0.886	0.013	-0.007	0.183	1
1.105	0.610	0.798	0.026	-0.075	0.542	1
1.356	0.762	0.344	0.096	-0.080	0.372	1
0.978	0.659	0.901	0.014	0.047	0.006	1
0.911	1.010	0.703	0.025	0.001	-0.020	1
0.645	1.173	0.712	-0.011	-0.049	-0.068	1
0.711	0.705	0.710	0.045	0.198	-0.121	1
0.778	0.565	0.775	-0.054	0.057	0.215	1
0.807	0.765	0.737	0.054	0.003	0.511	1
1.192	0.890	0.680	-0.040	-0.055	0.512	1
0.572	0.864	0.981	0.110	-0.025	-0.163	1
0.988	0.699	0.772	0.034	-0.102	0.266	1
1.057	0.986	0.782	0.035	-0.075	-0.089	1
0.279	0.639	0.627	-0.004	-0.034	-0.162	1
0.236	0.622	0.564	0.021	-0.103	-0.032	1
0.737	0.926	0.612	0.098	-0.021	-0.036	1
0.309	0.635	0.601	0.162	-0.065	-0.244	1
0.289	0.656	0.560	0.116	-0.039	-0.099	1
0.438	0.831	0.514	0.132	-0.154	-0.334	1
0.752	0.787	1.050	-0.009	-0.134	0.010	1
0.814	3.762	0.290	0.042	-0.053	0.656	2
1.072	2.144	0.553	0.036	-0.059	-0.110	2
1.080	2.755	0.828	0.035	-0.495	0.029	2
1.003	2.887	0.653	0.000	-0.049	-0.004	2
1.473	2.886	0.696	0.089	-0.027	0.161	2
0.796	2.298	0.894	-0.011	-0.026	0.402	2
0.439	2.125	0.473	0.063	-0.044	-0.098	2
0.318	2.431	0.913	0.012	0.007	-0.116	2
0.850	2.263	1.302	0.014	0.233	0.178	2
1.117	3.221	0.836	-0.006	0.253	-0.071	2
1.030	3.363	1.171	-0.003	0.248	0.542	2
1.234	2.458	1.107	0.046	0.247	0.439	2
1.494	3.068	0.365	0.208	0.249	0.020	2
1.733	3.061	1.345	0.047	0.244	-0.040	2
1.561	3.735	1.325	0.055	0.377	-0.038	2
1.572	2.153	0.811	0.051	0.221	-0.003	2
1.176	3.522	0.876	0.062	0.010	-0.114	2

Table A-1. Continued.

P1	P2	P3	P4	P5	P6	Protein #
1.564	3.816	1.273	0.065	-0.057	-0.106	2
1.621	3.149	0.639	0.071	0.401	-0.135	2
0.669	3.263	1.099	0.015	0.028	0.154	2
-0.013	-0.384	-0.107	1.727	-0.278	0.605	3
0.045	-0.374	-0.041	1.799	1.842	0.467	3
0.043	-0.468	-0.099	-0.126	2.301	0.450	3
-0.032	-0.401	-0.009	1.369	2.201	0.574	3
-0.079	-0.383	-0.124	0.117	-0.029	0.333	3
0.043	-0.492	-0.110	0.311	-0.030	0.640	3
-0.049	-0.378	-0.129	1.281	-0.098	0.454	3
-0.010	-0.434	-0.124	0.222	0.427	0.494	3
-0.040	-0.409	-0.161	0.251	-0.008	0.909	3
-0.002	-0.349	-0.120	1.638	-0.073	0.921	3
-0.003	-0.391	-0.125	1.016	1.232	0.894	3
-0.045	-0.373	-0.125	0.411	0.047	0.579	3
0.050	-0.482	-0.047	1.509	-0.036	0.594	3
0.057	-0.416	-0.083	-0.048	0.187	0.275	3
0.094	-0.426	-0.141	-0.067	0.039	0.150	3
-0.029	-0.497	-0.106	-0.043	-0.068	0.117	3
-0.026	-0.496	-0.137	-0.121	0.014	0.345	3
0.000	-0.545	-0.129	-0.186	-0.052	0.571	3
-0.021	-0.419	-0.010	-0.040	-0.034	0.728	3
-0.069	-0.349	-0.104	0.088	-0.096	0.486	3
0.035	-0.261	-0.024	1.409	3.191	0.750	4
0.023	-0.262	-0.032	1.422	2.995	1.101	4
0.026	-0.333	-0.022	1.149	2.588	0.946	4
-0.002	-0.389	-0.051	1.275	2.019	0.832	4
0.032	-0.362	-0.103	1.609	2.608	0.837	4
0.004	-0.421	-0.041	1.499	1.469	0.821	4
0.021	-0.350	-0.066	1.018	3.190	0.942	4
-0.050	-0.084	-0.071	1.582	3.354	0.701	4
0.023	-0.112	-0.060	2.090	2.345	0.753	4
-0.065	-0.158	-0.088	1.951	1.804	0.790	4
-0.013	-0.151	-0.088	1.470	1.269	0.807	4
-0.040	-0.122	-0.042	2.012	1.272	0.747	4
0.001	-0.064	-0.112	2.226	1.230	0.919	4
0.022	-0.156	-0.118	1.452	3.022	0.809	4
0.009	-0.212	-0.140	2.065	1.396	0.769	4
-0.011	-0.307	-0.141	1.112	1.739	0.695	4
0.024	-0.220	-0.132	1.468	1.460	0.753	4
0.029	-0.157	-0.135	1.688	1.603	1.212	4
0.018	-0.145	-0.144	1.681	2.945	1.012	4
0.005	-0.102	-0.075	1.216	3.124	0.628	4

Table A-1. Continued.

P1	P2	P3	P4	P5	P6	Protein #
-0.069	-0.269	-0.169	1.199	1.788	0.998	5
-0.030	-0.254	-0.130	0.816	1.110	0.972	5
-0.083	-0.213	-0.200	1.360	1.857	0.934	5
-0.023	-0.286	-0.188	0.926	1.312	1.031	5
-0.040	-0.303	-0.191	1.002	1.320	1.019	5
-0.029	-0.223	-0.308	1.173	0.778	1.587	5
-0.019	-0.314	-0.248	1.614	1.312	0.813	5
-0.042	-0.330	-0.228	0.973	1.193	1.178	5
0.000	-0.165	-0.327	0.834	0.912	1.160	5
-0.086	-0.213	-0.258	1.220	1.355	1.090	5
-0.011	-0.194	-0.288	1.450	0.749	0.622	5
0.016	-0.255	-0.301	0.794	1.544	1.301	5
0.026	-0.265	-0.105	0.886	0.350	1.390	5
0.000	-0.072	-0.053	1.796	0.970	1.203	5
-0.070	-0.143	-0.050	1.720	1.628	0.985	5
-0.034	-0.137	-0.039	0.988	1.286	1.107	5
-0.081	-0.098	0.045	1.095	0.896	1.163	5
-0.019	-0.103	-0.095	1.304	1.139	1.323	5
-0.047	-0.034	-0.117	1.789	1.492	0.938	5
-0.031	-0.145	-0.111	0.713	1.575	1.170	5
0.058	-0.106	-0.239	1.482	1.606	0.882	6
0.027	-0.127	-0.262	1.124	1.732	0.678	6
-0.012	-0.217	-0.260	1.266	2.590	0.592	6
-0.014	-0.142	-0.244	0.916	1.191	0.730	6
0.031	-0.121	-0.266	1.502	1.588	0.649	6
0.035	-0.125	-0.278	0.828	1.493	0.799	6
-0.025	-0.091	-0.113	1.166	2.036	0.665	6
-0.008	-0.123	-0.164	1.229	1.994	0.578	6
-0.049	-0.108	-0.199	0.857	2.194	0.584	6
-0.032	-0.094	-0.113	1.228	0.856	0.684	6
-0.036	-0.120	-0.132	1.234	1.045	0.717	6
-0.079	-0.148	-0.175	1.363	2.103	0.843	6
-0.003	0.002	-0.202	1.122	0.884	0.816	6
-0.014	-0.111	-0.182	0.625	1.218	0.612	6
0.010	-0.050	-0.144	0.837	1.343	0.863	6
-0.066	-0.058	-0.083	0.998	1.165	0.572	6
0.029	-0.109	-0.137	0.859	1.528	0.593	6
0.030	-0.108	-0.150	0.723	1.089	0.595	6
0.030	-0.192	-0.267	1.260	1.013	0.452	6
-0.026	-0.161	-0.122	1.044	1.097	0.757	6
-0.039	-0.068	-0.033	2.364	0.678	0.455	7
-0.053	-0.165	-0.018	2.890	0.776	0.507	7
0.024	-0.142	-0.051	2.605	0.869	0.483	7

Table A-1. Continued.

P1	P2	P3	P4	P5	P6	Protein #
-0.039	-0.132	-0.038	3.150	0.710	0.503	7
0.033	-0.143	-0.090	2.383	0.933	0.484	7
0.066	-0.205	-0.045	2.823	0.707	0.481	7
-0.045	-0.143	-0.043	2.252	0.734	0.426	7
0.017	-0.180	-0.054	2.461	0.779	0.624	7
0.058	-0.126	-0.033	2.942	1.224	0.781	7
-0.060	-0.008	-0.049	2.222	0.992	0.446	7
0.012	-0.080	-0.023	1.926	0.737	0.441	7
0.026	-0.036	0.058	1.892	0.722	0.721	7
-0.091	-0.041	0.052	1.788	0.861	0.443	7
-0.038	0.016	0.037	1.564	1.185	0.402	7
-0.079	-0.024	0.060	3.100	0.697	0.254	7
-0.014	-0.102	0.078	3.172	0.890	0.243	7
-0.085	-0.077	0.064	3.291	0.873	0.361	7
-0.083	-0.116	0.056	2.947	1.314	0.443	7
-0.069	-0.046	0.056	3.369	1.061	0.450	7
0.009	0.018	0.025	3.313	0.829	0.380	7

APPENDIX B
TABLE OF TEST DATA

Table B-1. Unknown sample test matrix of Log (τ_d/τ_0) of 6 CPE sensor array (P1 – P6) against various proteins (1 = avidin, 2 = LYZ, 3 = HRP, 4 = PLD2, 5 = HK3, 6 = BSA, 7 = GOx) with [CPE] = 500 nM and [protein] = 2 μ g/mL in 5 mM HEPEs buffer, pH 7.2, room temperature. (failure tests are denoted with star, I = Identification, V = Verification).

Sample #	P1	P2	P3	P4	P5	P6	I	V
1	-0.035	-0.223	-0.019	1.341	2.198	0.718	4	4
2	1.727	1.032	0.853	0.139	0.013	0.155	1	1
3	1.763	3.791	0.835	0.039	0.017	0.141	2	2
4	0.009	-0.247	-0.248	0.774	0.962	1.185	5	5
5	1.280	2.300	1.193	0.016	0.015	0.069	2	2
6	0.001	-0.443	-0.237	-0.088	0.755	0.807	3	3
7	-0.100	-0.243	-0.188	1.023	1.214	1.297	5	5
8	1.354	1.021	0.677	0.004	-0.007	0.043	1	1
9	0.044	-0.026	0.020	2.507	0.890	0.630	7	7
10	-0.029	-0.234	-0.012	2.002	1.712	0.688	4	4
11	0.024	0.001	0.011	2.642	0.966	0.184	7	7
12	-0.046	-0.123	-0.263	0.916	2.191	0.730	6	6
13	-0.020	-0.270	-0.205	1.254	1.256	0.965	5	5
14	2.635	2.235	1.480	0.235	-0.165	-0.029	2	2
15	-0.047	-0.411	-0.025	1.675	2.751	0.724	4	4
16	-0.003	-0.398	-0.279	1.031	1.211	0.415	3	3
17	1.052	1.332	0.724	-0.020	0.024	0.490	1	1
18*	-0.023*	-1.157*	-0.163*	1.255*	1.156*	0.772*	3*	6*
19	0.000	-0.263	-0.171	1.597	1.164	1.167	5	5
20	-0.020	-0.026	-0.014	3.219	0.835	0.056	7	7
21	1.850	3.330	1.218	0.032	-0.078	0.340	2	2
22	1.260	1.041	0.775	-0.018	-0.090	0.386	1	1
23	-0.020	-0.400	-0.039	1.444	2.493	0.617	4	4
24	-0.023	-0.455	-0.235	1.380	-0.050	0.673	3	3
25	-0.014	-0.142	-0.115	0.916	1.332	0.668	6	6
26	0.034	0.002	0.020	2.612	0.926	0.531	7	7
27*	0.002*	-0.413*	-0.206*	-0.150*	1.104*	0.918*	5*	3*
28	-0.038	-0.113	-0.259	1.126	1.270	0.576	6	6
29	0.003	-0.147	-0.228	1.169	1.448	1.566	5	5
30	0.033	-0.021	0.012	2.881	0.914	0.902	7	7
31	-0.038	-0.218	-0.039	1.756	1.428	0.939	4	4
32*	-0.086*	-0.150*	-0.244*	1.021*	1.181*	0.816*	5*	6*
33	-0.082	-0.068	-0.224	0.971	1.493	0.808	6	6
34	-0.021	-0.150	-0.261	1.309	0.884	1.173	5	5
35	-0.030	-0.304	-0.012	1.643	1.330	0.948	4	4
36	0.888	1.107	0.704	-0.158	-0.157	0.135	1	1

Table B-1. Continued.

Sample #	P1	P2	P3	P4	P5	P6	I	V
37	1.266	3.183	0.867	0.009	-0.087	0.202	2	2
38	-0.064	-0.455	-0.261	-0.091	-0.032	0.945	3	3
39	-0.029	-0.016	-0.011	1.497	0.873	0.091	7	7
40	0.993	2.728	1.149	0.080	0.011	0.178	2	2
41	-0.010	-0.409	-0.261	0.202	0.103	0.796	3	3
42	0.530	0.872	0.747	-0.085	-0.018	0.126	1	1

*Note: failure test

LIST OF REFERENCES

1. J. Mann, *Nature*, 1986, **319**, 818-818.
2. A. D. McNaught and A. Wilkinson, *IUPAC. Compendium of Chemical Terminology. (the "Gold Book")*, Blackwell Scientific Publications, Oxford, 1997.
3. N. Hall, *Chem. Commun.*, 2003, 1-4.
4. A. C. Grimsdale and K. Mullen, *Emissive Materials: Nanomaterials*, 2006, **199**, 1-82.
5. A. Kraft, A. C. Grimsdale and A. B. Holmes, *Angew. Chem. Int. Ed.*, 1998, **37**, 402-428.
6. U. H. F. Bunz, *Chem. Rev.*, 2000, **100**, 1605-1644.
7. I. F. Perepichka, D. F. Perepichka, H. Meng and F. Wudl, *Adv. Mater.*, 2005, **17**, 2281-2305.
8. A. O. Patil, A. J. Heeger and F. Wudl, *Chem. Rev.*, 1988, **88**, 183-200.
9. A. G. MacDiarmid, *Angew. Chem. Int. Ed.*, 2001, **40**, 2581-2590.
10. U. Scherf and E. J. W. List, *Adv. Mater.*, 2002, **14**, 477-487.
11. H. Shirakawa, *Angew. Chem. Int. Ed.*, 2001, **40**, 2575-2580.
12. A. Montali, P. Smith and C. Weder, *Synth. Met.*, 1998, **97**, 123-126.
13. L. Torsi, A. Dodabalapur, L. J. Rothberg, A. W. P. Fung and H. E. Katz, *Science*, 1996, **272**, 1462-1464.
14. H. Sirringhaus, *Adv. Mater.*, 2005, **17**, 2411-2425.
15. S. Gunes, H. Neugebauer and N. S. Sariciftci, *Chem. Rev.*, 2007, **107**, 1324-1338.
16. S. W. Thomas, G. D. Joly and T. M. Swager, *Chem. Rev.*, 2007, **107**, 1339-1386.
17. B. H. Wang and E. V. Anslyn, *Chemosensors: Principles, Strategies, and Applications*, John Wiley & Sons, Inc., Hoboken, New Jersey, 2011.
18. Y. L. Tang, F. Teng, M. H. Yu, L. L. An, F. He, S. Wang, Y. L. Li, D. B. Zhu and G. C. Bazan, *Adv. Mater.*, 2008, **20**, 703-705.
19. E. W. Paul, A. J. Ricco and M. S. Wrighton, *J. Phys. Chem.*, 1985, **89**, 1441-1447.
20. J. Janata and M. Josowicz, *Acc. Chem. Res.*, 1998, **31**, 241-248.

21. J. Gierschner, J. Cornil and H. J. Egelhaaf, *Adv. Mater.*, 2007, **19**, 173-191.
22. T. Q. Nguyen, J. J. Wu, V. Doan, B. J. Schwartz and S. H. Tolbert, *Science*, 2000, **288**, 652-656.
23. C. Y. Tan, M. R. Pinto, M. E. Kose, I. Ghiviriga and K. S. Schanze, *Adv. Mater.*, 2004, **16**, 1208-1212.
24. C. Y. Tan, M. R. Pinto and K. S. Schanze, *Chem. Commun.*, 2002, 446-447.
25. S. H. Lee, S. Komurlu, X. Y. Zhao, H. Jiang, G. Moriena, V. D. Kleiman and K. S. Schanze, *Macromolecules*, 2011, **44**, 4742-4751.
26. M. R. Pinto, B. M. Kristal and K. S. Schanze, *Langmuir*, 2003, **19**, 6523-6533.
27. S. Chemburu, E. Ji, Y. Casana, Y. Wu, T. Buranda, K. S. Schanze, G. P. Lopez and D. G. Whitten, *J. Phys. Chem. B*, 2008, **112**, 14492-14499.
28. X. Y. Zhao and K. S. Schanze, *Chemical Communications*, 2010, **46**, 6075-6077.
29. X. Y. Zhao, M. R. Pinto, L. M. Hardison, J. Mwaura, J. Muller, H. Jiang, D. Witker, V. D. Kleiman, J. R. Reynolds and K. S. Schanze, *Macromolecules*, 2006, **39**, 6355-6366.
30. E. K. Ji, D. L. Wu and K. S. Schanze, *Langmuir*, 2010, **26**, 14427-14429.
31. X. Y. Zhao, H. Jiang and K. S. Schanze, *Macromolecules*, 2008, **41**, 3422-3428.
32. L. H. Chen, S. Xu, D. McBranch and D. Whitten, *J. Am. Chem. Soc.*, 2000, **122**, 9302-9303.
33. S. J. Dwight, B. S. Gaylord, J. W. Hong and G. C. Bazan, *J. Am. Chem. Soc.*, 2004, **126**, 16850-16859.
34. M. R. Eftink and C. A. Ghiron, *Anal. Biochem.*, 1981, **114**, 199-227.
35. J. R. Lakowicz, *Principles of fluorescence spectroscopy*, Springer, New York, 2006.
36. Fluorescein, Oregon Green and Rhodamine Green Dyes—Section 1.5, <http://www.invitrogen.com/site/us/en/home/References/Molecular-Probes-The-Handbook/Fluorophores-and-Their-Amine-Reactive-Derivatives/Fluorescein-Oregon-Green-and-Rhodamine-Green-Dyes.html>, Accessed August, 6th, 2012.
37. J. Wang, D. L. Wang, E. K. Miller, D. Moses, G. C. Bazan and A. J. Heeger, *Macromolecules*, 2000, **33**, 5153-5158.
38. D. L. Wang, J. Wang, D. Moses, G. C. Bazan and A. J. Heeger, *Langmuir*, 2001, **17**, 1262-1266.

39. T. Forster, *J. Biomed. Opt.*, 2012, **17**, 011002-011002-011011
40. R. Y. Tsien, *Annu. Rev. Biochem.*, 1998, **67**, 509-544.
41. W. H. Tan, K. M. Wang and T. J. Drake, *Curr. Opin. Chem. Biol.*, 2004, **8**, 547-553.
42. Q. Zhou and T. M. Swager, *J. Am. Chem. Soc.*, 1995, **117**, 12593-12602.
43. L. H. Chen, D. W. McBranch, H. L. Wang, R. Helgeson, F. Wudl and D. G. Whitten, *P Natl Acad Sci USA*, 1999, **96**, 12287-12292.
44. B. S. Harrison, M. B. Ramey, J. R. Reynolds and K. S. Schanze, *J. Am. Chem. Soc.*, 2000, **122**, 8561-8562.
45. C. Y. Tan, E. Alas, J. G. Muller, M. R. Pinto, V. D. Kleiman and K. S. Schanze, *J. Am. Chem. Soc.*, 2004, **126**, 13685-13694.
46. J. M. Frank and S. J. Wawilow, *Zeitschrift Fur Physik*, 1931, **69**, 100-110.
47. H. Jiang, X. Y. Zhao and K. S. Schanze, *Langmuir*, 2006, **22**, 5541-5543.
48. M. Levitus, K. Schmieder, H. Ricks, K. D. Shimizu, U. H. F. Bunz and M. A. Garcia-Garibay, *J. Am. Chem. Soc.*, 2001, **123**, 4259-4265.
49. K. A. Walters, K. D. Ley and K. S. Schanze, *Langmuir*, 1999, **15**, 5676-5680.
50. J. Kim and T. M. Swager, *Nature*, 2001, **411**, 1030-1034.
51. R. B. Prince, J. G. Saven, P. G. Wolynes and J. S. Moore, *J. Am. Chem. Soc.*, 1999, **121**, 3114-3121.
52. J. C. Nelson, J. G. Saven, J. S. Moore and P. G. Wolynes, *Science*, 1997, **277**, 1793-1796.
53. S. Lahiri, J. L. Thompson and J. S. Moore, *J. Am. Chem. Soc.*, 2000, **122**, 11315-11319.
54. Y. Liu, K. Ogawa and K. S. Schanze, *J. Photochem. Photobiol., C*, 2009, **10**, 173-190.
55. D. L. Zeng, J. G. Cheng, S. J. Ren, J. Sun, H. L. Zhong, E. J. Xu, J. P. Du and Q. A. Fang, *React. Funct. Polym.*, 2008, **68**, 1715-1721.
56. C. F. Xing, Z. Q. Shi, M. H. Yu and S. Wang, *Polymer*, 2008, **49**, 2698-2703.
57. R. Zeineldin, M. E. Piyasena, T. S. Bergstedt, L. A. Sklar, D. Whitten and G. P. Lopez, *Cytom. Part A*, 2006, **69A**, 335-341.

58. C. H. Fan, K. W. Plaxco and A. J. Heeger, *J. Am. Chem. Soc.*, 2002, **124**, 5642-5643.
59. K. E. Achyuthan, T. S. Bergstedt, L. Chen, R. M. Jones, S. Kumaraswamy, S. A. Kushon, K. D. Ley, L. Lu, D. McBranch, H. Mukundan, F. Rininsland, X. Shi, W. Xia and D. G. Whitten, *J. Mater. Chem.*, 2005, **15**, 2648-2656.
60. S. Kumaraswamy, T. Bergstedt, X. B. Shi, F. Rininsland, S. Kushon, W. S. Xia, K. Ley, K. Achyuthan, D. McBranch and D. Whitten, *Proc. Natl. Acad. Sci. U. S. A.*, 2004, **101**, 7511-7515.
61. M. R. Pinto and K. S. Schanze, *Proc. Natl. Acad. Sci. U. S. A.*, 2004, **101**, 7505-7510.
62. F. Rininsland, W. S. Xia, S. Wittenburg, X. B. Shi, C. Stankewicz, K. Achyuthan, D. McBranch and D. Whitten, *Proc. Natl. Acad. Sci. U. S. A.*, 2004, **101**, 15295-15300.
63. B. S. Gaylord, A. J. Heeger and G. C. Bazan, *Proc. Natl. Acad. Sci. U. S. A.*, 2002, **99**, 10954-10957.
64. S. A. Kushon, K. D. Ley, K. Bradford, R. M. Jones, D. McBranch and D. Whitten, *Langmuir*, 2002, **18**, 7245-7249.
65. S. A. Kushon, K. Bradford, V. Marin, C. Suhrada, B. A. Armitage, D. McBranch and D. Whitten, *Langmuir*, 2003, **19**, 6456-6464.
66. B. S. Gaylord, A. J. Heeger and G. C. Bazan, *J. Am. Chem. Soc.*, 2003, **125**, 896-900.
67. I. B. Kim and U. H. F. Bunz, *J. Am. Chem. Soc.*, 2006, **128**, 2818-2819.
68. H. A. Ho and M. Leclerc, *J. Am. Chem. Soc.*, 2004, **126**, 1384-1387.
69. F. He, Y. L. Tang, S. Wang, Y. L. Li and D. B. Zhu, *J. Am. Chem. Soc.*, 2005, **127**, 12343-12346.
70. N. DiCesare, M. R. Pinto, K. S. Schanze and J. R. Lakowicz, *Langmuir*, 2002, **18**, 7785-7787.
71. Y. Liu and K. S. Schanze, *Anal. Chem.*, 2008, **80**, 8605-8612.
72. C. Li, M. Numata, M. Takeuchi and S. Shinkai, *Angew. Chem. Int. Ed.*, 2005, **44**, 6371-6374.
73. F. He, Y. L. Tang, M. H. Yu, S. Wang, Y. L. Li and D. B. Zhu, *Adv. Funct. Mater.*, 2006, **16**, 91-94.

74. Y. L. Tang, F. He, M. H. Yu, S. Wang, Y. L. Li and D. B. Zhu, *Chem. Mater.*, 2006, **18**, 3605-3610.
75. H. A. Ho, A. Najari and M. Leclerc, *Acc. Chem. Res.*, 2008, **41**, 168-178.
76. X. R. Duan, L. B. Liu, F. D. Feng and S. Wang, *Acc. Chem. Res.*, 2010, **43**, 260-270.
77. G. C. Bazan and S. Wang, in *Organic Semiconductors in Sensor Applications*, eds. D. A. Bernards, G. G. Malliaras and R. M. Owens, Springer Berlin Heidelberg, Berlin Heidelberg, 2008, pp. 1-37.
78. Q. H. Xu, S. Wang, D. Korystov, A. Mikhailovsky, G. C. Bazan, D. Moses and A. J. Heeger, *Proc. Natl. Acad. Sci. U. S. A.*, 2005, **102**, 530-535.
79. C. Y. J. Yang, M. Pinto, K. Schanze and W. H. Tan, *Angew. Chem. Int. Ed.*, 2005, **44**, 2572-2576.
80. K. Lee, L. K. Povlich and J. Kim, *Adv. Funct. Mater.*, 2007, **17**, 2580-2587.
81. A. Kessel and N. Ben-Tal, in *Chapman & Hall/CRC mathematical and computational biology series*, CRC Press, Boca Raton, FL.
82. D. J. Selkoe, *Nature*, 2003, **426**, 900-904.
83. R. Aebersold and M. Mann, *Nature*, 2003, **422**, 198-207.
84. C. J. Johnson, N. Zhukovsky, A. E. G. Cass and J. M. Nagy, *Proteomics*, 2008, **8**, 715-730.
85. S. Fields, *Science*, 2001, **291**, 1221-1224.
86. J. Wang, G. D. Liu, M. H. Engelhard and Y. H. Lin, *Anal. Chem.*, 2006, **78**, 6974-6979.
87. T. Li, L. P. Guo and Z. X. Wang, *Biosens. Bioelectron.*, 2008, **23**, 1125-1130.
88. C. P. Soman and T. D. Giorgio, *Langmuir*, 2008, **24**, 4399-4404.
89. C. D. Chin, V. Linder and S. K. Sia, *Lab on a Chip*, 2007, **7**, 41-57.
90. G. B. Hurst, M. V. Buchanan, L. J. Foote and S. J. Kennel, *Anal. Chem.*, 1999, **71**, 4727-4733.
91. H. Jiang, P. Taranekekar, J. R. Reynolds and K. S. Schanze, *Angew. Chem. Int. Ed.*, 2009, **48**, 4300-4316.
92. F. D. Feng, L. B. Liu, Q. O. Yang and S. Wang, *Macromol. Rapid Commun.*, 2010, **31**, 1405-1421.

93. K. Li and B. Liu, *Polymer Chemistry*, 2010, **1**, 252-259.
94. D. T. McQuade, A. E. Pullen and T. M. Swager, *Chem. Rev.*, 2000, **100**, 2537-2574.
95. R. J. Delange, *J. Biol. Chem.*, 1970, **245**, 907-916.
96. F. Cheng, G. W. Zhang, X. M. Lu, Y. Q. Huang, Y. Chen, Y. Zhou, Q. L. Fan and W. Huang, *Macromol. Rapid Commun.*, 2006, **27**, 799-803.
97. O. R. Miranda, C. C. You, R. Phillips, I. B. Kim, P. S. Ghosh, U. H. F. Bunz and V. M. Rotello, *J. Am. Chem. Soc.*, 2007, **129**, 9856-9857.
98. K. P. R. Nilsson and O. Inganäs, *Macromolecules*, 2004, **37**, 9109-9113.
99. L. L. An, Y. L. Tang, F. D. Feng, F. He and S. Wang, *J. Mater. Chem.*, 2007, **17**, 4147-4152.
100. F. D. Feng, Y. L. Tang, F. He, M. H. Yu, X. R. Duan, S. Wang, Y. L. Li and D. B. Zhu, *Adv. Mater.*, 2007, **19**, 3490-3495.
101. F. Pu, D. Hu, J. S. Ren, S. Wang and X. G. Qu, *Langmuir*, 2010, **26**, 4540-4545.
102. Y. Y. Wang, Y. Zhang and B. Liu, *Anal. Chem.*, 2010, **82**, 8604-8610.
103. Y. Liu, K. Ogawa and K. S. Schanze, *Anal. Chem.*, 2008, **80**, 150-158.
104. H. L. Fan, T. Zhang, S. W. Lv and Q. H. Jin, *J. Mater. Chem.*, 2010, **20**, 10901-10907.
105. L. L. An, L. B. Liu and S. Wang, *Biomacromolecules*, 2009, **10**, 454-457.
106. J. M. Busnel, S. Descroix, T. Le Saux, S. Terabe, M. C. Hennion and G. Peltre, *Electrophoresis*, 2006, **27**, 1481-1488.
107. Peptide Property Calculator, <http://www.innovagen.se/custom-peptide-synthesis/peptide-property-calculator/peptide-property-calculator.asp>, Accessed Sep. 16th, 2012.
108. Y. Liu and K. S. Schanze, *Anal. Chem.*, 2009, **81**, 231-239.
109. D. L. Wang, X. Gong, P. S. Heeger, F. Rininsland, G. C. Bazan and A. J. Heeger, *Proc. Natl. Acad. Sci. U. S. A.*, 2002, **99**, 49-53.
110. I. B. Kim, A. Dunkhorst and U. H. F. Bunz, *Langmuir*, 2005, **21**, 7985-7989.
111. F. Huang, X. H. Wang, D. L. Wang, W. Yang and Y. Cao, *Polymer*, 2005, **46**, 12010-12015.

112. K. Ogawa, S. Chemburu, G. P. Lopez, D. G. Whitten and K. S. Schanze, *Langmuir*, 2007, **23**, 4541-4548.
113. I. B. Kim, M. H. Han, R. L. Phillips, B. Samanta, V. M. Rotello, Z. J. Zhang and U. H. F. Bunz, *Chem. Eur. J.*, 2009, **15**, 449-456.
114. J. Wang and B. Liu, *Chem. Commun.*, 2009, 2284-2286.
115. H. P. Li and G. C. Bazan, *Adv. Mater.*, 2009, **21**, 964-967.
116. A. T. Wright and E. V. Anslyn, *Chem. Soc. Rev.*, 2006, **35**, 14-28.
117. J. W. Lee, J. S. Lee and Y. T. Chang, *Angew. Chem. Int. Ed.*, 2006, **45**, 6485-6487.
118. N. A. Rakow and K. S. Suslick, *Nature*, 2000, **406**, 710-713.
119. N. T. Greene and K. D. Shimizu, *J. Am. Chem. Soc.*, 2005, **127**, 5695-5700.
120. J. F. Folmer-Andersen, M. Kitamura and E. V. Anslyn, *J. Am. Chem. Soc.*, 2006, **128**, 5652-5653.
121. A. Buryak and K. Severin, *J. Am. Chem. Soc.*, 2005, **127**, 3700-3701.
122. C. C. You, O. R. Miranda, B. Gider, P. S. Ghosh, I. B. Kim, B. Erdogan, S. A. Krovi, U. H. F. Bunz and V. M. Rotello, *Nature Nanotech.*, 2007, **2**, 318-323.
123. L. L. An, S. Wang and D. B. Zhu, *Chem-Asian J*, 2008, **3**, 1601-1606.
124. A. Bajaj, O. R. Miranda, R. Phillips, I. B. Kim, D. J. Jerry, U. H. F. Bunz and V. M. Rotello, *J. Am. Chem. Soc.*, 2010, **132**, 1018-1022.
125. P. C. Jurs, G. A. Bakken and H. E. McClelland, *Chem. Rev.*, 2000, **100**, 2649-2678.
126. R. A. Johnson and D. W. Wichern, *Applied multivariate statistical analysis*, Prentice-Hall, Englewood Cliffs, N.J., 1988.
127. A. F. Thunemann and D. Ruppelt, *Langmuir*, 2001, **17**, 5098-5102.
128. A. F. Thunemann, *Adv. Mater.*, 1999, **11**, 127-130.
129. L. A. Bastardo, V. M. Garamus, M. Bergstrom and P. M. Claesson, *J. Phys. Chem. B*, 2005, **109**, 167-174.
130. F. Stabo-Eeg, M. Lindgren, K. P. R. Nilsson, O. Inganas and P. Hammarstrom, *Chemical Physics*, 2007, **336**, 121-126.

131. H. J. Yue, M. Y. Wu, C. H. Xue, S. Velayudham, H. Y. Liu and D. H. Waldeck, *J. Phys. Chem. B*, 2008, **112**, 8218-8226.
132. M. Y. Wu, P. Kaur, H. J. Yue, A. M. Clemmens, D. H. Waldeck, C. H. Xue and H. Y. Liu, *J. Phys. Chem. B*, 2008, **112**, 3300-3310.
133. D. Magde, W. W. Webb and E. Elson, *Physical Review Letters*, 1972, **29**, 705-708.
134. O. Krichевsky and G. Bonnet, *Rep. Prog. Phys.*, 2002, **65**, 251-297.
135. J. R. Lakowicz, *Topics in fluorescence spectroscopy*, Plenum Press, New York, 1991.
136. P. Schwille and E. Haustein, Fluorescence correlation spectroscopy. An introduction to its concepts and applications, www.biophysics.org/education/schwille.pdf
137. P. Kask, P. Piksarv, M. Pooga, U. Mets and E. Lippmaa, *Biophys. J.*, 1989, **55**, 213-220.
138. P. F. Fahey, D. E. Koppel, L. S. Barak, D. E. Wolf, E. L. Elson and W. W. Webb, *Science*, 1977, **195**, 305-306.
139. P. F. Fahey and W. W. Webb, *Biochemistry*, 1978, **17**, 3046-3053.
140. D. E. Koppel, D. Axelrod, J. Schlessinger, E. L. Elson and W. W. Webb, *Biophys. J.*, 1976, **16**, 1315-1329.
141. J. Widengren, U. Mets and R. Rigler, *Chemical Physics*, 1999, **250**, 171-186.
142. M. Borsch, P. Turina, C. Eggeling, J. R. Fries, C. A. M. Seidel, A. Labahn and P. Graber, *Febs Letters*, 1998, **437**, 251-254.
143. J. Schuler, J. Frank, U. Trier, M. Schafer-Korting and W. A. Saenger, *Biochemistry*, 1999, **38**, 8402-8408.
144. E. Van Craenenbroeck and Y. Engelborghs, *Biochemistry*, 1999, **38**, 5082-5088.
145. H. Schurer, A. Buchynskyy, K. Korn, M. Famulok, P. Welzel and U. Hahn, *Biol. Chem.*, 2001, **382**, 479-481.
146. T. Wohland, K. Friedrich, R. Hovius and H. Vogel, *Biochemistry*, 1999, **38**, 8671-8681.
147. M. Kinjo and R. Rigler, *Nucleic Acids Res.*, 1995, **23**, 1795-1799.
148. J. Borejdo, *Biopolymers*, 1979, **18**, 2807-2820.

149. H. Pick, A. K. Preuss, M. Mayer, T. Wohland, R. Hovius and H. Vogel, *Biochemistry*, 2003, **42**, 877-884.
150. R. Rigler, U. Mets, J. Widengren and P. Kask, *Eur. Biophys. J. Biophys.*, 1993, **22**, 169-175.
151. R. M. Rigler, Ulo, *Proc. Soc. Photo. Opt. Instrum. Eng.*, 1993, **1921**, 239-248.
152. M. Eigen and R. Rigler, *Proc. Natl. Acad. Sci. U. S. A.*, 1994, **91**, 5740-5747.
153. E. Van Rompaey, N. Sanders, S. C. De Smedt, J. Demeester, E. Van Craenenbroeck and Y. Engelborghs, *Macromolecules*, 2000, **33**, 8280-8288.
154. T. B. Bonne, C. M. Papadakis, K. Ludtke and R. Jordan, *Colloid. Polym. Sci.*, 2007, **285**, 491-497.
155. A. Laguecir, S. Ulrich, J. Labille, N. Fatin-Rouge, S. Stoll and J. Buffle, *Eur. Polym. J.*, 2006, **42**, 1135-1144.
156. A. V. R. Murthy, M. Goel, S. Patil and M. Jayakannan, *J. Phys. Chem. B*, 2011, **115**, 10779-10788.
157. Z. H. Xu, H. H. Tsai, H. L. Wang and M. Cotlet, *J. Phys. Chem. B*, 2010, **114**, 11746-11752.
158. S. Masuo, N. Nishi, M. Hosugi, S. Machida and A. Itaya, *Chem. Lett.*, 2010, **39**, 780-782.
159. A. B. Andrews, R. E. Guerra, O. C. Mullins and P. N. Sen, *J Phys Chem A*, 2006, **110**, 8093-8097.
160. S. Ghosh, U. Mandal, A. Adhikari and K. Bhattacharyya, *Chem-Asian J*, 2009, **4**, 948-954.
161. E. Haustein and P. Schwille, *Annu Rev Biophys Biomol Struct*, 2007, **36**, 151-169.
162. E. Overbeck, C. Sinn, I. Flammer and J. Ricka, *Rev. Sci. Instrum.*, 1998, **69**, 3515-3523.
163. H. C. Burstyn and J. V. Sengers, *Physical Review A*, 1983, **27**, 1071-1085.
164. J. X. Zhu, D. J. Durian, J. Muller, D. A. Weitz and D. J. Pine, *Physical Review Letters*, 1992, **68**, 2559-2562.
165. M. Zhao, L. Jin, B. Chen, Y. Ding, H. Ma and D. Y. Chen, *Appl. Opt.*, 2003, **42**, 4031-4036.

166. S. Wilhelm, Confocal Laser Scanning Microscopy,
[http://www.zeiss.de/C1256D18002CC306/0/F99A7F3E8944EEE3C1256E5C0045F68B/\\$file/60-1-0030_confocal-principles.pdf](http://www.zeiss.de/C1256D18002CC306/0/F99A7F3E8944EEE3C1256E5C0045F68B/$file/60-1-0030_confocal-principles.pdf).
167. Specific gravity, also called relative density, is the ratio of the substance to the density of water at 4 C
168. Free-Space Fiber Coupler for Single Mode Fiber,
<http://www.thorlabs.com/catalogpages/V21/198.PDF>, Accessed Sep. 29th, 2012.
169. K. R. Spring, T. J. Fellers and M. W. Davidson, Confocal Microscope Objectives,
<http://www.olympusmicro.com/primer/techniques/confocal/confocalobjectives.html>, Accessed Sep. 15th, 2012.
170. S. Wilhelm, Carl Zeiss MicroImaging GmbH, Jena, Germany.
171. P. Sengupta, J. Balaji and S. Maiti, *Methods*, 2002, **27**, 374-387.
172. M. Abramowitz and M. W. Davidson, Immersion Media,
<http://www.olympusmicro.com/primer/anatomy/immersion.html>, Accessed Sep. 15th, 2012.
173. K. R. Spring, H. E. Keller and M. W. Davidson, Microscope Objectives Introduction, <http://www.olympusmicro.com/primer/anatomy/objectives.html>, Accessed Sep. 15th, 2012.
174. D. E. Wolf, What is the Confocal Volume?,
http://www.fcsxpert.com/classroom/theory/pdfs/fcs_confocal.pdf, Accessed Sep. 15th, 2012.
175. J. D. Muller, Y. Chen and E. Gratton, *Biophotonics, Pt B*, 2003, **361**, 69-92.
176. D. L. Wu, F. D. Feng, D. P. Xie, Y. Chen, W. H. Tan and K. S. Schanze, *J. Phys. Chem. Lett.*, 2012, **3**, 1711-1715.
177. Although avidin only has 30% sequence identity to streptavidin, they have almost identical secondary, tertiary and quaternary structure
178. L. Haussling, H. Ringsdorf, F. J. Schmitt and W. Knoll, *Langmuir*, 1991, **7**, 1837-1840.
179. G. Balgi, D. E. Leckband and J. M. Nitsche, *Biophysical Journal*, 1995, **68**, 2251-2260.
180. O. Livnah, E. A. Bayer, M. Wilchek and J. L. Sussman, *P Natl Acad Sci USA*, 1993, **90**, 5076-5080.
181. Fude Feng, Kirk S. Schanze, paper in preparation.

182. K. Lee, J. C. Cho, J. DeHeck and J. Kim, *Chemical Communications*, 2006, 1983-1985.
183. D. P. Xie, in *Department of Chemistry*, University of Florida, Gainesville, FL, 2012, p. 152.
184. S. Taira and K. Yokoyama, *Biotechnol. Bioeng.*, 2004, **88**, 35-41.
185. M. X. You, R. W. Wang, X. B. Zhang, Y. Chen, K. L. Wang, L. Peng and W. H. Tan, *Acs Nano*, 2011, **5**, 10090-10095.
186. Y. Kawabe, L. Wang, S. Horinouchi and N. Ogata, *Adv. Mater.*, 2000, **12**, 1281-1283.
187. A. E. Friedman, J. C. Chambron, J. P. Sauvage, N. J. Turro and J. K. Barton, *J. Am. Chem. Soc.*, 1990, **112**, 4960-4962.
188. R. M. Hartshorn and J. K. Barton, *J. Am. Chem. Soc.*, 1992, **114**, 5919-5925.
189. D. M. Mock, N. I. Mock, C. W. Stewart, J. B. LaBorde and D. K. Hansen, *J. Nutr.*, 2003, **133**, 2519-2525.
190. H. P. Lesch, M. U. Kaikkonen, J. T. Pikkarainen and S. Yla-Herttuala, *Expert Opinion on Drug Delivery*, 2010, **7**, 551-564.
191. M. Wilchek and E. A. Bayer, *Biomol. Eng*, 1999, **16**, 1-4.
192. J. T. He, Z. H. Shi, J. Yan, M. P. Zhao, Z. Q. Guo and W. B. Chang, *Talanta*, 2005, **65**, 621-626.
193. M. Jeon, J. Kim, K. J. Paeng, S. W. Park and I. R. Paeng, *Microchem. J.*, 2008, **88**, 26-31.
194. K. Tanaka, S. Yokoi, K. Morimoto, T. Iwata, Y. Nakamoto, K. Nakayama, K. Koyama, T. Fujiwara and K. Fukase, *Biorg. Med. Chem.*, 2012, **20**, 1865-1868.
195. M. Q. Lu, W. Ngo, Y. Mei, V. Munshi, C. Burlein, M. H. Loughran, P. D. Williams, D. J. Hazuda, M. D. Miller, J. A. Grobler, T. L. Diamond and M. T. Lai, *Protein Expres. Purif.*, 2010, **71**, 231-239.
196. E. Ji, in *Department of Chemistry*, University of Florida, Gainesville, FL, 2009, p. 167.
197. M. Slim, N. Durisic, P. Grutter and H. F. Sleiman, *Chembiochem*, 2007, **8**, 804-812.
198. C. M. Ruan, K. F. Zeng, O. K. Varghese and C. A. Grimes, *Biosens. Bioelectron.*, 2004, **19**, 1695-1701.

199. G. S. Hong, C. Li and L. M. Qi, *Adv. Funct. Mater.*, 2010, **20**, 3774-3783.
200. S. Otsuki and M. Ishikawa, *Biosens. Bioelectron.*, 2010, **26**, 202-206.
201. X. D. Song, H. L. Wang, J. Shi, J. W. Park and B. I. Swanson, *Chem. Mater.*, 2002, **14**, 2342-2347.
202. P. Schwille, S. Kummer, A. A. Heikal, W. E. Moerner and W. W. Webb, *Proc. Natl. Acad. Sci. U. S. A.*, 2000, **97**, 151-156.
203. R. Paolesse, D. Monti, F. Dini and C. Di Natale, in *Luminescence Applied in Sensor Science*, Springer-Verlag Berlin, Berlin, Heidelberg, 2011, pp. 139-174.
204. A. P. Demchenko, *Trends Biotechnol.*, 2005, **23**, 456-460.
205. D. Perahia, R. Traiphol and U. H. F. Bunz, *J. Chem. Phys.*, 2002, **117**, 1827-1832.
206. A. Ajayaghosh and S. J. George, *J. Am. Chem. Soc.*, 2001, **123**, 5148-5149.
207. As shown in the webpage of Sigma company, HK3 has two isoforms, PI and PII (A and B), pI = 5.25 and 4, respectively.
208. HRP has at least seven isozymes with pI values range from 3.0 - 9.0 as described in the webpage of Sigma company
209. M. M. Bradford, *Anal. Biochem.*, 1976, **72**, 248-254.
210. Y. Wang, E. Y. Chi, K. S. Schanze and D. G. Whitten, *Soft Matter*, 2012, **8**, 8547-8558.
211. M. Loog, R. P. W. Duin and R. Haeb-Umbach, *IEEE Transactions on Pattern Analysis and Machine Intelligence*, 2001, **23**, 762-766.
212. M. Uray, P. M. Roth and H. Bischof, in *Proc.Int'l Conf. on Computer Vision Theory and Applications*, 2009.
213. Bradford Protein Assay, http://www.science.smith.edu/departments/Biochem/Biochem_353/Bradford.html, Accessed Mar. 15th, 2012.
214. Extinction Coefficients, <<http://www.piercenet.com/files/TR0006-Extinction-coefficients.pdf>>, Accessed Dec. 22nd, 2012, 2012.
215. Y. Chen, in *Department of Biophysics & Computational Biology*, University of Illinois at Urbana-Champaign, Urbana, Illinois, 1999, p. 140.
216. I. B. Kim, A. Dunkhorst, J. Gilbert and U. H. F. Bunz, *Macromolecules*, 2005, **38**, 4560-4562.

217. B. Liu, H. G. Dai, Y. Y. Bao, F. F. Du, J. Tian and R. K. Bai, *Polymer Chemistry*, 2011, **2**, 1699-1705.
218. B. Liu, Y. Y. Bao, F. F. Du, H. Wang, J. A. Tian and R. K. Bai, *Chem. Commun.*, 2011, **47**, 1731-1733.
219. B. Liu, Y. Y. Bao, H. Wang, F. F. Du, J. Tian, Q. B. Li, T. S. Wang and R. K. Bai, *J. Mater. Chem.*, 2012, **22**, 3555-3561.
220. D. Winter and C. D. Eisenbach, *J. Polym. Sci., Part A: Polym. Chem.*, 2004, **42**, 1919-1933.
221. C. H. Li, Y. B. Guo, J. Lv, J. L. Xu, Y. L. Li, S. Wang, H. B. Liu and D. B. Zhu, *J. Polym. Sci., Part A: Polym. Chem.*, 2007, **45**, 1403-1412.
222. Y. Q. Hu, Y. Xiao, H. M. Huang, D. L. Yin, X. M. Xiao and W. H. Tan, *Chem-Asian J*, 2011, **6**, 1500-1504.
223. J. C. Wataha and C. T. Hanks, *J. Oral. Rehabil.*, 1996, **23**, 309-320.
224. J. Kielhorn, C. Melber, D. Keller and I. Mangelsdorf, *Int. J. Hyg. Envir. Heal.*, 2002, **205**, 417-432.
225. B. Dimitrova, K. Benkhedda, E. Ivanova and F. Adams, *J. Anal. At. Spectrom.*, 2004, **19**, 1394-1396.
226. C. Locatelli, D. Melucci and G. Torsi, *Anal. Bioanal. Chem.*, 2005, **382**, 1567-1573.
227. K. Van Meel, A. Smekens, M. Behets, P. Kazandjian and R. Van Grieken, *Anal. Chem.*, 2007, **79**, 6383-6389.
228. R. N. Rao and M. V. N. K. Talluri, *J. Pharm. Biomed. Anal.*, 2007, **43**, 1-13.
229. E. Unterreitmaier and M. Schuster, *Anal. Chim. Acta*, 1995, **309**, 339-344.
230. H. M. Huang, K. Wang, W. H. Tan, D. An, X. H. Yang, S. S. Huang, Q. Zhai, L. Zhou and Y. Jin, *Angew. Chem. Int. Ed.*, 2004, **43**, 5635-5638.
231. T. Schwarze, H. Muller, C. Dosche, T. Klamroth, W. Mickler, A. Kelling, H. G. Lohmannsroben, P. Saalfrank and H. J. Holdt, *Angew. Chem. Int. Ed.*, 2007, **46**, 1671-1674.
232. F. L. Song, A. L. Garner and K. Koide, *J. Am. Chem. Soc.*, 2007, **129**, 12354-12355.
233. C. Y. Tan, in *Department of Chemistry*, University of Florida, Gainesville, FL, 2004, p. 163.

234. C. H. Chen, W. H. Chen, Y. H. Liu, T. S. Lim and T. Y. Luh, *Chem. Eur. J.*, 2012, **18**, 347-354.
235. B. Wang and M. R. Wasielewski, *J. Am. Chem. Soc.*, 1997, **119**, 12-21.

BIOGRAPHICAL SKETCH

Danlu Wu was born in the city of Longyan, Fujian province, China. In 2003, she graduated from No. 1 Middle School of Longyan and got the admission of University of Science and Technology of China (USTC). She started her college education in September, and obtained her bachelor's degree in polymer chemistry four years later. In August of 2007, she came to United States and enrolled in Department of Materials Science and Engineering, University of Florida for graduate study. One year later, she got the master degree in materials science and then she transferred to Department of Chemistry in the same university. Danlu joined the group of Dr. Kirk S. Schanze to pursue her Ph.D. in analytical chemistry. In the past four and half years, she researched in the amazing area of development of conjugated polyelectrolytes based fluorescent sensing methods. She received her Ph.D. in the fall of 2012.